Precision Measurements in a Rydberg Quantum Optics Experiment

Mikkel Gaard Hansen

Supervised by Prof. Sebastian Hofferberth

A thesis submitted for the degree of
Master of Physics

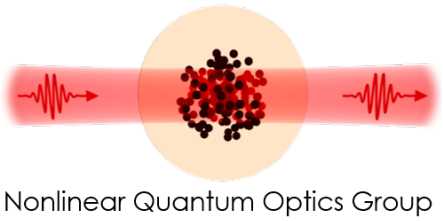

Department of Physics, Chemistry and Pharmacy
University of Southern Denmark
Denmark
2021-June-01

Abstract

The use of ultra low linewidth lasers to excite atoms to specific states is a fundamental concept in modern experimental atomic physics.

In the work of this thesis three lasers with wavelengths of 780 nm, 960 nm and 1012 nm respectively, are locked to an ultra stable, high finesse, cavity. These wavelengths serve as the probe, control, and magic wavelength-trap in the Rydberg quantum optics experiment with rubidium atoms in which they are used. Mode matching into a cavity, characterization of the cavity, generating a Pound-Drever-Hall error signal, and using it to narrow the linewidth of the control laser are described and discussed in this thesis.

Further, A phase interferometer for measuring the phase shift imprinted on a photon when interaction with an atomic ensemble is constructed, tested, and implemented in this work. Phase shifts of $\pm\pi$ are observed for photon rates of 0.09 photons/μs at 20 MHz probe detuning. A relation of lower phase shift with higher detuning from probe resonance is observed with 0.3π phase shifts observed at 100 MHz detuning. The phase shift imprinted by the interaction is measured to reduce in magnitude with increasing light intensities.

Finally, a scheme for realizing an all-optical non-reciprocal effect in a vapor cell is presented. Using the negative Doppler shift of hot atoms in a vapor cell a broadened Electromagnetic Induced Transparency (EIT) window is observed with counter-propagating probe and control laser in a ladder EIT configuration. No EIT is observed in the case of co-propagating probe and control leading to the non-reciprocal effect.

Resumé

Brugen af lasere med en ultra lav linjebredde i bestræbelserne på at adressere specifikke energiniveauer i et atom, er et fundamentalt koncept i moderne eksperimentel atomfysik.

I dette speciale er tre laseren med bølgelængder på henholdsvis 780 nm, 960 nm and 1012 nm låst til et ultrastabilt, høj finesse, kavitet. Disse tre bølgelængder er implementeret i et Rydberg kvante optik eksperiment hvor der arbejdes med rubidium, hvori de bruges som probe, kontrol og magisk bølgelængde fælde. Tilstandstilpasning til kaviteten, generering af the Pound-Drever-Hall error-signal, og hvordan dette bruges til at opnå en lavere linjebredde, er forklaret og diskuteret i detaljer, for kontrol laseren.

Et fase interferometer, til at måle faseskiftet induceret i en foton ved interagering med et atom, er konstrueret, testet og implementeret i dette speciale. Faseskift på $\pm\pi$ er observeret for foton rater på 0.09 photons/μs at 20 MHz probe afvigelse fra resonans. En relation mellem lavere faseskift ved højere afvigelser fra probe resonans er observeret, med 0.3π faseskift observeret ved 100 MHz afvigelse. Faseskiftet der forekommer ved interaktionen er målt til at falde i magnitude ved en forøgelse af lysintensiteten. Til sidst er en ny måde at opnå en ren optisk ikke-reciprok effekt præsenteret. Ved at udnytte det negative Doppler skift i varme atomer i en dampcelle opnås et bredere elektromagnetisk induceret transperans vindue for modsat propagarende probe og kontrol lasere i en stige EIT konfiguration. Intet EIT er observeret i det parallel propagerende tilfælde, hvilket giver den ikke-reciprokke effekt.

Contents

Introduction

With the development of the laser in the 1960s [1], atomic physicists received a new way of manipulating atoms. The lasers' almost monochromatic nature allows for interaction with specific atomic states. Reducing the laser linewidth has been an ongoing challenge for physicists ever since the laser was first developed. A revolutionary technique using the reflected signal from an optical resonator was developed by Pound, Drever, and Hall in 1983 [2] and has led to lasers with linewidths in the mHz range [3, 4]. Ultra narrow linewidth lasers are currently used to break records on optical clock stability [5] and to put constraints on the energy of dark matter in cosmology research [6] as well as many other areas of physics.

The development of ultra narrow linewidth lasers for interacting with a single hyperfine level of an atomic state has opened up various fields of atomic physics, including that of Nonlinear Quantum Optics. Within this field, we are interested in the optical nonlinearities that can be obtained by utilizing Rydberg atoms [7]. Rydberg atoms, atoms where one or more electrons are excited to a high principal quantum number, prove great candidates for studying atom-light interactions. They provide a way of overcoming the intrinsic low atom-photon cross-section and in general weak coupling of light fields to atoms [8, 9]. Rydberg atoms exhibit extreme properties compared to other atoms in terms of size, lifetime, polarizability, and interaction strength with other atoms via van-der-Waals or dipole-dipole interactions [10]. Due to their highly excited electron, the induced dipole moment of a Rydberg atom becomes so strong as to shift the energy levels of other nearby atoms exhibiting a blockade-like behavior preventing other Rydberg excitations within a volume given by the blockade radius [11, 12]. For blockades the size of the ensemble of trapped atoms, the atoms are effectively entangled and the entire ensemble can be coherently manipulated by just a single photon [13, 14]. Due to the long lifetime of Rydberg states, these can also conveniently be used for Electromagnetic Induced Transparency (EIT). In EIT the population is coherently trapped in one atomic state and a strong field coupling two states is used to induce a splitting of the excited state in a dressed state picture. The splitting of the excited state puts an otherwise resonance transition between the excited state and some other state off resonance and thereby induced transparency in an otherwise opaque medium [15]. This effect has many practical applications including laser locks [16] and phase gates [17]. Phase gates can be realized by examining the phase imprinted by the atom-photon interaction and proves a great tool for quantum information [18].

Optical systems are, for the most part, linear and reversible. Even though non-linear behaviors are widely known and used, they prove to be more rare than their linear counterparts. Non-reciprocal optical effects, however, have so far been difficult to realize on the single photon level [19–21]. In solid-state physics, Faraday isolators have been known for many years and while nanofabrication has come a long way using nanofibers for optical non-reciprocal applications [22], an all-optical scheme was only realized very

recently [23]. In this work, we present a novel way of realizing non-reciprocal optics in a vapor cell. Due to the atomic motion in the vapor cell the resulting transmission of the atoms on EIT resonance depend on the relative propagation direction of the EIT beams. The demonstration here is to our knowledge the first ever with Rydberg atoms.

About This Thesis

In the scope of this thesis, three different topics, all closely related to Rydberg physics with rubidium atoms, have been studied.
The first project deals with the locking of lasers to a very narrow linewidth. The project has dealt with implementing laser locks on three lasers of wavelengths 780 nm, 960 nm and 1012 nm, using an ultra stable glass cavity. These lasers have lengths utilized throughout the other experimental work performed in the scope of this project. The 780 nm laser was used to construct and test an interferometer designed to measure the phase change imprinted on a single photon. The interferometer was implemented into the running Rydberg quantum optics experiment in which the 780 nm laser and frequency doubled output of the 960 nm laser was used to make Rydberg atoms and measure the phase imprinted on the single photons from the 780 nm laser.
Finally, the same two lasers was used for implementing an all optical non-reciprocal scheme in a rubidium vapor cell.

This thesis is structured as follows. In chapter 1 theory relevant to all three sub project of this work is presented. This includes four section. The first gives a description of using beat notes to down-convert an optical signal to a frequency suitable for our electronics. In the second section the basic properties of Gaussian optics are treated. Section three introduces the number state of quantized light and the fourth section gives a description of atomic physics related to rubidium as well as a description of Rydberg Physics and Electromagnetic Induced Transparency. In chapter 2, 3, and 4 the experimental work of this thesis is presented. Chapter 2 presents the work done on frequency stabilizing the three lasers to an ultra stable glass cavity. In Chapter 3, the work on a phase interferometer designed to measure the phase of Rydberg atoms in an ultracold cloud of atoms, is presented. The process is described from the design stage and up to and including phase measurements on rudibium Rydberg atoms. In the last chapter on the experimental work, the design and implementation of a setup designed to test a theoretical proposal on an all-optical non-reciprocal light scheme is presented. The 5th chapter of this thesis summarizes on the results and outlooks presented in chapter 2 to 4.

Chapter 1

Common Theory

This thesis covers multiple different topics. However, the individual projects are based on the same theoretical framework and the same techniques are applied for all the projects. This chapter will review the theoretical concepts relevant throughout the following chapters. In the first section, a mathematical formulation of a beat note signal is derived. Beat notes are used extensively throughout this thesis as a way of down-converting the frequency of visible light to a frequency measurable by our electronics. The second section presents key elements of Gaussian optics used to describe the focusing of a laser beam. The third section explains the number state description of quantized light. This regime is important when the intensity of the light is so low the classical wave picture is insufficient. Throughout this thesis, the atomic species of rubidium is used for experiments. Therefore, in the fourth and final section of this chapter, some important atomic properties of rubidium are presented. Furthermore, Rydberg Physics and Electromagnetic Induced Transparency are discussed.

1.1 Measuring with Beat Notes

Electromagnetic radiation in the visible spectrum oscillates at frequencies of hundreds of THz. The frequency of 780 nm light, which is used extensively in the experimental work of this thesis, is $\omega_l = 384\,\mathrm{THz}$ and while fast oscilloscopes exist they remain too slow to capture this frequency. The oscilloscope primarily used in this work can measure a signal of maximum 200 MHz[1], called ω_D which is much smaller than ω_l.
To nonetheless investigate laser frequencies, and in particular changes in frequency, it is possible to down-convert the frequency. This is done by not measuring the light directly, but instead measuring the beat note between two waves with slightly different frequencies. This beat note will have a component oscillating at the difference of the frequencies of the two waves. This beat note oscillation can be measured by the available electronics.
In this thesis, beat notes are used extensively, both to measure changes in laser frequency, but also to determine changes in the relative phase between two laser beams. Such phase changes can be caused for instance by changes in path lengths as we will see in chapter 2 and 3, or by atom-light interactions as we will see in section 3.3.

In this section, a beat note between laser beams of arbitrary phase and frequency is derived mathematically.

[1] Keysight MSOX2024A

Assume that two electromagnetic waves with amplitudes $E_{1,2}$, frequency $\omega_{1,2}$ and phase $\phi_{1,2}$ are superimposed. The resulting electric field becomes

$$E_{tot} = E_1 \cos(\omega_1 t + \phi_1) + E_2 \cos(\omega_2 t + \phi_2). \tag{1.1}$$

The difference in the two frequencies is called the beat note frequency and is given as $\omega_b = \omega_2 - \omega_1$. Measurements are done using electric detectors. Such detectors register the intensity of the light which is given as the norm-square of the electric field.

$$I_{tot}(t) = |E_1 \cos(\omega_1 t + \phi_1) + E_2 \cos(\omega_2 t + \phi_2)|^2 \tag{1.2}$$

$$= E_1^2 \cos^2(\omega_1 t + \phi_1) + E_2^2 \cos^2(\omega_2 t + \phi_2) + 2E_1 E_2 \cos(\omega_1 t + \phi_1)\cos(\omega_2 t + \phi_2).$$

The first two terms in this equation oscillates at the optical frequencies of the two waves. As we are interested in the time dependent signal on an electric a detector, these two terms simplify to $E_{1,2}/2$ as the average of a $\cos^2(x)$ is $1/2$. The remaining expression contains the interference between the two beams.

$$I_{tot}(t) \propto 2E_1 E_2 \cos(\omega_1 t + \phi_1)\cos(\omega_2 t + \phi_2). \tag{1.3}$$

The trigonometric identity for the product of two cosine waves can be applied to this expression

$$\cos(x)\cos(y) = \frac{1}{2}\cos(x+y) + \frac{1}{2}\cos(x-y). \tag{1.4}$$

Resulting in

$$I_{tot}(t) \propto E_1 E_2 \left(\cos\left((\omega_2 - \omega_1)\, t - \Delta\phi\right) + \cos\left((\omega_2 + \omega_1)\, t + \Delta\phi\right)\right), \tag{1.5}$$

with $\Delta\phi = \phi_2 - \phi_1$. The first term can be recognized as oscillating with the beat note frequency $\omega_b = \omega_2 - \omega_1$. The second term is also a beat note of this signal but of frequency equal to the sum of the two optical frequencies putting it even further out of reach of detectors, hence this term can be dropped as it averages out. This yields the signal which will be visible using a photodiode

$$I_{tot} \propto \cos(\omega_b t + \Delta\phi). \tag{1.6}$$

The above calculation holds for any optical frequency due to the approximations and assumptions made. The final expression in equation (1.6) contains the difference in phase of the two superimposed waves. By using one of these waves as a trigger for the measurement it is possible to define a "zero-point" allowing for the determination of this relative phase of the two waves.

1.2 Gaussian Optics

The different topics in this thesis are all centered around the manipulation of light. Light is described by the Maxwell equations. In the case of a collimated laser beam, the paraxial approximation to the Helmholtz equation is applicable and light can be treated as rays propagating as straight lines. This description is sufficient for many everyday phenomena but does not describe the full behavior of light in the classical limit. At this point, one turns to Gaussian Optics. Gaussian optics refer to the simplest solution to the Helmholtz equation. In this description, light is not regarded as a ray, but rather as a wavefront with

a Gaussian intensity profile. This section contains some important aspects of Gaussian optics that are essential for mode matching into an optical cavity, section 2.3, and in general useful optics knowledge for any optics experiment.

Gaussian beams are characterized by a single parameter. This is the beam waist ω_0, which is the radius of the beam at the focus. If this quantity is known, the behavior of the beam size and divergence can be determined at any point z along the optical axis. This is illustrated in figure 1.1.

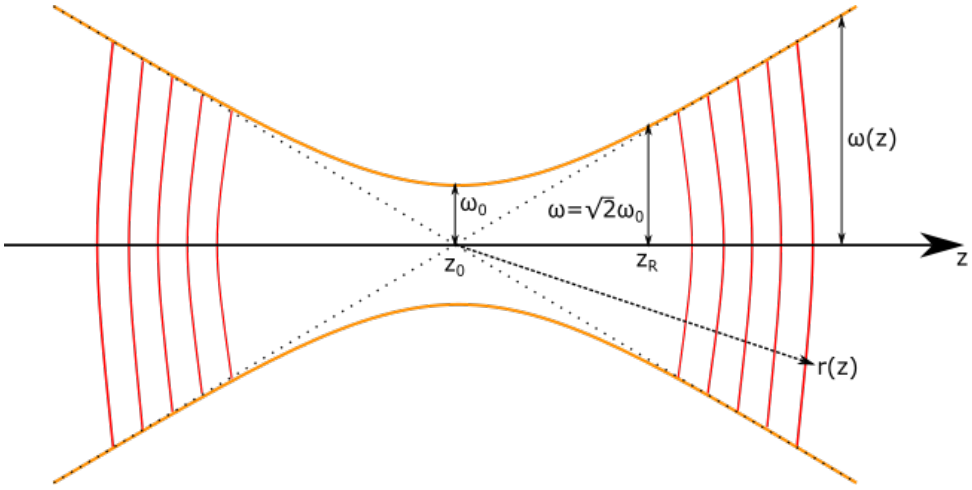

Figure 1.1: *Illustration of a focused Gaussian beam. The orange lines is the beam diameter at any point z. The black dotted lines is the ray-optics approximation. ω_0 is the beam waist at z_0, z_R is the Rayleigh range and $r(z)$ is the distance to the wavefront from the center point z_0.*

In this figure the waist, $\omega(z)$, is shown with orange lines and the paraxial ray-approximation is shown as black dotted lines.
The waist, $\omega(z)$ is mathematically given as [24]

$$\omega(z) = \omega_0 \sqrt{1 + \left(\frac{z}{z_R}\right)^2}. \tag{1.7}$$

$$z_R = \frac{\pi \omega_0^2 n}{\lambda}. \tag{1.8}$$

Here z_R is the Rayleigh range which is the distance from focus to the point where the waist is $\omega_{z_r} = \sqrt{2}\omega_0$. In the definition of the Rayleigh range the refractive index n and wavelength λ also enters.
The radius of curvature at any point z can be determined as

$$R(z) = z\left[1 + \left(\frac{z_R}{z}\right)^2\right]. \tag{1.9}$$

This equation shows, that when approaching focus, z_0, the radius of curvature approaches infinity with a flat wavefront at the focus. For large distances z the radius of curvature of the wavefront increases linearly with distance as shown in figure 1.1.

Determining the radius of curvature from the beam waist will prove essential for designing the optical setup around the cavity for the laser locks in chapter 2. By combining

the above three equations an expression for the curvature as a function of the waist can be found

$$R(z) = z\left[1 + \frac{\omega^2(z) - \omega_0^2}{\omega_0^2}\right]. \tag{1.10}$$

This equation have been derived by rewriting (1.7) and inserting (1.9).
An important property of Gaussian beam propagation and focusing is the wavelength dependency of the Rayleigh range. When working with two lasers of very different wavelength as done in chapter 4 the $1/\lambda$ in equation (1.8) plays a large role since two beams of different wavelength focused to the same beam waist will not have the same behavior away from the focus. The difficulties of making two same-sized beams over as large a range as possible are further investigated in section 4.2.

1.3 Single Photons

In this section key equations for the quantum description of light are presented. In both the interferometer testing and implementation, as well as the Vapor Cell EIT experiment, the quantum regime of light is encountered. It is important to have an understanding of the photon, the quanta of light, even though the data is not treated on a photon by photon level. The single-photon picture is always used when the intensity of the light is too low for the classical wave-picture of Maxwell to apply.

The photon is a massless spin 1 particle [25]. It is an energy package traveling at the speed of light with a frequency related to the energy via the Planck constant. The photon also carries momenta meaning it can be the mediator of a force which is utilized in a magneto-optical-trap (MOT), a common way of trapping atoms [26], and in the field of cavity optomechanics as the mediator between optical and mechanical systems [27].

In a single photon picture, we assume that the photons are so few that they are countable. The total number n is can be written as $|n_{k,\lambda}\rangle$ using the bra-ket-notation. This is called a number state or Fock state. Such a state should be read as the number of photons n with momentum k and polarization λ. Light in the quantum picture is described as a harmonic oscillator with the number states as eigenstates. The quantum harmonic oscillator Hamiltonian takes the form

$$\hat{H} = \frac{\hat{p}^2}{2m} + \frac{1}{2}m\omega^2\hat{q}^2, \tag{1.11}$$

with hats indicating operators and p,q being the momentum and position respectively.
It is convenient to write this equation in terms of two dimensionless operators called the *creation* and *annihilation* operators. These take the form of equation (1.13) and have the properties of ladder operators that either go "up" one energy level or "down", i.e. they describe the process of creating or annihilating a photon. Such a creating or annihilation process can happen via the two fundamental processes absorption and emission.

$$\hat{a}^\dagger = \sqrt{\frac{1}{2m\hbar\omega}}\,(m\omega\hat{q} - i\hat{p}) \tag{1.12}$$

$$\hat{a} = \sqrt{\frac{1}{2m\hbar\omega}}\,(m\omega\hat{q} + i\hat{p}) \tag{1.13}$$

These operators has the property of their commutator equaling 1, $\left[\hat{a},\hat{a}^\dagger\right] = 1$.
The Hamiltonian can be rewritten in terms of these operators

$$\hat{H} = \hbar\omega\left(\hat{a}^\dagger\hat{a} + \frac{1}{2}\right). \tag{1.14}$$

Applying an energy number state $|n\rangle$ to this equation yields an expression for the energy

$$\hat{H}\,|n\rangle = \hbar\omega\left(\hat{a}^\dagger\hat{a} + \frac{1}{2}\right)|n\rangle = E_n\,|n\rangle\,. \tag{1.15}$$

From this equation, it is straightforward to show that the ground state energy is given by $E_0 = \frac{1}{2}\hbar\omega$ and that any other energy eigenstate is separated by exactly $\hbar\omega$ resulting in the following equation for the energy corresponding to some number of photons

$$E_n = \hbar\omega\left(n + \frac{1}{2}\right), \qquad n = 0,1,2,\ldots, \tag{1.16}$$

with n being the number of photons and ω the frequency of these.
In this work, we merely consider the single photons picture as when they are countable and show up as single clicks on the electronics of the TimeTagger.

1.4 Rubidium and Rydberg Physics

The topics of this thesis all relates to the use of rubidium atoms for conducting atomic physics experiments. The lasers locked in chapter 2 are chosen specifically for working with rubidium and in chapter 3 and 4 rubidium atoms are used for the experiments presented.

In this section, the important atomic physics related to Rubidium is presented as well as the physics of Rydberg atoms which is of interest for this work. This includes a description of the concept of electromagnetic induced transparency.

1.4.1 Atomic Properties of Rubidium

Rubidium is the 37th atom in the periodic table and is the species used throughout this thesis. Rubidium is an alkali atom, i.e. it is located in the far left column of the periodic table and has a single valence electron. This electron is located in the 5S shell. Rubidium is arguably the most used atomic species for quantum optics due to its energy levels being convenient for the use of diode lasers. The natural abundance of Rubidium is 72.17% ^{85}Rb and 27.83% ^{87}Rb. ^{87}Rb is unstable and decays via β^- decay with a half life time of 4.9×10^{10} years but this decay can be fully neglected. In the phase measurements of the cloud of cold atoms presented in section 3.3, only the 87 isotope is of interest as only this isotope is trapped in the dipole trap. For the Vapor Cell experiment in chapter 4 both of the isotopes are important as the cell contains a natural abundance of Rubidium.

We choose to describe the rubidium level structure in the hyperfine basis with quantum numbers F, to include the hyperfine structure of the energy states. It is important to distinguish between the hyperfine states as they have a measurable frequency difference and will be noticeable when doing Doppler-free spectroscopy, see section 4.3. The hyperfine structure arises from the coupling between the nuclear magnetic moment and the

magnetic moment due to the electron spin. It is defined as the nuclear quantum number I plus the total angular momentum J which is the addition of orbital angular momentum L and the electron spin S.

$$F = I + L + S = I + J \tag{1.17}$$

This total angular momentum of the atom can adopt the values

$$|I - J| \leq F \leq |I + J| \,. \tag{1.18}$$

The quantum numbers are discrete in nature and can take on integer and half integer values. The F levels can be further divided into sub-levels called m_F states. There are $2F + 1$ m_F levels

$$m_F = -F, -F + 1, \cdots, F. \tag{1.19}$$

The F-basis obeys the know eigenvalue equations

$$\vec{F}^2 = F\,(F + 1)\,\hbar^2, \tag{1.20}$$

$$F_z = m_F \hbar. \tag{1.21}$$

The symmetry properties of the electric dipole operator result in non-vanishing dipole-matrix elements only for specific transitions, where the quantum numbers of the initial and final states obey the so-called selection rules. The rules are as follows: The total orbital angular momentum L must change, $\Delta L = \pm 1$, and the spin cannot change, i.e. $\Delta S = 0$. This gives the rules $\Delta J = \pm 1{,}0$ and $\Delta F = \pm 1{,}0$ with the exception that the transition of $F = 0 \rightarrow F' = 0$ and similar for J cannot happen as this would require the rule on L to be broken [28].

In the experiments presented in this thesis, rubidium atoms are usually excited from the ground state $5S_{1/2}$ to the $5P_{3/2}$ state and further to some Rydberg state of interest. In figure 1.2 the energy level structure of the levels of interest for this work is seen. The figure shows the D2-line transition. The D1 line corresponds to the $5P_{1/2}$ state which is the other fine splitting state. It is separated far enough from the $5P_{3/2}$ state that it is of no concern in this context [29, 30]. Depending on the isotope, the ground state energy level is shifted relative to the ionization energy, due to the structure of the atomic core. The levels are shown with their respective hyperfine splitting, i.e. different F quantum numbers. It is important to notice that the isotope shift and hyperfine splittings for the Rydberg states are so small it is generally ignored. The transition to specific sub-levels of Rydberg states will anyway be suppressed by the linewidth of the lasers used for this work.

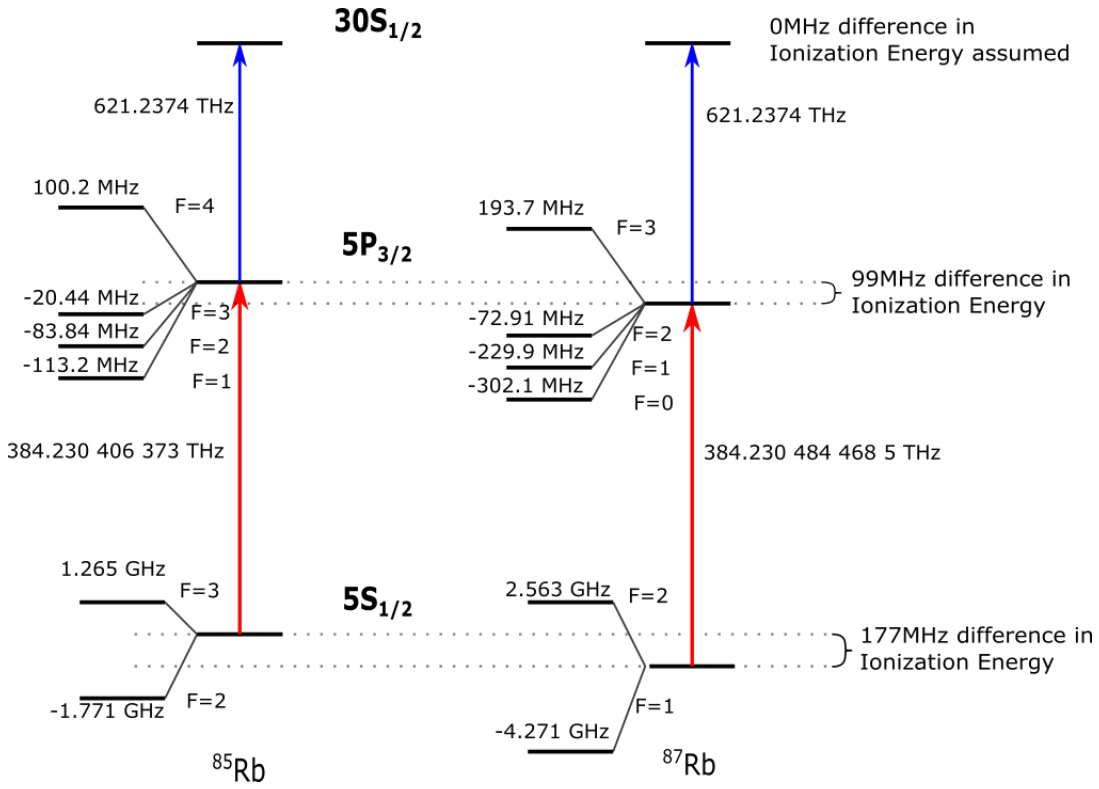

Figure 1.2: *Atomic level structure with the $5S_{1/2}$, the $5P_{3/2}$, and the $30S_{1/2}$ states of ^{85}Rb and ^{87}Rb. The base energy level is shifted by an amount dependent on the isotope called the isotope shift. This equal* 177 MHz *for the ground state,* 99 MHz *for the excited state but is negligible for the Rydberg states.*

1.4.2 Electromagnetic Induced Transparency

Electromagnetic induced transparency (EIT) is the concept of opening up a transmission window in an otherwise fully absorbed transition. In an illustrative picture, this means shining a powerful laser onto an optically thick medium in such a way the medium becomes transparent to another laser. EIT requires a three-level system and two lasers. The three states are named $|1\rangle$, $|2\rangle$ and $|3\rangle$ with the labels always such that transition $|1\rangle \rightarrow |2\rangle$ is dipole forbidden [15]. There are three different level configurations suitable for EIT as shown in figure 1.3.

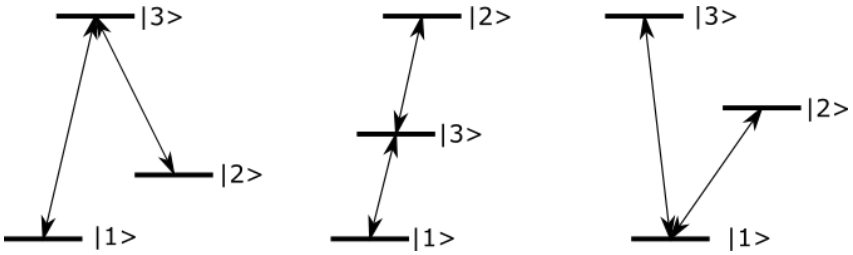

Figure 1.3: *Three possible EIT schemes. On the left is the lambda scheme, the center is the ladder scheme and the rightmost is the vee scheme. The labels are such that the $|1\rangle \rightarrow |2\rangle$ is always the dipole forbidden transition.*

The three include the lambda configuration, ladder configuration, and Vee configuration.

The lambda scheme is presented below to understand the concept of EIT. This is followed by a discussion of the ladder scheme used in several chapters of this work but shows no EIT in the strict sense because of the absence of a metastable dark state [15]. The Vee configuration is not discussed further in this work.

The important quantity for measuring EIT is the imaginary part of the susceptibility. The equation describing this can be derived by considering the master equation with a term taking coherent relaxation processes into account. A total of three levels are needed in a configuration similar to the lambda scheme. Such a derivation can be done using the density matrix formalism. In this formalism, the system is expressed as a matrix with the population of each state on the diagonal and the transition probabilities between the states on the off-diagonal. This derivation can be found in [31]. Here I merely state the final result in its general form with both lasers detuned from resonance.

$$\chi = \frac{-iN\left|\langle 2|\,\hat{\varepsilon}_2 \cdot d\,|3\rangle\right|^2}{\epsilon_0 \hbar} \frac{\left[(\Delta_2 - \Delta_1) + i\gamma_{21}\right]}{(i\Delta_2 - \Gamma_2/2)\left[(\Delta_2 - \Delta_1) + i\gamma_{21}\right] - i\left(\Omega_1/2\right)^2}. \tag{1.22}$$

In this equation N is the atomic density which is given by the temperature, the bra-ket with state 2 and 3 is the dipole moment between these two states, $\Delta_{2,1}$ are the detunings from resonance for each state respectively, Γ_2 is the decay to state two, γ_{21} is the dephasing and Ω_1 is the control laser rabi frequency. By looking at this for on resonance parameters, at a temperature of 40 °C, and a control field of rabi frequency $2\pi \cdot 320\,\mathrm{MHz}$, and for no control field at all, the plot in figure 1.4 is obtained.

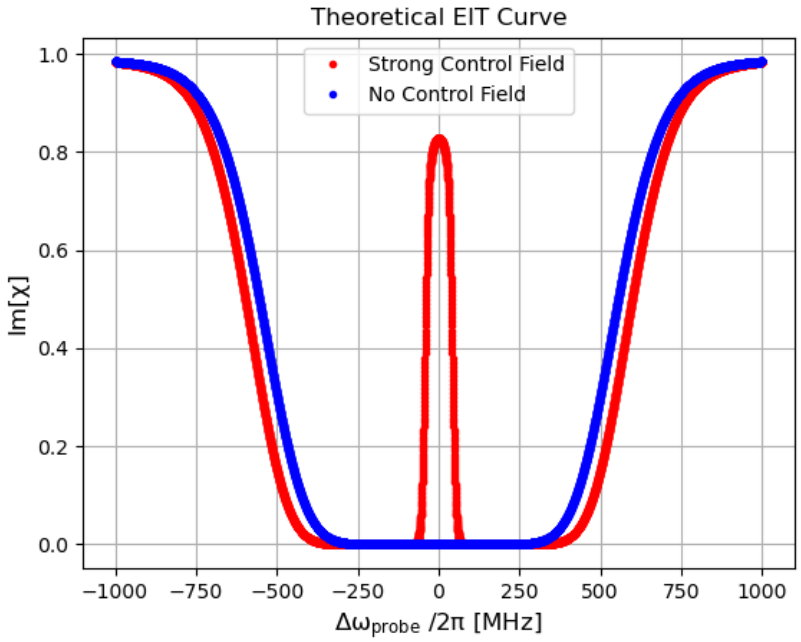

Figure 1.4: *EIT for on resonant light at* $40°C$ *and a control field of either* $2\pi \cdot 320\,\mathrm{MHz}$ *or for no control field at all. The red curve is with EIT and the blue without.*

In this figure, both fields are on single-photon resonance. If two-photon resonance is met but at some detuning from probe resonance the EIT peak will shift to either side depending on the detuning. This effect arises in the implementation of the phase interferometer in section 3.3.

Lambda Scheme

The lambda EIT scheme is widely used when trying to understand the mechanism of EIT [15]. In figure 1.5 a lambda scheme is sketched with the probe and control frequencies $\omega_{p,c}$, their respective detunings $\Delta_{p,c}$ and the decay from state $|3\rangle$ to the other two states, Γ_{31} and Γ_{32}. The effect of EIT can be viewed in the frame of a "Dressed State"-picture. In this picture, the control laser coupling state $|2\rangle \leftrightarrow |3\rangle$ induces a splitting in the energy level of state $|3\rangle$, such that it is a superposition of the two states ($|2\rangle \pm |3\rangle$). This makes it so that for a probe laser on resonance with the initial state $|3\rangle$, thus expecting full absorption, the energy level is now split and the otherwise resonant beam is detuned from both of the dressed states, leading to full transmission.

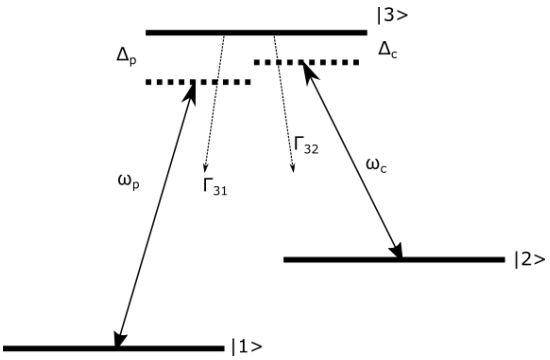

Figure 1.5: *Lambda EIT scheme with three level and the $|1\rangle \rightarrow |2\rangle$ forbidden by selection rules. $\omega_{c,p}$ is the control and probe frequencies, $\Delta_{c,p}$ the respective detunings from resonance and Γ_{31},Γ_{32} is the decays from $|3\rangle$ to any of the other states.*

Ladder Scheme

While the Lambda scheme is very robust and works in most cases as long as the condition of $|1\rangle \rightarrow |2\rangle$ being dipolar forbidden is met, the ladder scheme behaves slightly different. The scheme has, in the general sense, no metastable dark state and hence no EIT behavior in the strict sense. However, by utilizing a Rydberg state as the high lying energy state of the system the long lifetime of such a state effectively makes the intermediate state act as a metastable dark state.

In the picture of an ultracold atomic ensemble with negligible velocities of the atoms, the Ladder scheme works similarly to the lambda scheme. Here the intermediate state is split in the dressed state picture and the ground to intermediate state exhibits EIT behavior as the resonance is shifted.

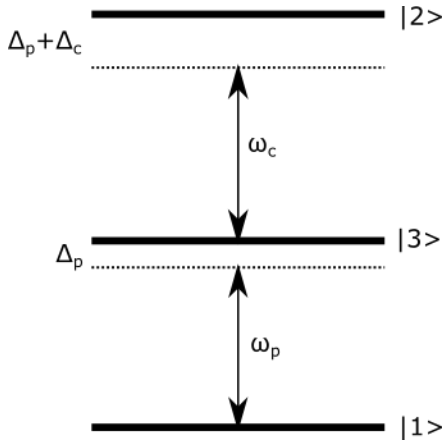

Figure 1.6: *Ladder EIT scheme with three level and the $|1\rangle \rightarrow |2\rangle$ forbidden by selection rules. $\omega_{c,p}$ is the control and probe frequencies, $\Delta_{c,p}$ the respective detunings from resonance.*

1.4.3 Rydberg Physics

A Rydberg state is a state with a high principal quantum number. In this work, a Rydberg state is defined as having a principal quantum number of $n \geq 20$ as these are the states we can reach using our control laser to excite from the $5P_{3/2}$ state. The highly excited Rydberg atom is very close to the ionization energy of the atom and is hence very sensitive to electric fields. The sensitivity stems from the polarizability which scales as n^7 for Rydberg atoms. Fields of just a few $\frac{kV}{cm}$ are sufficient to ionize any Rydberg atom created in the context of this thesis [32]. This effect can be utilized to remove any existing Rydberg atoms from the atomic ensemble in between repetitions of the experiment.

Rydberg states are very long-lived with $n \geq 70$ states having lifetimes $\tau \geq 1\,\text{ms}$ and the lifetime overall scaling with the principal quantum number as n^3 [9, 33].

Rydberg states can be reached via single-photon transitions. Transitions from low-n to high-n states require lasers in the UV spectrum for rubidium. UV-lasers are highly non-trivial to make and results in fully Doppler broadened transitions. This approach is thus limited in the practical sense. Alternatively, a two-photon transition can be utilized. This requires two lasers, often of much more convenient wavelengths, and is the scheme used for this work. The transitions utilized in this work are shown in figure 1.2 with the Rydberg state being either $20S_{1/2}$ or $30S_{1/2}$ for the vapor cell experiment and $121S_{1/2}$ for the phase measurements. In theory, any number of photon transitions can be utilized but the laser setup becomes increasingly complicated with each transition. The three-photon transition has some advantages as it can eliminate recoil and Doppler broadening effects [34].

Due to the high polarizability of Rydberg atoms, which makes them very sensitive to electric and magnetic fields, Rydberg atoms are also very sensitive to the presence of other Rydberg atoms. This gives rise to the so called Rydberg blockade [12]. The blockade effect can be understood by considering two atoms in the pair basis. In such a system there is four possible states: $|gg\rangle$, $|gr\rangle$, $|rg\rangle$, $|rr\rangle$. Using a laser to couple from $|g\rangle \rightarrow |r\rangle$ with coupling Ω. With the states structured as they are listed above, the matrix of such a system would be

$$\begin{bmatrix} 0 & \Omega & \Omega & 0 \\ \Omega & E & 0 & \Omega \\ \Omega & 0 & E & \Omega \\ 0 & \Omega & \Omega & 2E + V_{int} \end{bmatrix} \tag{1.23}$$

The state $|gg\rangle$ couples to $|gr\rangle$ and $|rg\rangle$ with Ω. Similarly, $|gr\rangle$ and $|rg\rangle$ couple to $|rr\rangle$ with Ω. But for the $|rr\rangle$ state there is an additional term, V_{int}, which is present only for the two Rydberg atom states. This additional potential stems from the van-der-Waals force induced by the presence of another Rydberg atom. As a consequence, the transition is no longer on resonance and if V_{int} is much larger than Ω, the $|rr\rangle$ state is effectively decoupled from the system dynamics. That is the Rydberg blockade. The blockade feature is shown schematically in figure 1.7.

This makes it such, that no other Rydberg atoms can be excited within the blockade volume with radius r_B [35]. It is this effect of Rydberg atoms that make them of interest to us, and a promising tool for quantum information and quantum simulation [9].

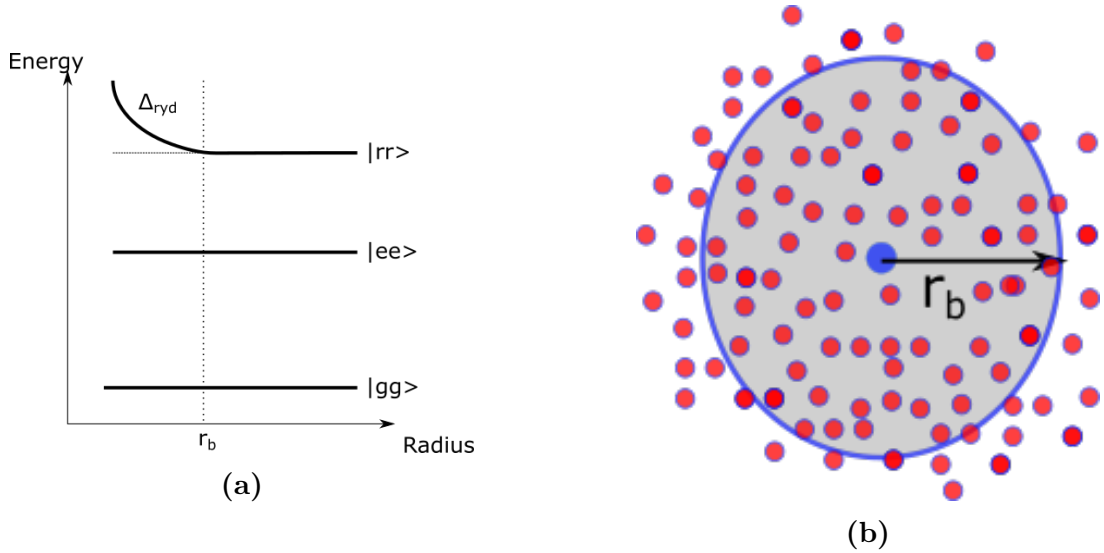

Figure 1.7: ***a)*** *Energy scheme of two atoms in the pair basis in the vicinity of one another. If one is excited to a Rydberg state the other experience a shift in its energy levels due to the van-der-Waals interaction of the first atom.* ***b)*** *Atomic ensemble of atoms (small red dots). The larger blue dot is a Rydberg excitation with its corresponding blockade radius r_b indicated by the blue circle.*

Chapter 2

Laser Locking to an External Cavity

Many fields of research in physics require stable lasers. This could be in the context of atomic clocks [5], or a newly realized novel set of constraints on dark matter candidates [6]. In our case, we use narrow linewidth lasers to probe atomic states for creating Rydberg atoms in atomic ensembles [36].

A laser is often referred to as a stable monochromatic light source emitting only a single frequency ω_0 at any point in time. In practice, such a perfect laser cannot be constructed and a laser always emits in a finite frequency range $\omega_0 \pm \Delta\omega$. In addition to a laser output not being perfectly monochromatic it also fluctuates in both intensity and frequency over time. The fluctuations occur around a mean value which itself can fluctuate and walk randomly. The slow fluctuation processes are driven by the environment in which the laser is located, i.e. depend on temperature, pressure, acoustics, and vibrations. Faster timescale fluctuations might also stem from the direct fluctuations of the laser medium itself. The noise can be classified in two categories, namely frequency independent noise, i.e. white noise, coming from quantum fluctuations and so called $1/f$ noise, f being the frequency, which is due to the technical limitations [24]. The aim of this work is to reduce the $\Delta\omega$.

To stabilize the frequency of a laser one must have a reference that is more stable than the laser itself. The frequency of the emitted light is actively stabilized by the use of a feedback loop. A measurement of the laser frequency relative to the frequency reference is used to create an error signal which is fed back into the laser. The internal electronics of the laser then adjust the output frequency accordingly. This can be done by adjusting the current over the main laser diode.

There exist multiple different solutions for a frequency reference with popular choices being a spectroscopy cell, in which you lock to an atomic resonance [37], or an ULE (Ultra Low Expansion) glass cavity, in which the laser is locked to a frequency supported by the cavity. For the work presented here the locking is done to a glass cavity. Both the ULE cavity and the laser lock are characterized in this chapter.
We wish to lock three lasers to this cavity by the use of the Pound-Drever-Hall technique, see section 2.1.2. The lasers have wavelengths of 780 nm, 960 nm and 1012 nm. These wavelengths each play key roles in working with rubidium atoms with the first two being used for the interferometer implementation presented in chapter 3.3 and the vapor cell EIT presented in chapter 4.

The 780 nm laser used for the work on this cavity is a home built DFB (Distributed Feedback) laser. This laser did not have sufficiently advanced electronics to implement a laser lock. Appropriate electronics could be build and this laser could be frequency

stabilized too. For real experiment implementation, we would lock a Toptica DLPro laser of this wavelength but any 780 nm laser is sufficient to perform the mode matching as explained later. The DFB laser is a very simple system but has a higher linewidth in free running mode than the more advanced cavity diode lasers [38]. This wavelength is used to excite rubidium atoms from the ground state $5S_{1/2}$ to the $5P_{3/2}$ excited state. This is referred to as the probe laser in this work. A properly locked laser for our purpose has a linewidth small enough to only hit a single hyperfine level of the excited state as shown in section 1.4

The 960 nm laser locked to this cavity is a TA-SHG laser from Toptica. This wavelength is used to couple atoms from the excited state to some higher lying Rydberg state and is regarded as the control laser in this thesis. The raw laser diode output of 960nm is coupled into the cavity. However, this laser has a TA (Tapered amplifier) and an SHG (Second Harmonic Generator) cavity which doubles the frequency through a non-linear process in a crystal [24]. The frequency doubled output of this exact laser is used for the vapor cell EIT experiment presented in chapter 4. The 960nm output is used for the cavity coupling as making mirrors of the required finesse at wavelength spanning more than the full visible spectrum is very difficult.

Finally, the cavity system should also be used for locking a 1012 nm laser. This will be used for a magic wavelength trap that has not yet been implemented in the experiment. A magic wavelength trap is an optical trap where the frequency of the trapping light is chosen such that the trapping potential is the same for atoms in both the ground and excited state of interest. For our purpose this happens when the polarizability of the ground state is approximately equal to that of a Rydberg state with principal quantum number n, i.e. $\alpha(\omega)_{5s} \approx \alpha(\omega)_{ns}$ [39]. Such magical wavelength traps have been implemented with success in other labs, for example, the lab of Kuzmich at the University of Michigan has shown its promising application in high-resolution spectroscopy, measuring the hyperfine splitting of Rydberg S-states in the range of $n = 30$ to $n = 65$ [40], and in quantum information science [41].

2.1 Theoretical background of Laser Stabilization

In this section, the theoretical knowledge required to set up a laser lock is presented. First, key equations for describing optical resonators are derived. This is followed by a derivation of the Pound-Drever-Hall (PDH) error signal. Finally, the theory of separating higher order modes in the resonator is presented.

2.1.1 Optical Resonators

The simplest optical resonator consists of two plane mirrors placed on an optical axis, z, separated by a distance L. Such a resonator is called a Fabry-Perot etalon [42]. One mirror is placed at the origin $z_1 = 0$ and the other at $z_2 = L$.

Within such a resonator lives a wavefunction given by

$$E(\boldsymbol{r},t) = \mathrm{Re}\left[E_0(\boldsymbol{r})\exp(i\omega t)\right], \tag{2.1}$$

where $E_0(\boldsymbol{r})$ is a complex amplitude that satisfies the Helmholtz equation

$$\nabla^2 E_0(\boldsymbol{r}) + k^2 E_0(\boldsymbol{r}) = 0, \tag{2.2}$$

with the wavevector $k = 2\pi\nu/c = \omega/c$. Such a resonator has the boundary conditions that, at the mirrors, the amplitude must equal zero, $E_0(\boldsymbol{r}) = 0$. The waves supported by such a Fabry-Perot etalon are those given by the solutions to the Helmholtz equation subject to the boundary conditions. The simplest form of solutions are the standing waves, also called modes, of the form

$$E(\boldsymbol{r}) = E\sin(kz). \tag{2.3}$$

Applying the boundary conditions the values of k are limited to a discrete set

$$k_q = \frac{\pi q}{L}, \qquad q \in \mathbb{N}, \tag{2.4}$$

where L is the separation distance of the mirror and q is a positive integer. This leads to an infinite set of solutions

$$E_q(\boldsymbol{r}) = E_q \sin\left(k_q z\right), \qquad q \in \mathbb{N}. \tag{2.5}$$

The discrete behavior of the wavevector leads to a discrete behavior of the supported frequencies due to the relation $k = 2\pi\nu/c$. Equation (2.4) leads to a similar expression in frequency

$$\nu_q = \frac{qc}{2L}, \qquad q \in \mathbb{N}, \tag{2.6}$$

which is the expression for the supported frequencies.
The Free Spectral Range (FSR) is defined as the distance, in frequency space, between two adjacent supported modes. [42]

$$\Delta\nu_{FSR} = \frac{c}{2L} \tag{2.7}$$

This equation depends only on the distance L between the resonator mirrors. Note that the c in these equations is the speed of light in between the mirrors. This becomes important if there is something other than vacuum between the resonator mirrors as the speed of light will have to be adjusted accordingly, $c_{vac} = c/n$.

In the case of perfect resonator mirrors the total standing wave inside the cavity can be expressed as the sum of all supported modes

$$E_{tot} = \sum_q E_q \sin\left(k_q z\right). \tag{2.8}$$

If the wave coupled into the cavity is of frequency exactly equal to a supported mode, all contributions inside the cavity will be perfectly in phase with respect to one another. However, in the case of none-perfect mirrors, each round trip leads to a probability of the wave not being reflected fully. We now assume for simplicity, that the cavity is symmetrical and each mirror has a reflectivity of R. A full round-trip will contribute with R^2 as the light will hit each mirror once. With the mode not matched perfectly to the resonance of the cavity, a slight change in phase will occur. The relation between round i and round $i+1$ is given by

$$E_{i+1} = hE_i, \qquad h = Re^{-i\phi}, \tag{2.9}$$

with $\phi = 2kL$ being the resulting phasor from a single round trip.
Writing up an infinite number of round trips all having h change in phase with respect to the previous round, the electric field takes the form

$$\begin{aligned} E &= E_0 + E_1 + E_2 + \cdots \\ &= E_0 + hE_0 + h^2E_0 + \cdots \\ &= E_0(1 + h + h^2 + \cdots) \\ &= \frac{E_0}{1-h}. \end{aligned} \tag{2.10}$$

The intensity of the wave in the resonator is the square of the electric and takes the form

$$\begin{aligned} I = |E|^2 &= \frac{E_0^2}{(1-h)^2} \\ &= \frac{I_0}{|1 - Re^{-i\phi}|^2} = \frac{I_0}{R^2\sin^2\phi + R^2\cos^2\phi - 2R\cos\phi + 1} \\ &= \frac{I_0}{R^2 - 2R\cos\phi + 1} = \frac{I_0}{(1-R)^2 + 2r(1-\cos\phi)} \\ &= \frac{I_0}{(1-R)^2 + 4R\sin^2\left(\frac{\phi}{2}\right)} \\ &= \frac{I}{(1-R)^2}\frac{1}{1 + \frac{4R\sin^2\left(\frac{\phi}{2}\right)}{(1-R)^2}} \\ &= \frac{I_{max}}{1 + \left(\frac{2\mathcal{F}}{\pi}\right)^2\sin^2\frac{\phi}{2}}. \end{aligned} \tag{2.11}$$

Here, $I_{max} = I_0/(1-R)^2$ has been introduced as the maximum intensity, with I_0 being the intensity of the initial wave. An important parameter called the finesse $\mathcal{F}$ has also been introduced and is given by the reflectivity as

$$\mathcal{F} = \frac{\pi\sqrt{R}}{1-r}. \tag{2.12}$$

This quantity is a measure of how many rounds the wave takes inside the resonator [43]. A plot of the intensity as a function of frequency shows a repeating pattern with the finesse determining the width of the resonance peak and the FSR the separation of the resonances. This is plotted in figure 2.1 with varying mirror reflectivity leading to different finesse.

To measure the finesse of a resonator one can utilize the decaytime after turning off the laser generating the standing wave inside the cavity. Due to the slight imperfection of the mirror there is a probability that part of the wave leaks out every time it encounters a mirror. This leads to an exponential decay with a characteristic time of τ

$$I(t) = I_0\exp\left(-\frac{t}{\tau}\right). \tag{2.13}$$

This is related to the finesse as

$$\mathcal{F} = \tau\frac{\pi c}{L}. \tag{2.14}$$

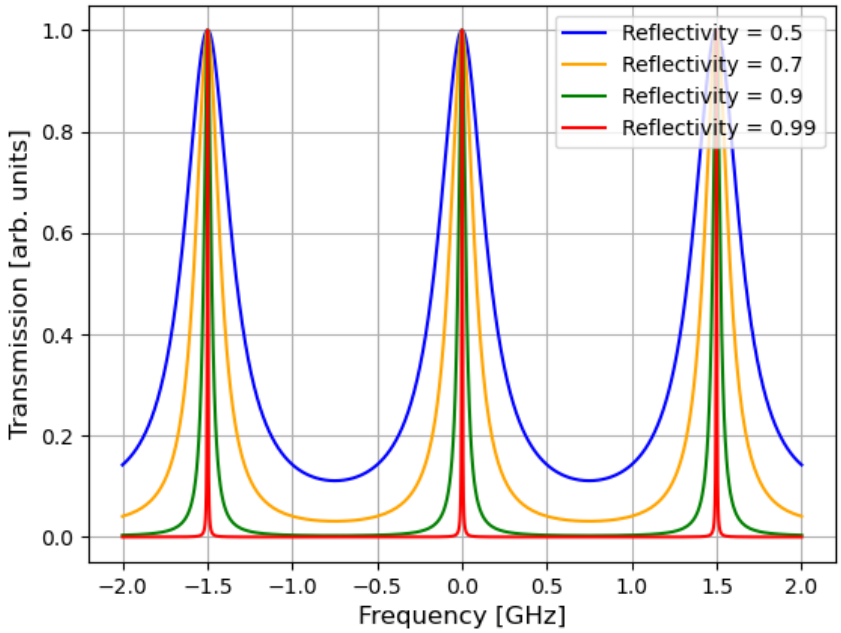

Figure 2.1: *Transmission as a function of frequency with an arbitrary zero point. A repeating pattern with periods giving by the cavity FSR is observed. The with of the peak is determined by the finesse of the cavity mirrors with higher finesse resulting in a more narrow transmission peak.*

The latter equation is related to the FSR, equation (2.7). The free spectral range describes the supported frequencies of the cavity, and considering a full round trip, it equates the fraction in equation (2.14). Multiplied by the decay time, i.e. how long a photon survives in the cavity, it becomes clear that the finesse describes how well the mirrors reflect.
In section 2.4.1 a measurement of the cavity finesse is presented.

Transmission and Reflection

So far we have studied the intensity *inside* the resonator and how this is related to the characteristics of the cavity, namely the FSR and finesse. With the knowledge of these quantities, it is possible to write a set of equations that describe the intensity of the reflected and transmitted signal respectively. The reflected and transmitted signals are assumed to be measured over time at some location outside the cavity. In practice, this is done with a photodiode.

To derive expressions for the reflected and transmitted intensity, consider the idealized case of a laser emitting a monochromatic wave $E_{in} = E_0 e^{i\omega t}$ of frequency ω and complex amplitude E_0. The reflected wave has the same frequency, but a different complex amplitude $E_{ref} = E_1 e^{i\omega t}$. The ratio between the reflected and the incoming wave leads to the following reflection coefficient assuming a lossless and symmetric cavity [44].

$$\mathcal{R}(\omega) = \frac{E_{ref}}{E_{in}} = \frac{\sqrt{\mathcal{R}}\left(e^{i\omega/\Delta\nu_{FSR}} - 1\right)}{1 - \mathcal{R}e^{i\omega/\Delta\nu_{FSR}}} \tag{2.15}$$

Here $\mathcal{R}$ is the reflectivity of the mirrors and $\Delta\nu_{FSR}$ is the free spectral range. The intensity of the reflected signal is the norm square of the product of the incoming field

and the reflection coefficient

$$I_{ref} = |\mathcal{R}E_{in}|^2 = I_0 \frac{\sin^2\left(\frac{\omega}{2\Delta\nu_{FSR}}\right)}{\left(\frac{\pi}{2\mathcal{F}}\right) + \sin^2\left(\frac{\omega}{2\Delta\nu_{FSR}}\right)}. \tag{2.16}$$

The reflected intensity is a coherent sum of two contributions. Namely the promptly reflected beam, i.e. the beam that never makes it into the cavity but is reflected from the back of the cavity mirror, and the leakage beam back out of the cavity. The leakage beam is made up of yet another sum of contributions from beams having undergone a different number of roundtrips in the cavity. For our situation of an ideal cavity with no losses the intensity of all contributions are the same but the phase of the promptly reflected and the leakage beam differs by 180°. This phase is imprinted when the beam is promptly reflected. Therefore, for frequencies close to the cavity resonance, the two contributions interfere destructively and cancel, giving rise to a dip in the reflected intensity as shown in figure 2.2. The larger the finesse of the cavity, the lower a frequency range will be supported, hence the frequency range for which a leakage beam can result in destructive interference is reduced. The phase of the reflected signal is seen to change sign whenever the cavity resonance is crossed. The highest phase shift is just around cavity resonance.

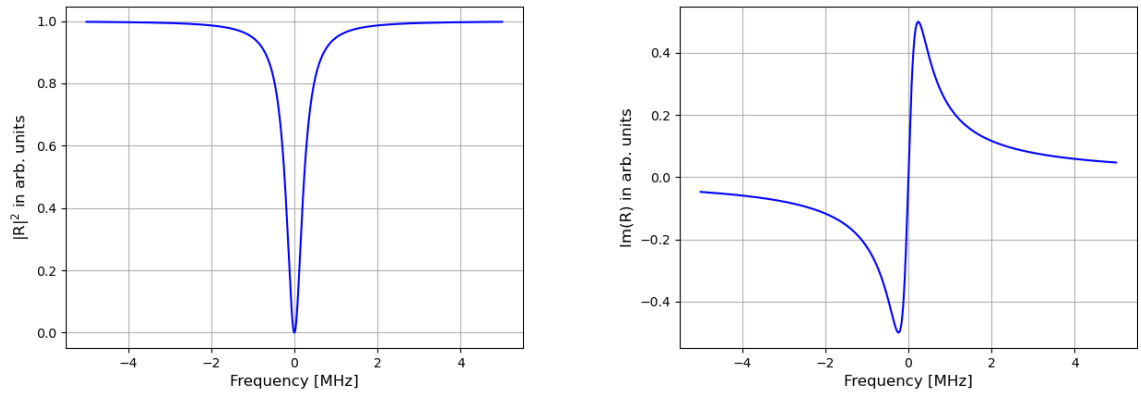

(a) *Intensity of the cavity reflection signal.* **(b)** *Phase of the cavity reflection signal.*

Figure 2.2: *The reflection coefficient for a symmetric lossless cavity.* ***a)*** *is the intensity of the signal with a dip around resonance due to destructive interference, and* ***b)*** *is the phase change of the reflected signal which changes sign when crossing resonance. The calculations are done using specification parameters of cavity length* $L = 100.1\,\text{mm}$ *and a finesse* $\mathcal{F} = 20000$

By studying the transmitted signal using a similar approach an expression for the intensity of this signal can be obtained

$$I_{trans} = I_0 \frac{1}{1 - \left(\frac{2\mathcal{F}}{\pi}\right)^2 \sin^2\left(\frac{\omega}{2\Delta\nu_{FSR}}\right)}. \tag{2.17}$$

This equation has a periodic pattern with a period of the FSR. The width of the peak occurring at each FSR is given by the prefactor which includes the finesse.

Degeneracy of cavity modes

Up until this point the discussion has focused on the standing wave solutions, equation (2.3), to the Helmholtz equation, equation (2.2). However, the simple fundamental Gaussian mode is not the only set of solutions to the Helmholtz equation. In fact, two additional families of solutions exist. These are the Hermit-Gaussian and the Laguerre-Gaussian beams. They both share the parabolic wavefront feature of the Gaussian beam but have different intensity distributions. They both have the property that their 0th order corresponds to the Gaussian beam. While the Hermite-Gaussian solutions stem from solving the paraxial Helmholtz equation in Cartesian coordinates the Laguerre-Gaussian solutions are obtained by writing it in cylindrical coordinates (ρ,ϕ, z) [42]. This indicates that Laguerre-Gaussian modes are the ones surviving in a spherical resonator like the one used for this thesis.

For both sets of solutions, it is important to take the Gouy phase, ζ, into account. This is a phase shift that occurs due to the Gaussian nature of the wavefront and the fact that this differs from a plane wave.

$$\zeta(z) = \arctan \frac{z}{z_R} \tag{2.18}$$

The Gouy phase is defined as in equation (2.18) with z_R being the Rayleigh range. A plot of this equation for a cavity of fixed length similar to that used for our setup is shown in figure 2.3, with the red line being a phase shift of $\pi/2$, the blue being the Gouy phase shift, and the orange cross being the point corresponding to the mirror curvature in our setup.

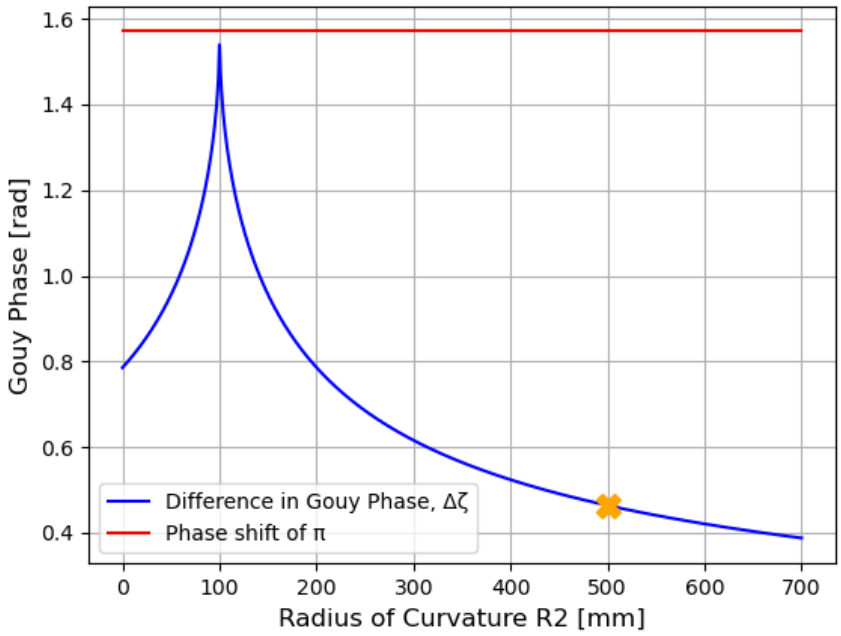

Figure 2.3: *Gouy Phase for a fixed cavity length of* 100.1 mm. *The blue curve is the Gouy Phase, the red line a shift of* $\pi/2$ *and the orange cross the point corresponding to our setup. Degeneracy, i.e.* $\pi/2$ *phase shift occurs at curvature equal to cavity length.*

It can be seen from this figure that degeneracy, i.e. a phase shift of $\pi/2$ occurs at cavity length equal to the curvature of the second mirror. This is undesired for laser locking as there will be multiple modes to which the locking can be performed.

The Gouy phase becomes important when taking higher order modes into account because these acquire different phase shifts and will therefore become separated in frequency space. When looking at Hermite-Gaussian modes, characterized by two transverse indices (l,m) and a single longitudinal mode q, the difference in frequency of the supported modes become [42]

$$\nu_{q,l,m} = q\Delta\nu_{FSR} + (1 + l + m)\,\frac{\Delta\zeta}{\pi}\Delta\nu_{FSR}. \tag{2.19}$$

With $\Delta\zeta$ being the relative Gouy phase at mirror one and two respectively. A quick check shows that this equation is consistent with previous calculations as there is a single FSR between two different longitudinal modes q, q'. By looking at the difference of two transversal modes (l, m) and (l', m') the frequency separation between higher order transversal modes can be calculated.

$$\nu_{q,l,m} - \nu_{q,l',m'} = [(l - l') + (m - m')]\,\frac{\Delta\zeta}{\pi}\Delta\nu_{FSR}. \tag{2.20}$$

Here the dependency on the longitudinal mode drops out. Taking the fundamental (0,0) mode and the first higher order mode (0,1) the frequency separation can be calculated to be 221 MHz.

While the above are true for Hermite-Gaussian modes the equations change slightly for the Laguerre-Gaussian modes. The line of thought and the Gouy phase calculation remains the same but the scaling on mode numbers change slightly [45]. The mode is now characterized by a different set of indices as the coordinates are now cylindrical. The Laguerre-Gaussian modes are denoted L_p^l with mode numbers (p, l) with p being the radial and l the azimuthal index. Equation (2.19) now takes the form

$$\nu_{p,l} = q\Delta\nu_{FSR} + (1 + |l| + 2p)\,\frac{\Delta\zeta}{\pi}\Delta\nu_{FSR}. \tag{2.21}$$

Here q is an integer number as for the Hermite-Gaussian [46]. Calculating the difference between two modes results in an equation similar to that of the Hermite-Gaussian with the indices being the only difference

$$\nu_{p,m} - \nu_{p,m'} = [2(p - p') + (|l| - |l'|)]\,\frac{\Delta\zeta}{\pi}\Delta\nu_{FSR}. \tag{2.22}$$

The calculation of the frequency difference between the two modes (0,0) and (0,1) is identical for the Hermite and Laguerre Gaussian. In section 2.4.3 the experimental results of measuring the separation of modes for our cavity are presented.

2.1.2 Pound-Drever-Hall Locking Technique

This section goes through the theoretical background of the Pound-Drever-Hall technique (PDH). The PDH technique was developed by R.V. Pound, Ronald Drever, and John L. Hall in 1983 [2] and proved to be a milestone for obtaining ultra-narrow linewidth lasers at a sub Hz level [3,4]. The game-changing factor of this new way of locking a laser is the use of the reflected signal as opposed to the traditional use of the transmitted signal of the cavity to which the laser is locked [47]. By utilizing the reflected signal it is possible to

separate intensity fluctuations of the laser itself and of its alignment into the cavity [44]. The PDH locking technique utilizes an error signal with a steep slope to which the laser is locked. In the following, a mathematical formulation of the error signal is derived.

If the laser is swept in frequency over a cavity resonance the resulting error signal will have a parabola shaped intensity profile. Since the parabola is symmetric around the cavity resonance it cannot be used to distinguish whether the laser frequency is higher or lower than the resonance frequency. However, the derivative of the parabolic signal contains this information. To obtain this information the incoming laser beam is modulated by applying sidebands with a definite phase relation to the carrier frequency. When light with frequency ω is subject to modulation of amplitude β and a phase Ω the resulting electric field takes the form:

$$\begin{aligned} E_{in} &= E_0 e^{i(\omega t + \beta \sin \Omega t)} \\ &= E_0 e^{i\omega t} \sum_{-\infty}^{\infty} J_n(\beta)\, e^{in\Omega t} \\ &\approx E_0 \left[J_0(\beta)\, e^{i\omega t} + J_1(\beta)\, e^{i(\omega+\Omega)t} - J_1(\beta)\, e^{i(\omega-\Omega)t} \right] \end{aligned} \tag{2.23}$$

Here the expression has been expanded in terms of the Bessel functions $j_i, i \in 0{,}1$ and weak modulations of amplitude $\beta \ll 1$ is assumed [48]. From the last expression it becomes evident that the incoming light consists of a carrier with frequency ω and two sidebands with frequency $\omega \pm \Omega$. The signal on the reflection photodiode can be calculated by treating the reflection from the cavity mirrors as three distinct components with the mirror reflectivities, $\mathcal{R}(\omega)$, being frequency dependent.

$$E_{ref} = E_0 \left[\mathcal{R}(\omega)\, J_0(\beta)\, e^{i\omega t} + \mathcal{R}(\omega+\Omega)\, J_1(\beta)\, e^{i(\omega+\Omega)t} - \mathcal{R}(\omega-\Omega)\, J_1(\beta)\, e^{i(\omega-\Omega)t} \right] \tag{2.24}$$

The photodiode always measures intensity which is the norm square of the reflected electric field. The measured signal becomes

$$\begin{aligned} P_{ref} =& |E_{ref}|^2 \\ =& J_0^2(\beta)\, P_0 |R(\omega)|^2 + J_1^2(\beta) P_0 \left(|\mathcal{R}(\omega+\Omega)|^2 + |\mathcal{R}(\omega-\Omega)|^2 \right) \\ &+ 2J_0(\beta) J_1(\beta) P_0 \,\mathrm{Re}\left[\mathcal{R}(\omega)\mathcal{R}^\star(\omega+\Omega) - \mathcal{R}^\star(\omega)\mathcal{R}(\omega-\Omega) \right] \cos \Omega t \\ &+ 2J_0(\beta) J_1(\beta) P_0 \,\mathrm{Im}\left[\mathcal{R}(\omega)\mathcal{R}^\star(\omega+\Omega) - \mathcal{R}^\star(\omega)\mathcal{R}(\omega-\Omega) \right] \sin \Omega t \\ &+ \mathcal{O}(2\Omega)\,. \end{aligned} \tag{2.25}$$

This signal consist of terms oscillating at ω and $\omega \pm \Omega$ which is the carrier and sideband frequencies as usual. It also consists of two terms oscillating at Ω which stems from the interference effects between the carrier and sideband fields. The 2Ω terms have not been written explicitly but they represent the interference between the two carrier frequencies and are thus neglected, as small modulation amplitudes have been assumed.

By mixing the reflection signal with the modulating frequency and comparing the relative phase of the two signals, it is possible to deduce an error signal for the laser frequency relative to the cavity frequency. In practice, the reflection signal given in equation (2.25) goes through a low-pass filter and a phase-shifter before being mixed with the modulation frequency.
The mixer is, mathematically, taking two input signals and outputs the product of the two. The low-pass filter isolates the low frequency components of the signal and the

phase-shifter compensates for the delays in signal paths of the two signals.
In the case of fast modulations, i.e. $\Omega \gg \Delta\nu_{FSR}/\mathcal{F}$ the final error signal reads

$$P_{ref} = -2J_0(\beta)J_1(\beta)P_0 \,\mathrm{Im}\left[\mathcal{R}(\omega)\mathcal{R}^\star(\omega+\Omega) - \mathcal{R}^\star(\omega)\mathcal{R}(\omega-\Omega)\right]\sin\Omega t. \tag{2.26}$$

In section 2.5 the locking of a 960 nm laser will be discussed. For this laser the modulation frequency is set internally, using the laser controller, to $\Omega = 25\,\mathrm{MHz}$. The free spectral range of the cavity is $\Delta\nu_{FSR} = 1.5\,\mathrm{GHz}$ and the finesse is set to 20000. This leads to an inequality $\Delta\nu_{FSR}/\mathcal{F} = 1.5\,\mathrm{GHz}/20000 \approx 75\,\mathrm{kHz} \ll \Omega$. In this case the fast modulation limit of equation (2.26) is applicable.
For these parameters, the error signal takes the form of that in figure 2.4.

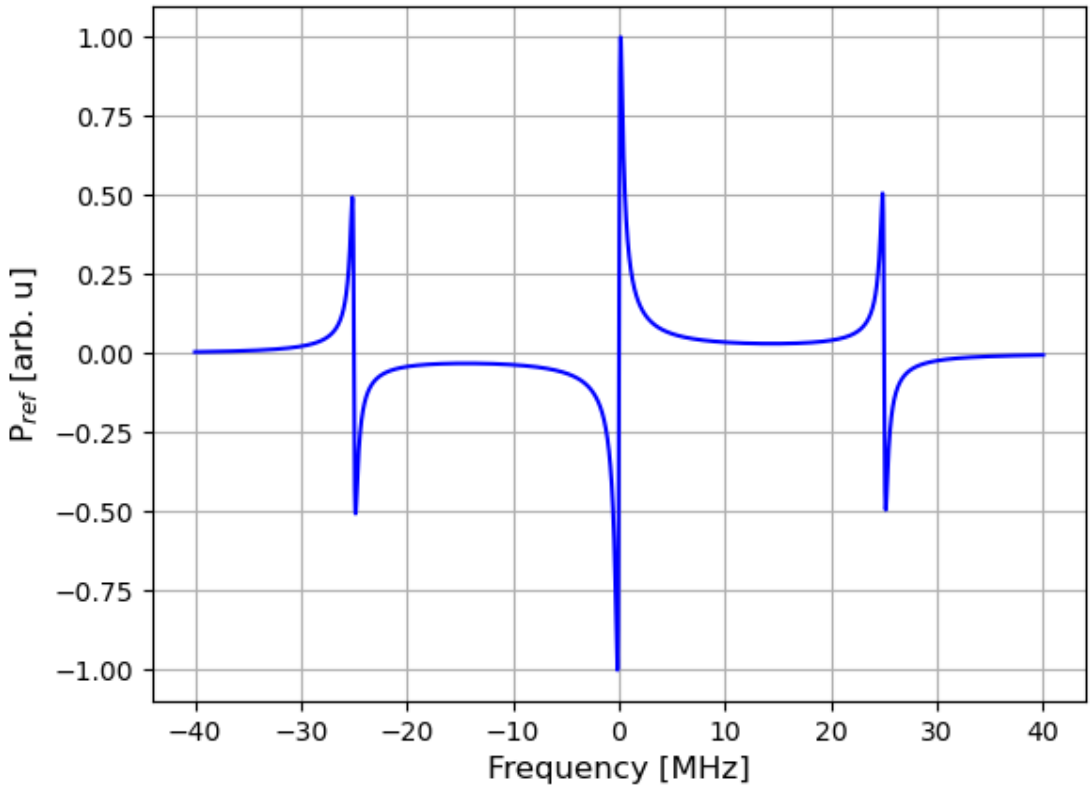

Figure 2.4: *Theoretical PDH signal for the experiment parameters of* $\Delta\nu_{FSR} = 1.5\,\mathrm{GHz}$ *and* $\mathcal{F} = 20000$. *The modulation frequency is* $25\,\mathrm{MHz}$.

This signal has the property of the steep slope around the cavity resonance which allows for very narrow laser locking. Due to the very steep nature of the error signal only a small deviation in frequency is necessary to obtain a clear change in the value of the error signal.

2.2 Alignment of the Cavity in Cavity Housing

In this section, the procedure of aligning the cavity and the cavity housing is presented. The cavity used here is a commercial solution from Stable Laser Systems[1], consisting of the cavity itself and a vacuum housing for the cavity. To ensure optimal conditions for the cavity it is not attached but rather rests on small Viton balls. The lack of attachment results in freedom related to both the position and the angle of the cavity with respect to the housing. It is essential that the cavity is placed straight with respect to the longitudinal axis and to know the exact position relative to the front panel of the housing. The position of the cavity determines the position of the lens in front of the cavity which is an essential part of obtaining a good coupling of the light, see section 2.3.

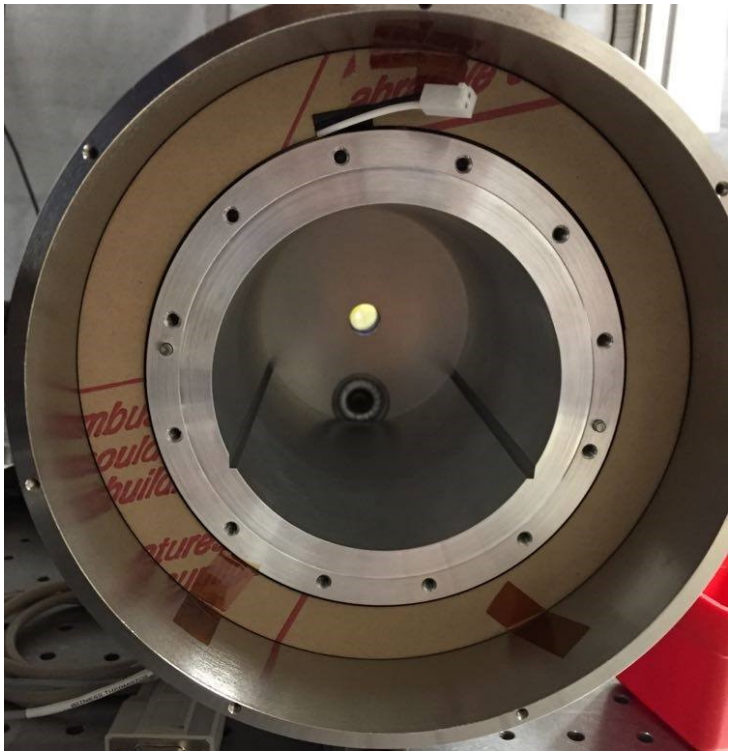

Figure 2.5: *Picture of the cavity housing with the lid and front panel isolation taken off. The hollow core is where the ULE cavity is inserted. The connector on top is for the temperature regulation placed inside the isolation material.*

A picture of the open cavity housing before the insertion of the ULE cavity can be seen in figure 2.5. This cylindrical cavity housing consists of a hollow center in which the cavity is placed. Around the center is a layer of isolation material with wires that can be used for precise temperature stabilization using a temperature controller[2]. The cavity comes with a calibration sheet in which the temperature resulting in the lowest expansion of the ULE glass can be found. This is individually calibrated for each product and the optimal temperature for our cavity is 36.65 °C. The cavity housing also comes with pipes onto which appropriate vacuum pumps can be attached. The windows at the front and back panel of the cavity housing are tilted by 2 degrees to avoid echelon effects from the

[1] stable laser systems model VH6010-4
[2] Wavelength Electronics, model: LFI-3751

windows.

Before placing the cavity housing, a He-Ne laser of wavelength 632.8 nm was aligned to be exactly on top of a line of holes using two apertures and corresponding mirrors for adjustment. Since the wavelength of a He-Ne laser is far away from those that should be locked to this cavity, the coatings on the windows are not designed for this wavelength, allowing both transmission and reflection. Having a visible transmission through the cavity housing helps to put it exactly straight. Due to the tilted windows, the back reflection cannot be used to get a perfect orthogonal placement. Instead, the housing was placed such that the laser beam entered and exited from the center of the windows resulting in a cavity housing placed exactly on top of the line of holes. Once the housing was in place the lid could be taken off and the ULE cavity inserted. Since the cavity is only resting inside the housing, the housing should not be moved after the cavity has been installed. Otherwise, the cavity might move around inside damaging both the housing and the cavity.

When inserting the ULE cavity all work had to be done with great care and vacuum cleaned equipment. A single fingerprint or a gram of dust from a tool has the potential of greatly reducing the quality of the vacuum and should thus be avoided.

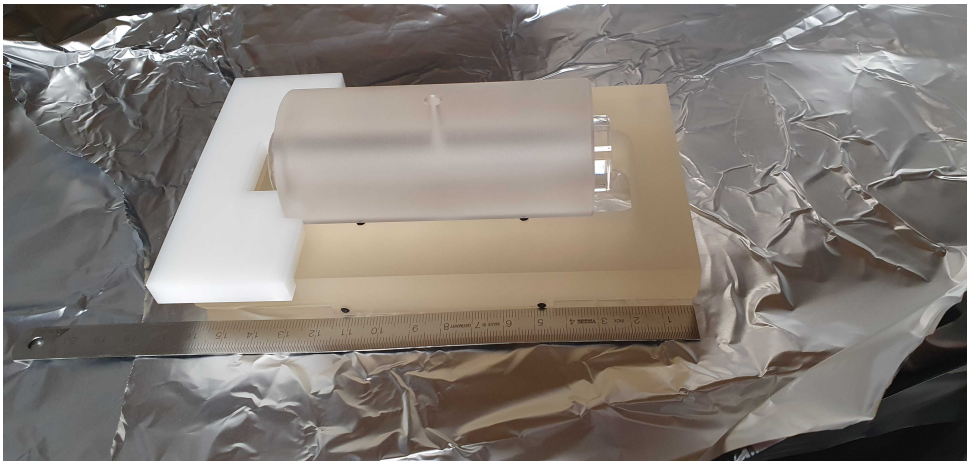

Figure 2.6: *Picture of the ULE cavity put onto the square glass mount. The white piece is an alignment tool provided by Stable Laser Systems and is thus removed upon placement of the cavity inside the housing. Four Viton balls on each side of the mount ensure stability from vibrations. The cavity is placed in the center of the mount.*

The cavity is seen in figure 2.6. The white piece is an alignment tool provided by Stable Laser Systems that helps to ensure a center and non-tilted placement of the cavity in the mount. It is important to place it in the center of the glass mount and to place the glass mount in the center of the housing as this will result in the least vibrations. It also turns out that by placing the cavity in the center the first mirror location almost coincides with a screw on the outside of the housing making it easier to get the proper distances for the mode matching. Once the cavity is in place and the housing is sealed it should be pumped under vacuum. A vacuum environment is the best suited for a stable cavity as any interaction will molecules or atoms will scatter the light.

In this work, the cavity was not pumped. For an undamaged cavity vacuum around 10^{-11}hPa is expected. For this cavity a pressure of 10^{-6}hPa was obtained which is many orders of magnitude larger than the expected pressure. The suspicion is that the flange

has been damaged when closing the housing after inserting the cavity. Testing the vacuum requires a turbopump which was not available after the initial pumping. The chamber not being under vacuum turns out to be a limiting factor to the laser lock as explained in section 2.5.

2.3 Mode matching

After aligning the cavity inside the housing the lens design to ensure the best possible coupling can be designed. The optical setup around the cavity can be build once the lenses are known.

Mode Matching
To achieve perfect coupling into the cavity the criteria for mode matching have to be met. To achieve perfect mode matching into a plano-concave cavity the curvature of the Gaussian beam at the position of the curved mirror must match exactly that of the mirror. The light passes through the curved mirror when coupling into the cavity. Therefore, it is important to take this into account when designing the setup. Such a plano-concave piece of glass acts as a plano-concave lens of focal length

$$f = -\frac{R}{n-1}, \tag{2.27}$$

with R being the radius of curvature and n the refractive index of the glass.
A lens, called the mode matching lens, must be chosen such that, for fixed distance between the cavity mirrors and spacial constraints given by the cavity housing, the curvatures match the criteria for mode matching. This design process was carried out in the Gaussian Beam Calculator program and is shown in figure 2.7 for the 960 nm laser. The radius of curvature is known from the spec sheet to be $R_2 = 500\,\text{mm}$ and equation 1.10 is used to find the corresponding waist at the plane mirror. The outcoupling lens and mode matching lens, as well as the position of the latter, is determined by trial and error.

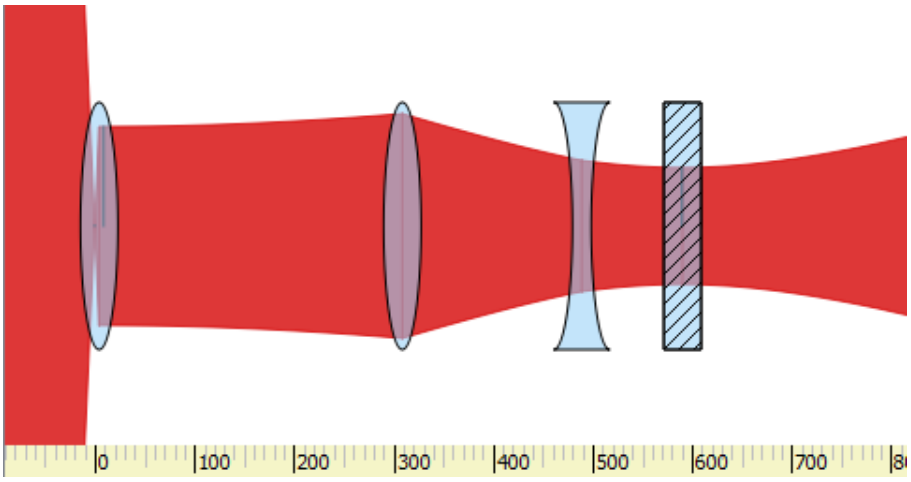

Figure 2.7: *Mode matching design for the* 960 nm *laser. The outcoupling lens is followed by the mode matching lens focusing on the plane mirror after passing through the curved mirror acting as a plano-concave lens of focal lens* $f \approx -1000$.

The 960 nm laser is chosen as the primary wavelength for which the fiber outcoupling lens is adjusted to give a collimated beam. Similar designs were made for the other two lasers, however, the mode matching lens position relative to the cavity was fixed by the 960 nm laser design. The wavelength-dependent focusing of a Gaussian beam, presented in section 1.2, requires the 780 nm and 1012 nm laser to be either converging or diverging when incident on the mode matching lens. This is adjusted with the outcoupling lens and puts stringent length requirements on the beam paths. For the 780 nm laser a full 345 mm should be between the outcoupler and the mode matching lens. This is amble of space. However, for the 1012 nm laser there is only 232 mm which is just enough to fit in the desired pieces of optics. However, if the setup is ever extended to support two rubidium quantum optics experiments with separate sets of lasers, fitting another 1012 nm laser in this space will pose a challenge.

Optical Layout

Depending on the number of lasers and the wavelengths of these the setup on the front end of the cavity may change. For lasers of very similar wavelength, the two beams can be overlapped with a PBS ensuring opposite polarization such that the beams do not interfere with each other [43]. In this thesis a 780 nm, 960 nm and 1012 nm laser were coupled into the same cavity. Since the three different wavelengths are relatively far apart, it is possible to use appropriate dichroic mirrors to overlap them. The setup is illustrated in figure 2.8.

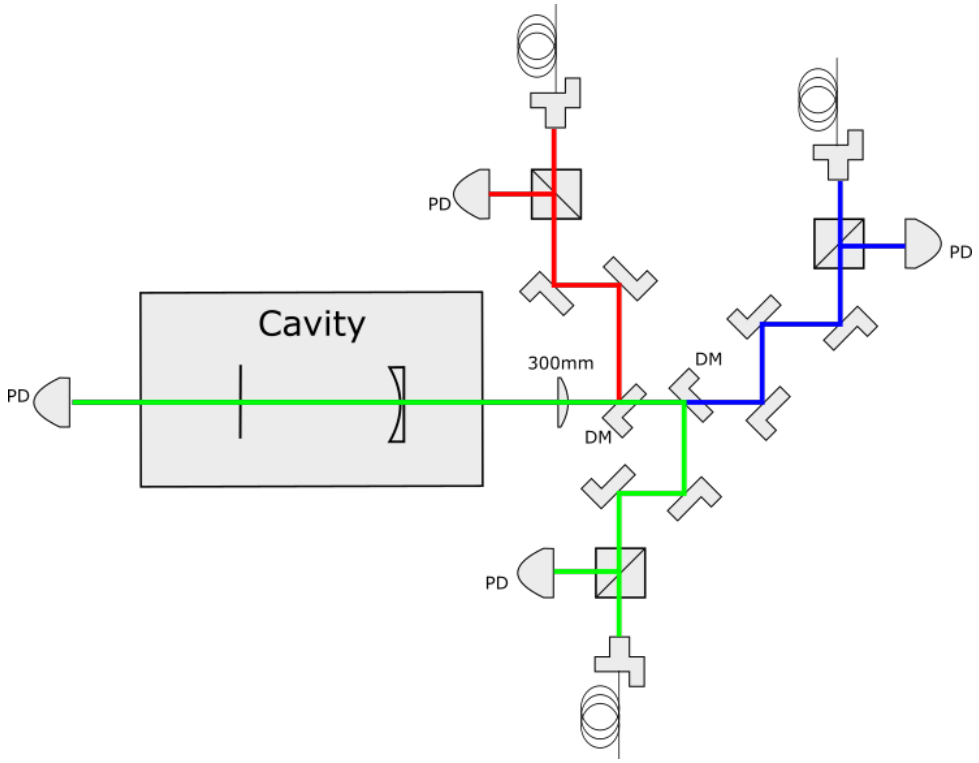

Figure 2.8: *Illustration of the optical setup in front of the cavity. A* 300 mm *lens is used to properly focus the beam on the curved mirror. The beamsplitter cube is used to send the reflected signal onto the photodiodes. It is these photodiodes that measure the signal used for the PDH error signal. The centerline optics is on non-adjustable mounts and the two mirrors in each arm are used to align the beam.*

Since a dichroic mirror will change the beam pointing ever so slightly, as it is a piece of glass through which light is transmitted, these have to be placed first.

As seen in figure 2.8 a single incoupling arm consists of an outcoupler, a beamsplitter used to send the reflected signal to a photodiode, two adjustable mirrors, and a mode matching lens focusing into the cavity.
For future expansions of this system to account for an extra laser of each wavelength, the beamsplitter should be replaced with a PBS. A waveplate, BS, photodiode, and an outcoupler would have to be placed such that spatial requirements are still fulfilled such that optimal coupling can still be achieved. A suggestion for such a design is shown in figure 2.9.

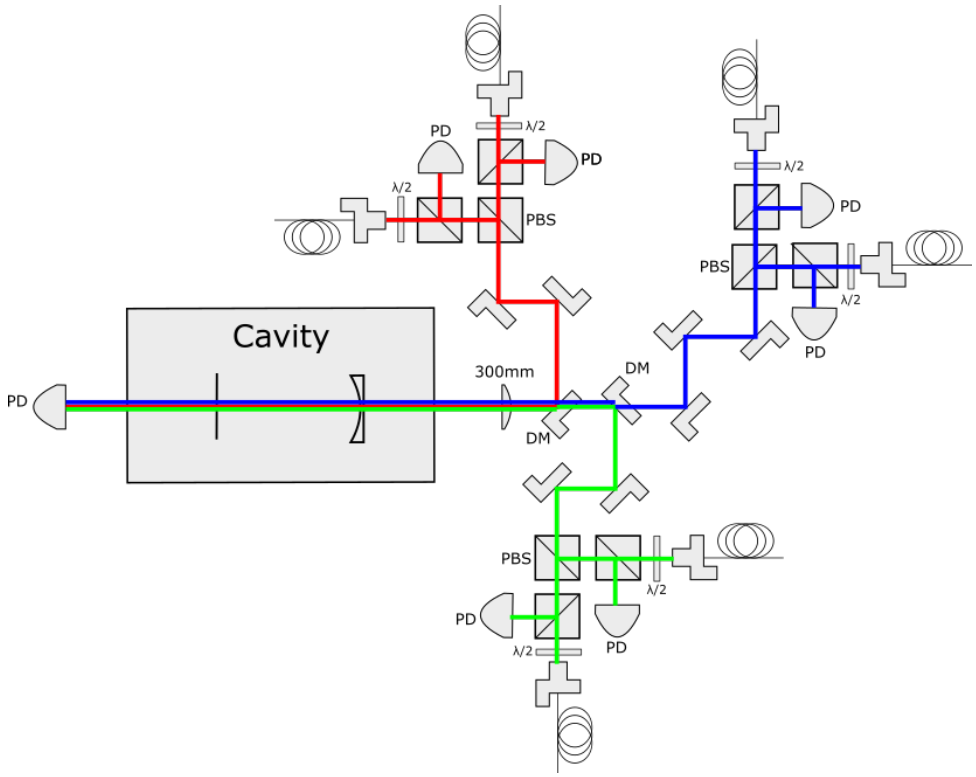

Figure 2.9: *Suggestion for a 6 lasers layout in front of the cavity. Each optical path now has two components overlapped using a PBS.*

Obtaining a signal from the cavity

It can be challenging to find the initial signal through the cavity. To overcome this, the aforementioned He-Ne laser was used. The He-Ne laser was sent through the cavity from the flat-mirror side and overlapped with the primary wavelength at the front end of the cavity. Using this trick a signal was easily obtained.

To have optimal coupling into the cavity the aim is to align such that only the fundamental TEM_{00} Gaussian mode survives. To obtain this, a camera[3] and a photodiode, connected to an oscilloscope, are used. A setup with a 50:50 beamsplitter behind the cavity is used to have a signal on the photodiode and camera simultaneously.

The laser is scanned over a free-spectral range, i.e. 1.5 GHz, to make sure there is a cavity resonance somewhere throughout the scan. When aligning on the camera a scan

[3]Unibrain Fire-i

rate of a handful of Hz is used. For the photodiode alignment, a scan rate of 25 Hz was used. The exact scan rate does not matter but should be picked depending on the refresh rate of the camera/detector.

First, the camera is used to obtain a signal of the transmitted light. The first signal is often some higher order mode. Aligning on the two incoupling mirrors should lead to a signal of the fundamental mode which has the form of a dot. A variety of surviving higher order modes have been seen during the alignment process and are shown in figure 2.10.

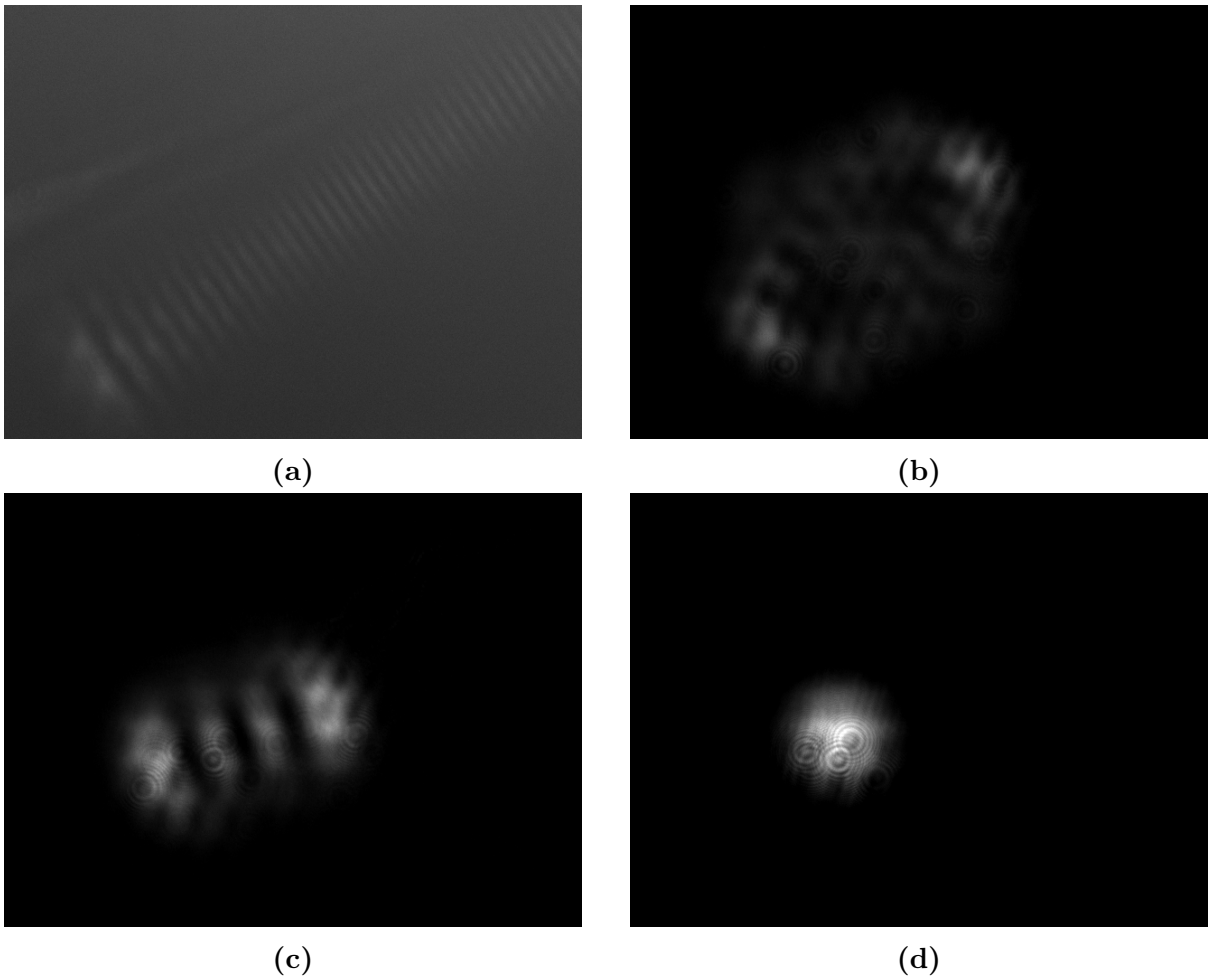

Figure 2.10: *A variety of Gaussian modes seen during the cavity alignment.* ***a)*** *is a very high order mode.* ***b)*** *is still a high order mode but closer to the fundamental than* ***a****.* ***c)*** *is identified as the* (1,1) *Laguerre-Gaussian mode.* ***d)*** *is the fundamental Gaussian mode*

It is not possible to align purely on the camera as the fundamental mode will saturate the camera and a signal of a few higher order modes might remain, though not visible. For this purpose, a photodiode connected to an oscilloscope is used. If the fundamental mode is visible on the camera it should be the higher peak on the oscilloscope. It will have a peak for every mode that lives inside the cavity. The alignment is optimized by minimizing all transmission peaks except for the fundamental Gaussian mode. In this project, the alignment was considered optimal when the higher order modes were at less than 1% of the intensity of the fundamental mode. At optimal coupling, the intensity of

the higher order modes was on the order of the noise on the photodiode.
Having aligned into the cavity, the optical setup for laser locking is in place and it is possible to generate an error signal for locking.

2.4 Cavity Characterization

In this section, the cavity is characterized using the 960 nm and 1012 nm laser. Three quantities have been examined. First, the finesse of the cavity is measured to characterize the resonator mirrors. Secondly, the free spectral range is measured to know the exact length of the cavity. These two quantities were measured using the 960 nm laser. The mode separation is measured to get the distance in frequency space to higher order Gaussian modes. This was done using the 1012 nm laser.

2.4.1 Finesse

Once a laser is locked there is a very simple way of measuring the finesse. The finesse is a measure of how good the mirrors reflect and is thus directly related to the lifetime of a photon inside the cavity. The mathematical relation was derived in equation 2.13 and 2.14. The finesse is measured by locking the laser such that the highest possible transmission is obtained and then kicking it far away from resonance preventing more light from being coupled into the cavity. The amplified photodiode measuring transmission will observe an exponential decay in intensity as light is leaking out of the cavity while nothing is coupled in. From this data, the lifetime τ can be determined via an exponential fit. In this specific measurement, a function generator was used to apply a 200 μs square pulse of amplitude 100 mV to the FALC 110 module. The module responds by rapidly changing the frequency of the laser which moves it off cavity resonance. The result of this is shown in figure 2.11.

This figure shows a full transmission decay (blue) with the laser locked initially, followed by the exponential decay after the laser has been knocked out of lock. The orange part of the dataset is used for the fitting of the red line. The first data of the decay is not included in the fit since the PID controller is still trying to keep the laser locked and the decay is not perfectly exponential. The exponential part of the decay is determined by looking for the linear part in a semi-log representation. Using equation (2.13) and (2.14) the finesse is determined to be just short of 20000. This is in the high end of the specifications for the used cavity, in which the finesse is stated to be between 5000 and 20000. To get a slightly more accurate measure of the finesse a possible next step in the analysis would be to fit a linear curve to the semi-log data and find the optimal range of data to include in the fit.

Further work using the same approach is required to fully characterize the cavity. The finesse is greatly dependent on the coating of the mirrors and is most certainly not the same for all three wavelengths. Performing such measurements does, however, require the lasers to be locked to the cavity, hence they were not performed for the 780 nm and 1012 nm laser.

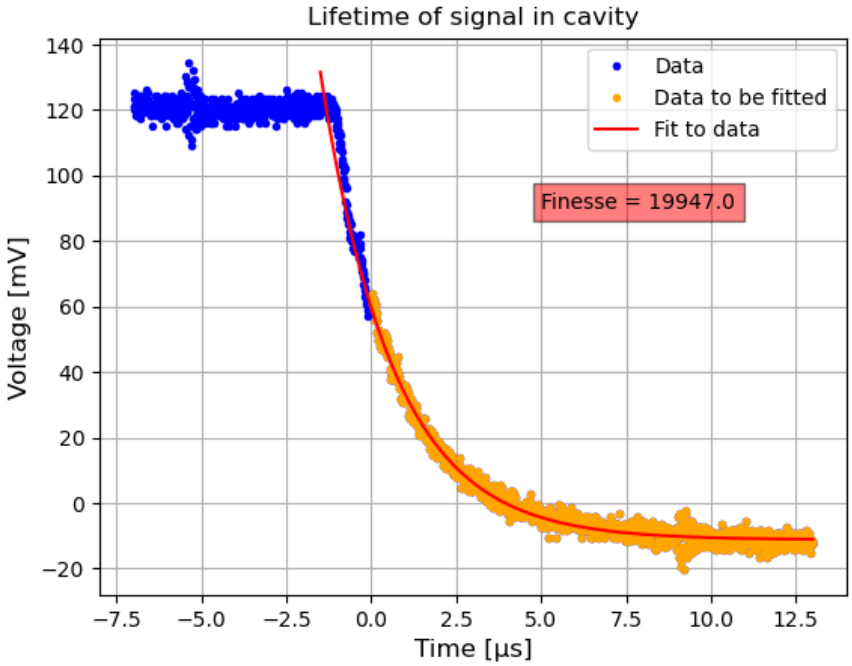

Figure 2.11: *Transmitted intensity through the cavity of the* 960 nm *laser. The blue is the full transmitted signal, the orange is the fitted data and the red curve is the fit of equation* (2.13)*. The finesse is determined to be just short of 20000*

2.4.2 Free Spectral Range

In this section the second characteristic parameter of the cavity, namely the free spectral range, equation (2.7), will be determined. A theoretic calculation of the FSR assuming the specified cavity length of 100.1 mm results in a FSR of $\Delta\nu_{FSR} = 1.497\,\text{GHz}$.

To measure the FSR, sidebands are applied with a Windfreak[4] microwave source connected to a fiber EOM[5]. The sidebands are applied a definite frequency at either side of the carrier peak and have much smaller amplitude than the carrier frequency. The sidepeaks are used as a frequency reference to translate from time, as given by the oscilloscope, to frequency using the equation

$$\Delta\nu_{FSR} = \Delta f_{sideband}\frac{\Delta t_{carrier}}{\Delta t_{sideband}}. \tag{2.28}$$

To obtain a $\Delta t_{carrier}$ the laser is scanned over more than a free spectral range. Such a scan is shown in figure 2.12 with the blue being the data from the photodiode on the transmission, the orange crosses the carrier peaks and the green crosses the sidepeaks. From this data the FSR of the cavity is determined to be $\Delta\nu_{FSR} = 1.497\,\text{GHz} \pm 0.030\,\text{GHz}$ with the error being from the method used to determine the peaks [49]. This agrees very well with the theoretical prediction.

As opposed to the finesse it is not necessary to determine the FSR for the other wavelengths as it depends solely on the geometrical properties of the cavity and is such not wavelength dependent.

[4]SynthUSBII
[5]EOspace - Lithium Niobate Modulator - PM-0S5-20-PFA-PFA-960

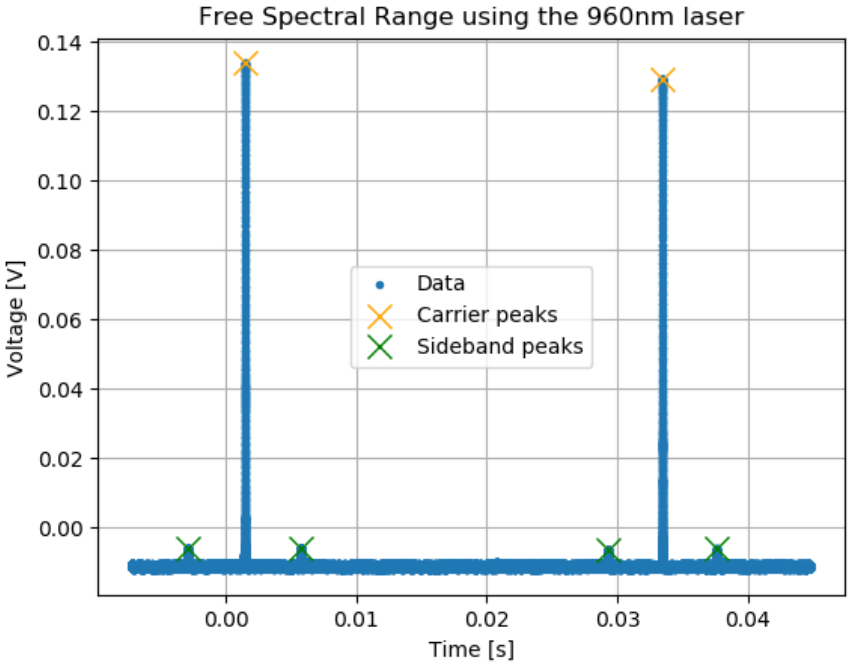

Figure 2.12: *Scan over more than a FSR. Orange crosses are the carrier peaks, green crosses are the sidepeaks applied by the windfreak. The blue is the data. The FSR determined using equation* (2.28) *is* $\Delta\nu_{FSR} = 1.497\,\text{GHz} \pm 0.030\,\text{GHz}$.

Hysteresis

It is also of interest to study the scan behavior of the laser. The scan is not necessarily linear and identical for back and forward scanning, a phenomenon known as hysteresis. Hysteresis can be caused by the scanning of the piezo crystal not being perfectly linear.

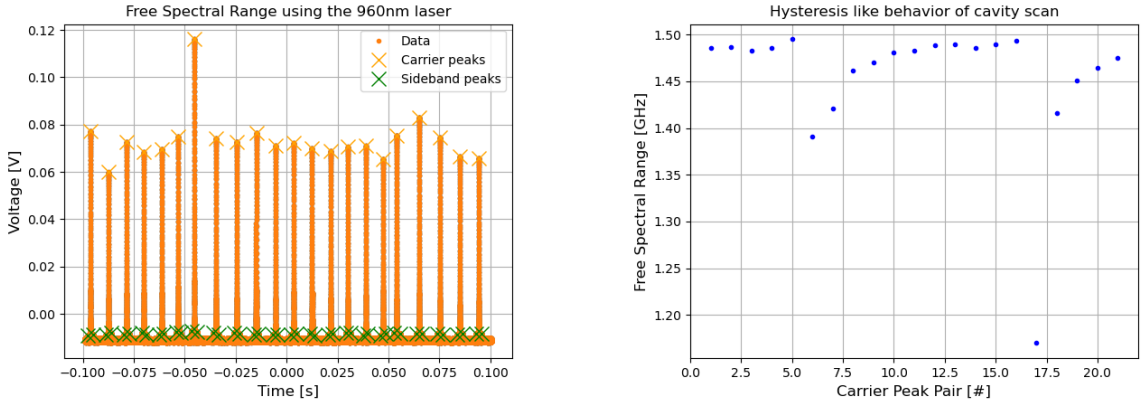

(a) **(b)**

Figure 2.13: *Hysteresis behavior of the piezo.* ***a)*** *Scan over 11 carries peak resonances and corresponding sidepeaks.* ***b)*** *FSR calculated for each carrier peak using equation* (2.28)

Here we investigate possible hysteresis using the same approach as for the FSR measurements. In figure 2.13a a scan of the laser (back and forth) over 11 carrier peaks is shown and in 2.13b the corresponding FSR calculation is seen. Carrier peak pairs 6 and 17 are where the scan turns. Therefore, the distance in time between those two is not correct as it is in fact the same peak twice. However, Peak 7 through 12 and peak 18 through 22 clearly shows the hysteresis behavior of the scan as the FSR over these peaks are not constant. For a hysteresis-free scan, the FSR would have been a flat line with outliers at the turning points of the scan. However, it very clearly has a slope.

This is important to keep in mind if the laser is ever used in scanning mode for collecting data. By not having a linear frequency scan the translation from time to frequency becomes a non-linear action and the data will have to be adjusted accordingly. This is for example important when scanning across the rubidium spectrum as done for the vapor cell EIT in chapter 4. In such a situation knowing two points and using equation (2.28) will not be sufficient as it will result in a wrong frequency axis as the non-linear behavior is not accounted for.

2.4.3 Mode separation

In this section, the mode separation derived in section 2.4.3, equation (2.19) and (2.21), is experimentally investigated. The measurement is performed by intentionally misaligning the 1012 nm laser into the cavity such that a higher order mode is visible. The laser is then scanned across more than one FSR to obtain a signal of two cavity peaks during a single scan. This provides a precisely known time to frequency relation, via the FSR, that makes it possible to determine the frequency difference of the fundamental and first higher order mode. The data is shown in figure 2.14, with the red crosses being the fundamental modes and the green those of the higher order mode.

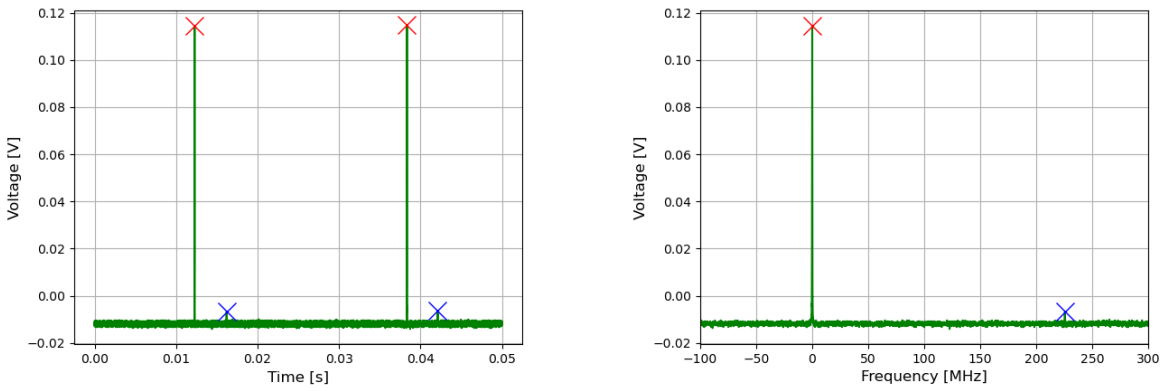

(a) *Full scope trace* **(b)** *Zoom on a single cavity resonance*

Figure 2.14: *Separation of modes due to the acquired Gouy phase. Red crosses are the carrier peak, green crosses are the first higher order mode and the blue is the trace data.* ***a)*** *shows the full scan over two cavity resonances with a time-axis.* ***b)*** *shows a zoom on a single cavity resonance with a frequency axis.*

Using this data the mode separation is determined to be $\Delta\nu_{HigherOrder} = 221\,\text{MHz} \pm 30\,\text{MHz}$. The error stems from the peak detection method and is obtained via the covariance matrix. This is in very good agreement with the theoretical calculation.

The measurements here were done with the 1012 nm laser as opposed to the 960 nm laser used for the other cavity characterization measurements. However, since both the Gouy phase and the frequency separation presented here, do not depend on the wavelength of the light, this holds for all wavelengths coupled to the cavity.

2.5 Locking the laser

For the Toptica TA-SHG laser locked in this work, several controllers are provided by the manufacturer. In this section, the two key modules for laser locking are presented followed by the lock optimization carried out for the 960 nm TA-SHG laser.

PDH Module

The PDH module is a commercial device from Toptica. It creates the PDH error signal via frequency modulation. The modulation frequency can be either 5 MHz or 25 MHz. The module has two channels of which we only used one. The module has one input and two outputs. The first output is a frequency reference signal. The input takes a frequency signal. This frequency signal is compared to the reference frequency obtainable from the first output port. The second output is the PDH error signal generated within the module. This depends on the phase difference of the input signal and the frequency reference. The phase difference can be adjusted using the laser controller. It was adjusted to give as symmetric a PDH signal as possible on the second output port. The frequency reference signal is what is used to apply sidebands to the laser light, i.e. the features at ± 25 MHz in figure 2.4.

FALC 110 Module

The FALC 110 module is a commercial PID controller from Toptica. It takes an error signal from the PDH module as input and produces an output signal which we feed back into the laser. An ordinary PID regulator has three terms, a Proportional, an Integral, and a Differential term, hence the name. The FALC 110 is slightly more advanced as it has four integrator terms, of which we use three, and a differential term. These are a Slow Limited Integrator SLI, Fast Limited Integrator FLI, Unlimited Integrator ULI, Extra Slow Limited Integrator ESLI (unused), and a Fast Limited Differentiator FLD. Each of these terms takes care of a component in the drift. The slow integrators deal with the long term drift due to ambient changes, such as temperature, etc. and the FLI and FDI are the fast oscillating noise terms.
The module also offers the option to amplify the error signal by adjusting the 'main gain'.

Optimizing the Laser Lock

The final locking of the laser is done by adjusting the parameters for the PID controller on the FALC module to optimize the long term stability of the lock. For a stable cavity, it is possible to detect a difference in the linewidth of the laser lock by changing a parameter just a single step. Such a measurement can be done by measuring the intensity stability

over time or via beat note with another stabilized laser. This was realized in the scope of a previous master thesis of the group on a similar system for different wavelengths [43]. Very narrow laser locks as in the cited master thesis were not achieved in this work.

If one of the PID terms is set too low, it will respond slowly to a laser drift, and such allow for a large degree of fluctuations. If, on the other hand, a term is set too high the response may be too aggressive. A too aggressive lock pushes the laser too far with each correction and the laser can be knocked out of lock even due to small fluctuations. A variety of PID settings were attempted for locking the 960 nm laser, with SLI=7, FLI=8, and FLD=4 being too aggressive. SLI=6, FLI=8, and FLD=1 proved to be a lock reliable enough to make a finesse measurement of the cavity mirrors, but small perturbations like placing a hand on the table were enough to unlock it.

A lot of work was put into optimizing this lock. For the parameters SLI=6, FLI=8, and FLD=1 the best lock was obtained. To examine how well the laser was locked a beat note with the TA-SHG laser from the running Rydberg quantum optics experiment was made. Monitoring the linewidth of this beat note would result in an upper bound on the linewidth of either laser. As the experiment laser has proven to work flawlessly with a narrow linewidth the beat note would tell a lot about the new TA-SHG laser lock as it would be the dominating factor to the linewidth of the beat note.

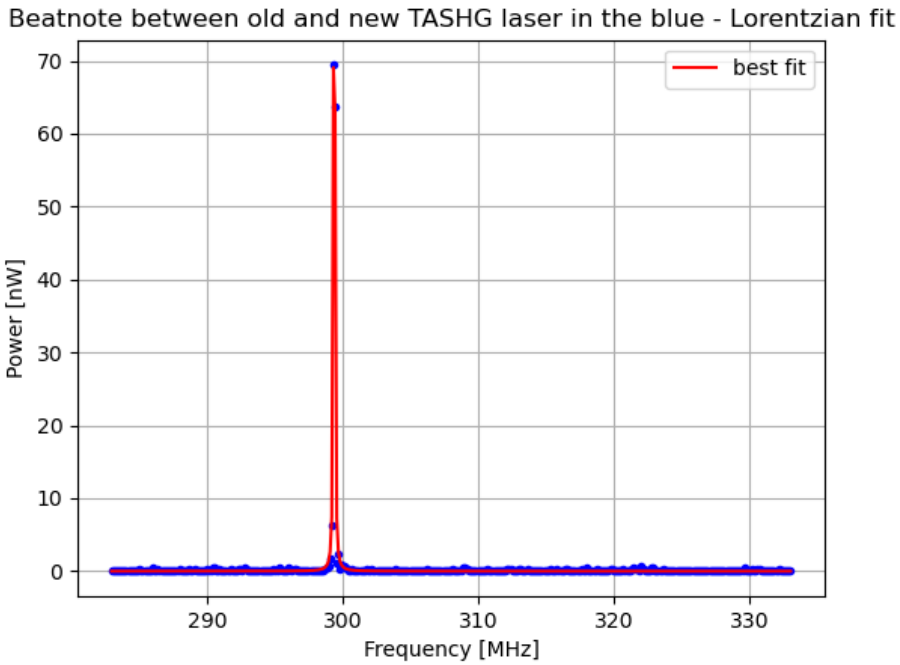

Figure 2.15: *Beat note with new and old TA-SHG laser in the blue. The red is the fitted curve.*

The beat note shown in figure 2.15 was made in the blue and while undersampling. A clear beat note frequency is seen around 300 MHz. When increasing the sampling time to get a better resolution on the beat note it turned out to be widening on a MHz scale. When further investigating the beat note behavior a drift in the beat note frequency was observed. The beat note frequency was observed to drift on a MHz scale on a minute-time-scale and to jump some 10 MHz when the door of the lab was opened.

The cavity was placed in a non-shielded environment at the edge of an optical table, close to our lab work area, where it was subject to a strong airflow from the laboratory air condition unit. As we had not been able to pump the cavity housing under vacuum, it is not surprising that vibrations and environmental change of the cavity surroundings will affect the air within the cavity housing.

After discovering that the cavity itself was not stable any further work on locking lasers was postponed until a turbopump was available for investigating the leakage. This thesis was handed in before such a pump was available.

2.6 Conclusion and Further Work

The work presented in this chapter has shown that three lasers can be properly mode matched to the cavity with the setup in figure 2.8. This shows that lenses and positions have been chosen correctly. The two wavelength-independent cavity characterization parameters, the FSR and mode separation have been determined and show good agreement with theory as a FSR of 1.497 GHz and a mode separation of 221 MHz were measured. The finesse of the cavity at a wavelength of 960 nm was also determined. This was measured to roughly 20000 using the decay of the cavity transmission signal and is within the specifications of 5000 to 20000. The finesse of the cavity should be measured for the two other wavelengths as well. However, the measurement technique of knocking the laser out of lock requires the laser to be locked in the first place. Therefore, such measurements have only been performed with the 960 nm laser.

It has also been examined what PID settings would give a good lock for the 960 nm laser. It turned out that the cavity being under air and not vacuum, combined with its placement in the room, made it impossible to create a good lock. It was possible to find a set of parameters for which the laser would remain locked but the cavity itself was not stable enough. This lead to several MHz fluctuations in the locking frequency making the laser frequency varying more in locked mode than free-running.

Due to the cavity not being under vacuum, and large frequency fluctuations on the MHz scale being observed, it was not meaningful to lock all three lasers to the cavity. Therefore, some work remains to be done when a turbopump is available and allows investigation of possible cavity housing leaks.

Chapter 3

Phase Interferometer

This chapter describes, the design, construction, and programming of a phase interferometer for measuring the phase shift of a photon following the interaction with an ensemble of ultracold rubidium atoms excited to a Rydberg state. To measure this change we need to measure the phase before and after the photons interact with the atomic ensemble. This is a challenge as the atoms absorb light. To overcome this we create a beat note with a resonant beam and a beam detuned far enough to pass virtually unnoticed through the ensemble. By monitoring the beat note before and after the atomic ensemble we can deduce the phase shift imprinted on the photons.

We wish to solve this challenge for a cloud of ^{87}Rb atoms using the $5S_{1/2}, F = 2 \rightarrow 5P_{3/2}, F = 3$ probe transition. This transition has a linewidth of $\Gamma/2\pi = 6.1\,\mathrm{MHz}$ [17] which means the frequency shift just needs to be of order some ten of MHz to put the light so far off resonance no absorption occur. We choose to solve this by constructing an interferometer in frequency space. The design of this interferometer is based on work done at MIT [17, 50] and at the Max-Planck Institute für Quantenoptik [18]. A sketch of such an interferometer is seen in figure 3.1. We utilize an Acousto Optical Modulator (AOM) to spatially separate the probe laser while applying an 80 MHz shift to the first diffracted order. The two diffracted orders are superimposed using a beamsplitter. This creates a beat note which is continuously detected on a photodiode. The other output of the beamsplitter is attenuated to a single photon level and sent to the atomic ensemble. In this ensemble, one of the beams interacts with the atoms while the other passes through unnoticed. This results in a shift of the beat note frequency with respect to the reference signal from the photodiode.

I will now discuss the phase interferometer in further detail. First, a discussion of the stability of such a setup is discussed. This is followed by a discussion of how to use the reference signal as a trigger such that multiple phase measurements can be combined to obtain sufficient amounts of data. The triggering scheme is tested in section 3.2. All the testing is done using a setup build on the side. Finally, the interferometer is implemented in the running Rydberg quantum optics experiment in chapter 3.3 and phase measurements of photons interacting with atoms are presented.

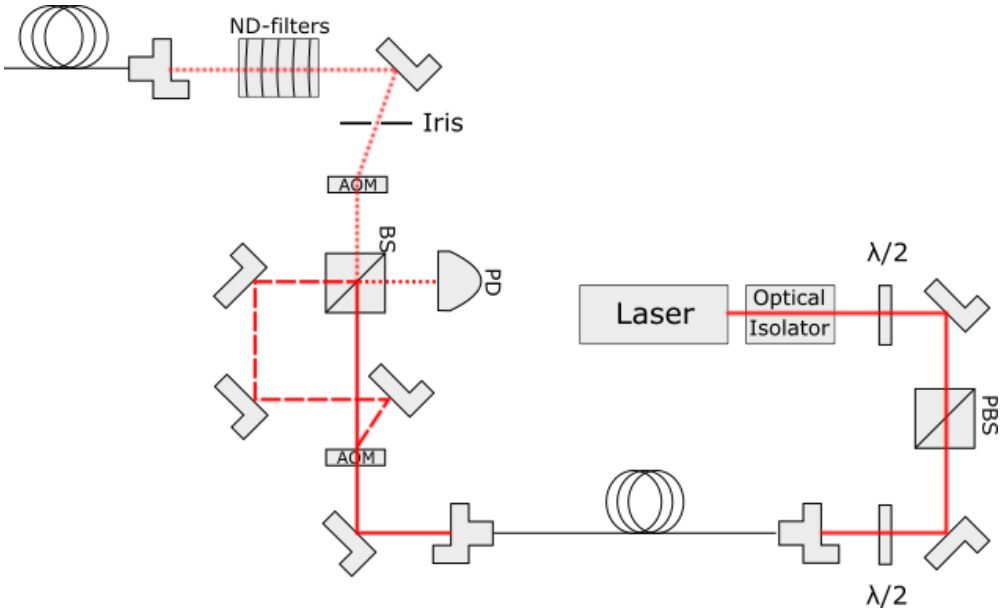

Figure 3.1: *Illustration of the phase interferometer. Solid line is the* 780 nm *light. Dashed is the* 80 MHz *shifted beam. Dotted are the overlapped beams. Laser light is emitted from the laser and send through a polarization-maintaining fiber. The first AOM shifts the first order by* 80 MHz*. The zeroth-order and the first order are overlapped at a 50:50 beamsplitter which results in a beat note. That beat note is detected on a photodiode via one arm of the beamsplitter, while the other arm is sent through a second AOM used to switch the light on and off and through a series of Neutral Density (ND) filters with a total value of ND=13 which attenuates the light to the single photon level*

3.1 Simple Phase Interferometer

In this section, a further discussion of the phase interferometer is presented along with the results of a stability test. While the fundamental part of the interferometer, sketched in figure 3.1, was discussed previously, a few additional elements remain to be discussed. First, it is important to have a stable polarization throughout the setup. If a stable polarization is not achieved the arms might have different polarization, resulting in reduced contrast in the interference of the beat note. In this setup polarization stability is ensured by coupling the light into a polarization-maintaining fiber. Secondly, an additional AOM is placed in the path of the beat note heading to the experiment. This AOM is used to pulse the light. In the Rydberg quantum optics experiment, we do not always want the probe light to be on and this setup provides a fast on-off switch.
Having passed through the second AOM the light is attenuated with ND-filters and coupled into a fiber sent to the Rydberg quantum optics experiment.

A great advantage of this setup is the short distance over which the two beams are not superimposed. When the two beams are superimposed their beam paths experience the same fluctuations from temperature, optics, and vibrations in fibers. Since we are interested in measuring the relative change in beat note frequency before and after the atomic ensemble the only noticeable fluctuation happens from the first AOM and to the beamsplitter. Therefore, when setting up the experiment it is important to have the shortest possible pathlength from the AOM splitting the light into 0th and 1st order and to the beamsplitter at which they are recombined.

3.1.1 Stability Tests

To measure the stability of the interferometer we wish to monitor the relative phase of the beat note at the reference and after the fiber leading to the experiment. This was done using photodiodes for both measurements as going to the single-photon regime would provide no additional insight into the stability. The fiber after the beams have been overlapped was chosen to be of length similar that used when it is in the running experiment.

To determine the drift over time of this setup and examine if there is any relation to the change in room temperature, a series of measurements of the phase difference between the two classical detectors were performed over the duration of several hours. An oscilloscope[1] was programmed [51] to capture the waveform of the two sinusoidal beat note signals (one from each detector) at a time interval of 10 s. For each set of waveforms, two sine waves were fitted, and from these fits, the phase difference of the two was extracted. A temperature sensor was placed above the table continuously measuring the temperature in the lab. These data were extracted and plotted on top of the phase change. The resulting plot is shown in figure 3.2.

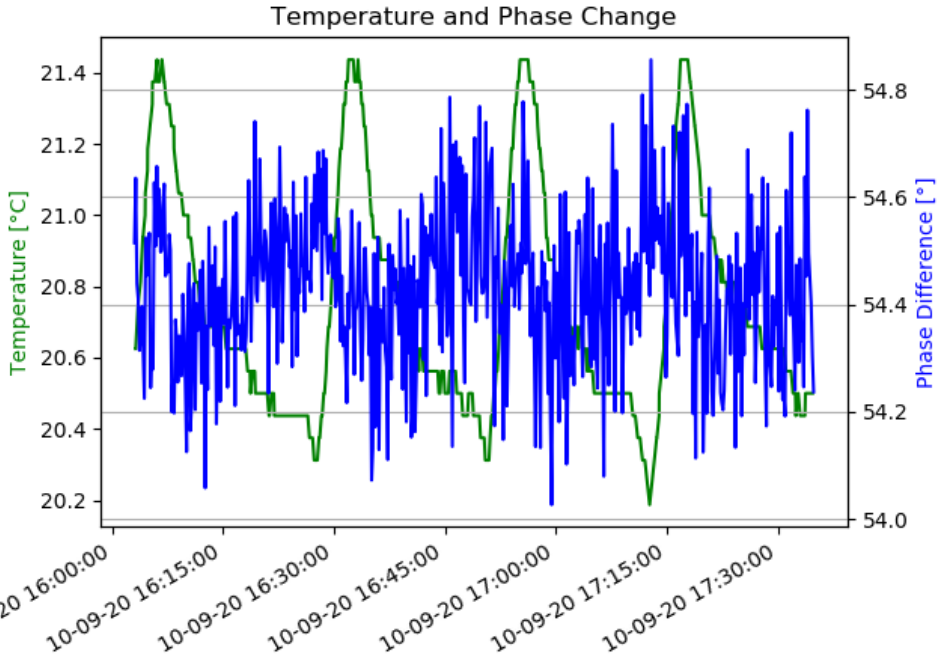

Figure 3.2: *The green curve is the temperature above the table in the lab. The blue curve is the phase change. There is a clear correlation between temperature and phase change. The deviation in phase over one and a half-hour of less than* 1°

In figure 3.2 the green curve is the lab temperature which oscillates over approximately 1 °C with a period of approximately 15 min. The blue curve is the relative phase of the beat note signals measured on the photodiodes. The blue graph shows sub 1° phase change throughout one and a half hours. The correlation between the phase measurements and room temperature indicates that thermal fluctuations are the major source

[1] Keysight Technologies InfiniiVision 2000 X

of phase instability. The mirrors can change shape ever so slightly due to temperature fluctuations but this will happen on a much slower timescale than what is examined, and can, therefore, be ruled out as a possible contribution to the instability. This leaves the small change to the index of refraction of air to be a likely contributor to the phase change. A phase change of 2π would be equal to a pathlength change of one wavelength, i.e. 780 nm, which means a 1° phase change is equal to 2.2 nm path length change. The total pathlength of the non-overlapping beams is roughly 10 cm compared to which 2.2 nm is a vanishingly small distance. This stability curve sets the absolute limit of resolution in this system. During scans, the reference point is always moved to a common point using the reference beat note signal from the photodiode, and data is collected during a time window on the order of 10 ms such that temperature drift can be neglected.

3.1.2 Triggering

In the Rydberg quantum optics experiment, we will be working in the single photon-regime. This means that instead of measuring a continuous beat note signal we will measure single photon detection events. By adding up a lot of repetitions of the experiment it is possible to obtain the sinusoidal pattern of the beat note signal after the light has passed through the atoms. To add the individual measurements correctly, each detection event has to be triggered correctly with respect to the phase of the reference signal. The triggering is done using a home-build comparator box designed to take a TTL and the reference beat note signal as input and return a TTL output. The comparator functionality is sketched in 3.3.

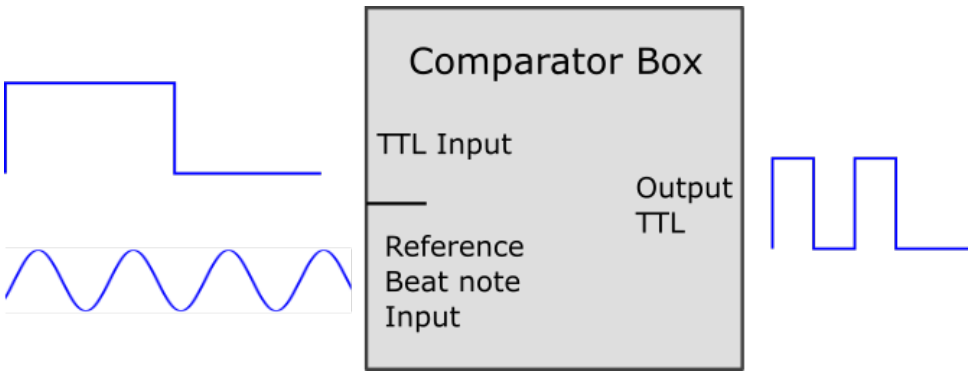

Figure 3.3: *Illustration of the functionality of the home build comparator box. A TTL input and an input for the beat note signal from the photodiode. The output is based on an AND gate returning high when both inputs are above a threshold value.*

The TTL input is provided from a pulse generator. The output TTL signal is "high" when both of the input signals are above a threshold voltage. This voltage can be adjusted using a potentiometer.

The output TTL can be used to trigger the data collection by triggering on a rising or falling edge. The reference beat note signal is always on and the input TTL therefore also serves as an overall trigger for the phase interferometer. The full electronics set up for such a triggering scheme is sketched in figure 3.4

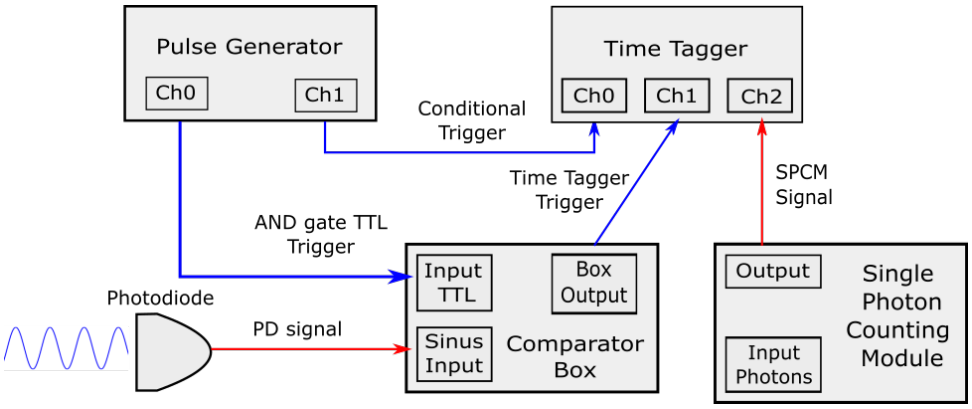

Figure 3.4: *Illustration of the electronics required for implementing the triggering scheme for the simple interferometer. The pulse generator sends a TTL signal to the comparator box and the photodiode sends the reference beat note signal. The output is going to the Time Tagger and triggers counting on the signal from the SPCM.*

The setup utilizes a Time Tagger to record the detection events. With the current setup, the Time Tagger receives a new trigger with every oscillation on of the output from the comparator box which is a 80 MHz TTL signal. The Time Tagger has a maximum number of 8×10^6 counts per second. Applying a signal of higher frequency results in overflow errors. To avoid this the functionality of a conditional filter is used. This filter makes it such that a channel only counts the first click after a click on some other channel. This is supplied from the pulse generator and prevents overflow errors.

Before implementing the setup and the triggering electronics into the running experiment, we are interested in performing some tests on the triggering procedure as well as showing that the phase change of single photons can be detected using this setup.

As we do not have an atomic medium similar to that used in the experiment available for a test setup we choose to use an Electro-Optical Modulator (EOM) in its place. An EOM is fundamentally different from an atomic ensemble. It is a block of glass that changes refractive index with an applied electric field and hence interacts with any wavelength and the trick of a non-interacting part of the beat note because of the detuning, is not applicable for such a test. The EOM will be further discussed in the coming section. As a result of using the EOM, the setup had to be expanded significantly.

3.2 Double Interferometer

In this section, the expansion of the system presented in section 3.1 required to test the triggering setup using an EOM is presented.

As we do not have an atomic medium similar to that used in the experiment available for a test setup we choose to use an Electro-Optical Modulator (EOM) in its place. An EOM is fundamentally different from an atomic ensemble. It is a block of glass that changes refractive index with an applied electric field and hence interacts with any wavelength and the trick of a non-interacting part of the beat note because of the detuning, is not applicable for such a test. The EOM will be further discussed in the coming section. As a result of using the EOM, the setup had to be expanded significantly.

Since the EOM shifts the phase of all light passing through we now need an interferometer similar to the one previously discussed to have a reference, and we need a second

one, in which an EOM is inserted in one of the beam paths before they are overlapped making this beat note. Such a design is shown in figure 3.5. This design will allow the EOM to shift the phase of one of the beams relative to the other, effectively shifting the beat note phase relative to the reference. The extension of the setup is done by inserting a 50:50 beamsplitter in the beam paths after the initial AOM.

Before we dive further into testing the triggering process and using the EOM, the same stability tests as for the simple setup are performed. This is to examine what magnitude of drift is expected for a setup in which the non-overlapping beam path is about a factor of 10 longer.

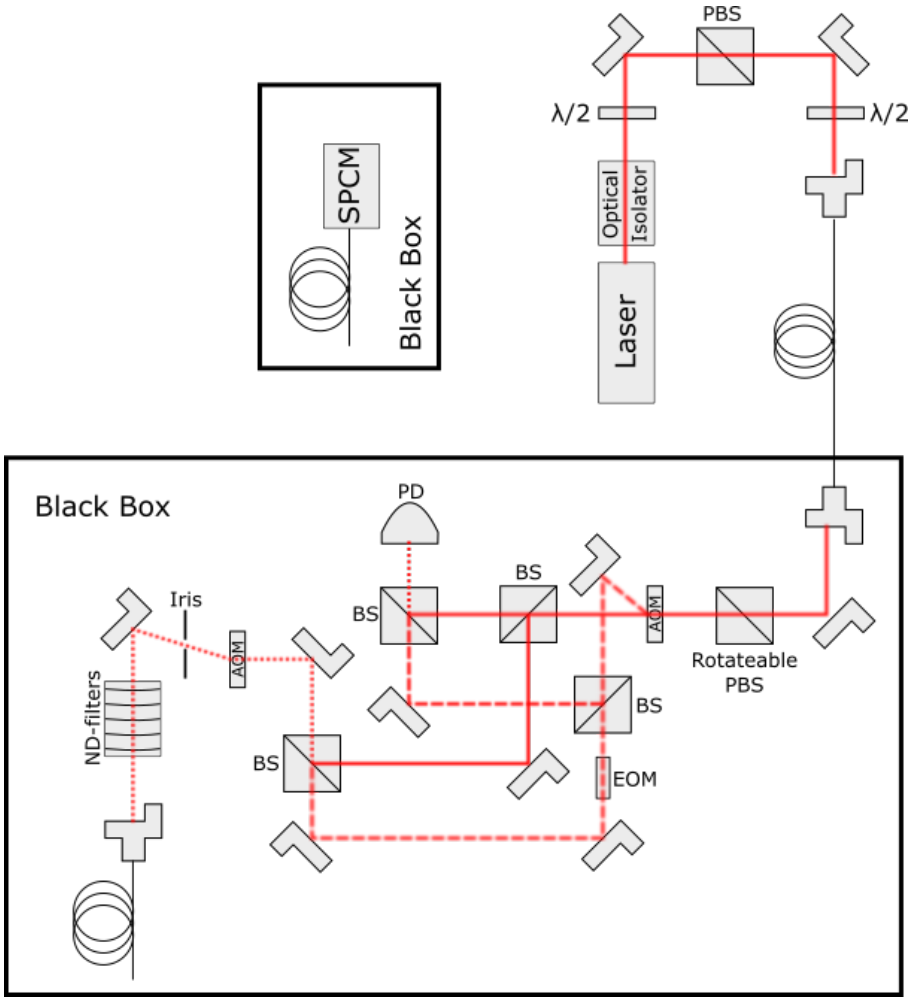

Figure 3.5: *Illustration of the double interferometer. The solid line is the non-shifted light, dashed is the shifted, and dotted is the overlapped. The laser is coupled out and initially send through a PBS to make possible polarization fluctuations into intensity fluctuations. Afterward, the AOM splits the light into a frequency shifted and non-frequency-shifted order. A 50:50 BS in each arm is used to split both beams. One is sent to a photodiode creating the classical reference from the first interferometer. The second interferometer has an EOM in one arm and the shifted beat note is sent to an SPCM. The second interferometer light is attenuated with ND filters to ensure single photons at the SPCM. Both the interferometer and the SPCM are placed in separate black boxes for isolation from the environment and stray light.*

3.2.1 Classical Measurements

In this subsection, the classical detection approach is used. This means a setup similar to that of figure 3.5 is used but the ND filters are removed and the fiber does not connect to a Single Photon Counting Module, but to a photodiode. First, stability is examined. This is followed by measurements of a phase change induced by the EOM.

Stability tests

To perform classical measurements on the setup the SPCM was replaced with a photodiode and the ND filters removed.

The first measurement done with this setup was a stability check over a long timescale compared to an experimental cycle. This is to characterize the long-term stability. Since the pathlength over which the beams do not overlap is significantly higher for this setup the influence of temperature fluctuations is expected to increase as well. This can be seen in figure 3.6 with a drift of 126° in just one and a half hours.

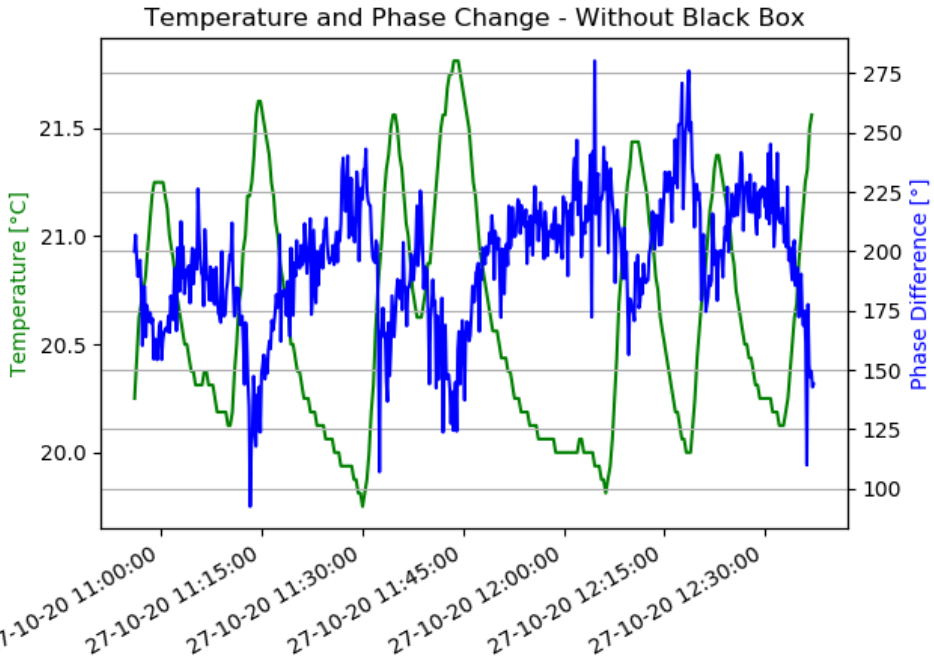

Figure 3.6: *Green graph is the room temperature above the experiment table and the blue is the phase change measured. This measurement was done without the black box for isolation.*

However, this could be significantly improved. By adding a box for isolation, and removing tension from cables connected to optical components, far better stability was obtained as shown in figure 3.7. This more stable setup has a drift of 13° throughout just over an hour. This increase in drift compared to the simple setup is expected due to the longer non-overlapping beam path.

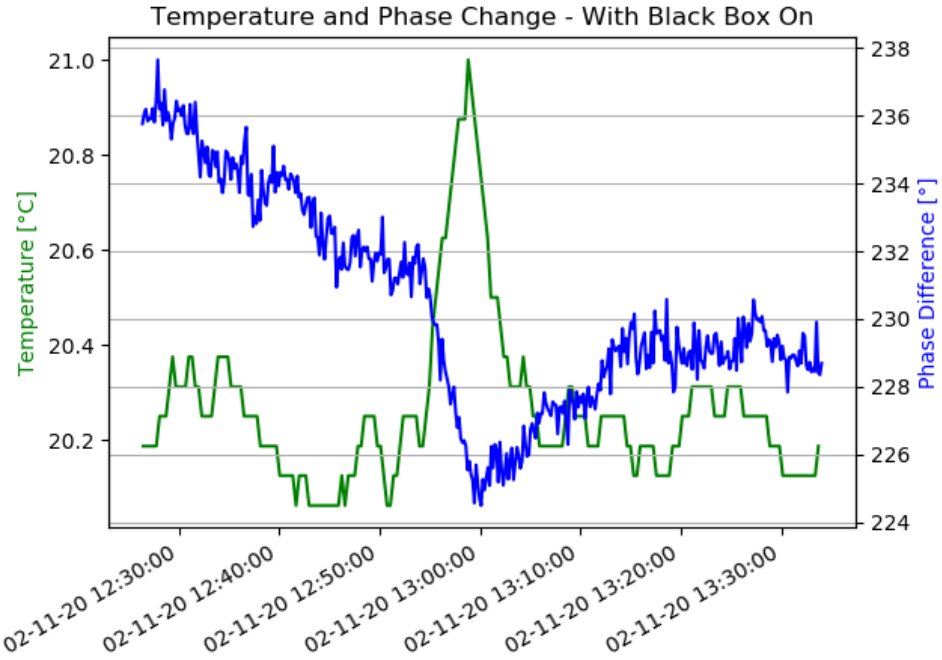

Figure 3.7: *Green graph is the room temperature above the experiment table and the blue is the phase change measured. This measurement was taken with the black box to isolate the interferometer from the environment.*

Phase Change Measurements

The EOM used for this work uses a LiNb crystal. Our EOM is home built and consists of the LiNb crystal mounted in between two copper plates. The electro-optical properties of a LiNb crystal stem from its change in refractive index with an externally applied electric field [52]. This behavior is only happening along one of the crystal axes and the EOM thus has to be oriented correctly with respect to the polarization of the light. The change of phase of interest is the relative change from the applied electric field. The expected relative change of phase, $\Delta\Phi$ can be calculated using the following two equations

$$\Delta\Phi = \frac{\pi}{\lambda_0} n_e^3 r_{33} V_e \frac{L}{d}, \tag{3.1}$$

$$n_e^2 = 4.4569 + \frac{0.094779}{\lambda^2 - 0.034439} - 0.026721\lambda^2. \tag{3.2}$$

The numerical values are experimental parameters [52]. Here, λ is the wavelength of the light and n_e the wavelength-dependent refractive index. V_e is the applied electric field and d is the distance between the plates. L is the length of the LiNb and r_{33} is the Pockels factor.

Our EOM can take an input voltage of 0V to 500V with 500 V corresponding to a phase change of 2π. We use it only up to 250 V which corresponds to a phase change of π.

We seek to measure the phase change induced by the EOM as a function of the applied voltage. To do so, a few extra electronics components will need to be triggered on top of those sketched in figure 3.4. These include a high voltage switch which is used to switch the voltage applied to the EOM on and off. The high voltage applied to the EOM is set

using a high voltage power supply. For the initial measurements of this section, it is set by hand. Later it is implemented in the triggering scheme. The additional electronics is shown in figure 3.8.

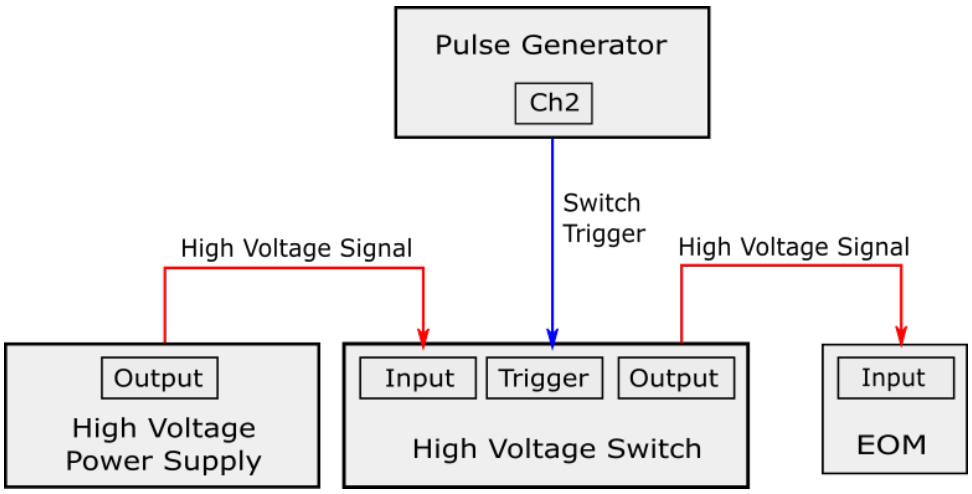

Figure 3.8: *Illustration of the electronics required for using the EOM to induce a phase shift. This is in addition to that presented in figure 3.4. A high voltage power supply connect to a high voltage switch. The switch receives a trigger in the form of a TTL signal from the pulse generator. The output is connected to the EOM.*

The measurements of the phase change induced by the EOM were done by performing 10 measurements within short succession (a few seconds) at a given voltage applied to the EOM. An average of the relative phase of these 10 measurements makes up a single value in figure 3.9. The voltage applied to the EOM is changed manually resulting in roughly a minute between the measurement of each different voltage. We measure a phase shift of 0.7π at 250 V which is lower than the theoretically expected value of 1π. However, previous measurements with this EOM indicate an expected phase shift of this magnitude [53].

Measuring the data presented in figure 3.9 takes roughly ten minutes, though the actual data collection takes only a few seconds per data point. This is within a single period of the temperature oscillation in the room. This measurement was done with the box on, so a maximum drift of 13° is expected.

To highlight drift the drift over time, we also took data over longer intervals. Initially, data was collected for EOM voltages of 0V,50V,100V, etc., and an hour later for voltages of 25V,75V,...,225V. This was all done with the box off to force more fluctuations into the system.

Figure 3.10 shows that two data sets cannot be meaningfully combined if taken over long time scales.

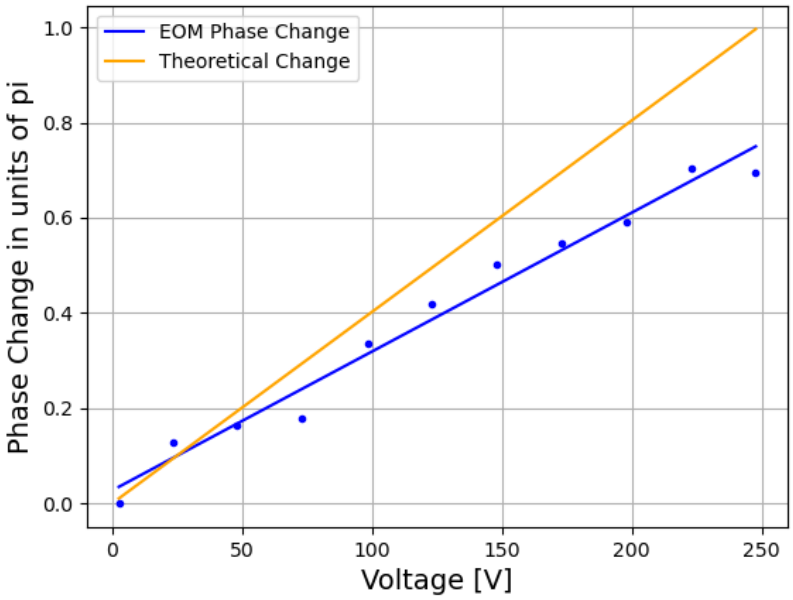

Figure 3.9: *The orange curve is the theoretical curve calculated from equation* (3.1) *and* (3.2)*. The following parameters are used in the calculation:* $\lambda = 780\,\text{nm}$*,* $d = 2\,\text{mm}$ *and* $L = 20\,\text{mm}$*. The blue points are the data points and the curve is the best linear fit. Each data point is made from the average of 10 measurements taken within a few seconds. Error bars are hidden by the size of the point-marker.*

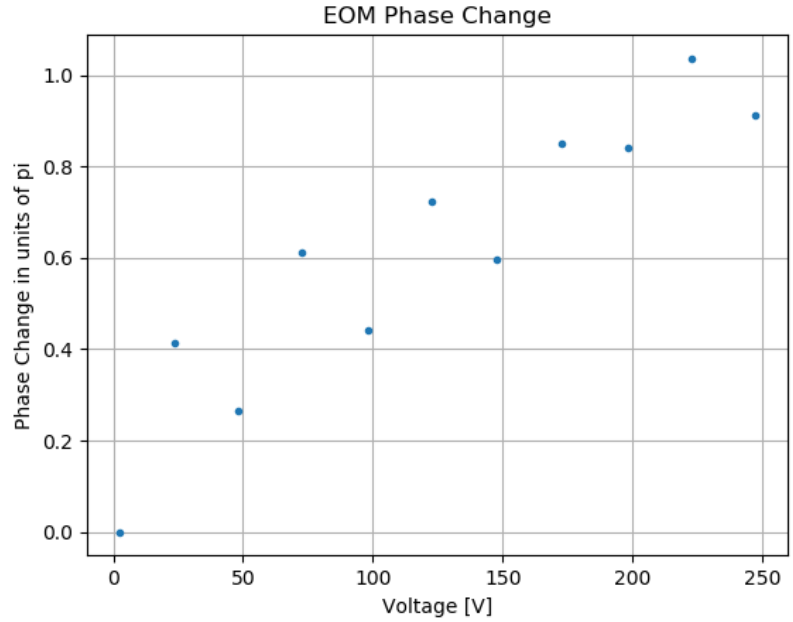

Figure 3.10: *The points* $i \cdot 50V$ *is taken at one time and the points* $i \cdot 50V + 25V$ *is taken roughly an hour later to have the phase drift out of sync.* $i \in \{0 : 5\}$*. Errorbars hidden by marker size.*

3.2.2 Quantum Measurements

Having characterized the stability of the double interferometer we now test the ability to detect phase shifts on the single-photon level. For all measurements presented in this section, the ND filters were flipped in and the SPCM connected. By using the triggering scheme developed in the previous sections we seek to reproduce figure 3.9 using quantum measurements. From such measurements, the parameters of the detection such as the time resolution set by the Time Tagger and the photons detected per time bin will be discussed.

For quantum measurements we use a SPCM to count the photon clicks, a Time Tagger to process the information, and a pulse generator to trigger the time tagger via the comparator box. The setup is later implemented in the running quantum optics experiment, and the sequence programmed for the testing closely resembles the one used for the running experiment. The structure is shown schematically in figure 3.11.

We term a single sequence as shown in figure 3.11 a **cycle**. Such a cycle includes a number of **shots** with the EOM on followed by the EOM off. The total number of cycles is referred to as a **scan**. For the programmed sequence, the EOM is on for 10 ms. Within this time, 1000 shots are applied to the comparator box TTL input. This gives a pulse sequence similar to that of the running Rydberg experiment. Within such a single shot the beat note oscillates many times. We trigger on the shot and captures single-photon data of the beat note.

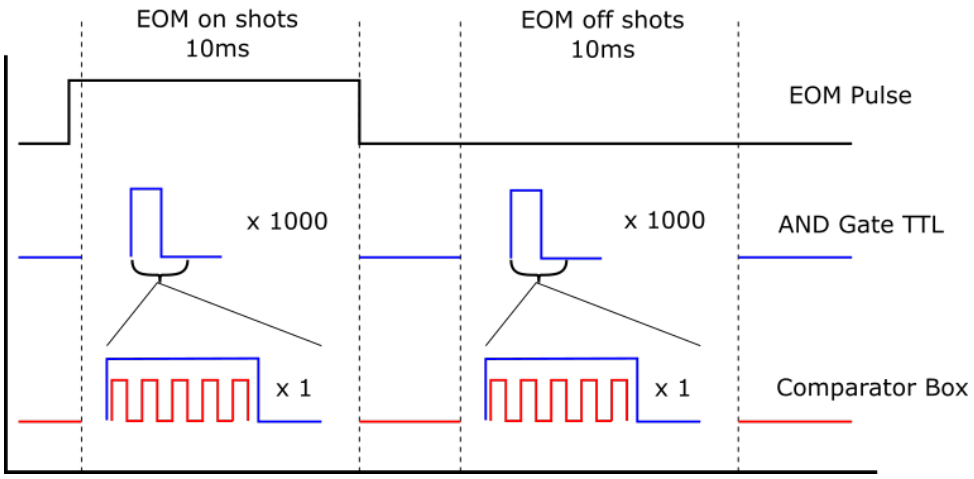

Figure 3.11: *Pulse structure of the experiment. The EOM is either on or off and within the 10ms on/off time there are 1000 pulses on the AND gate TTL. Within such a single AND gate TTL pulse there are several oscillations of the* 80 MHz *signal which is what we are interested in measuring. The pulses with EOM on correspond to atoms in the cloud and those with EOM off to the reference signal with no atoms.*

Figure 3.12a shows perfectly aligned trigger pulses due to the conditional filter. Figure 3.12b shows the photon clicks on the counting channel as yellow dots.

After initial tests of the electronics and triggering the data plotted in figure 3.13 was obtained. This figure shows the single-photon data in histogram form for 40 cycles each consisting of 1000 shots. The binwidth used for this data is 1 ns. A sine is fitted to the data and from the fits the contrast and phase shift are determined. The contrast is extracted from the fit rather than the data to prevent the influence of outliers.

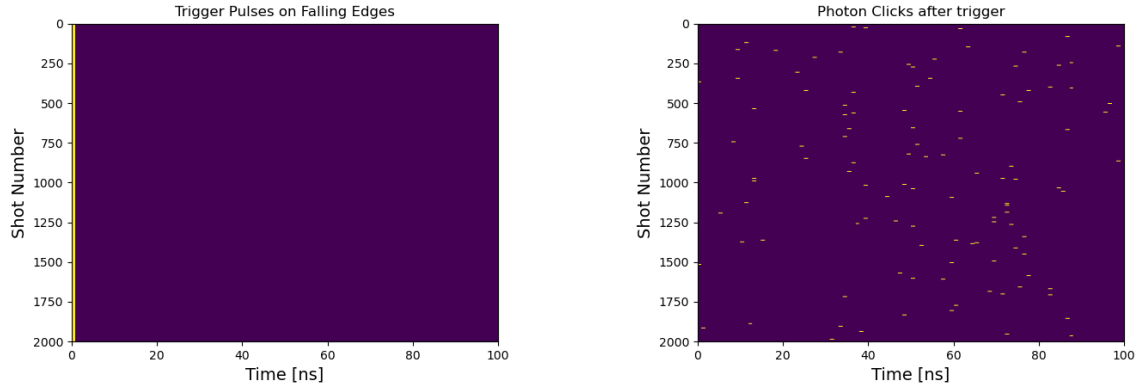

(a) *Trigger pulses each aligned with each other at the start at $t = 0$*

(b) *Photon clicks after a trigger has been received.*

Figure 3.12: *Shows the trigger pulses being perfectly aligned on the falling edge resulting in phase measurements always in phase with the latest classical clock signal reference. The photon clicks are represented by yellow dots in the right hand figure. Each shot contains on average 1 to 2 photons*

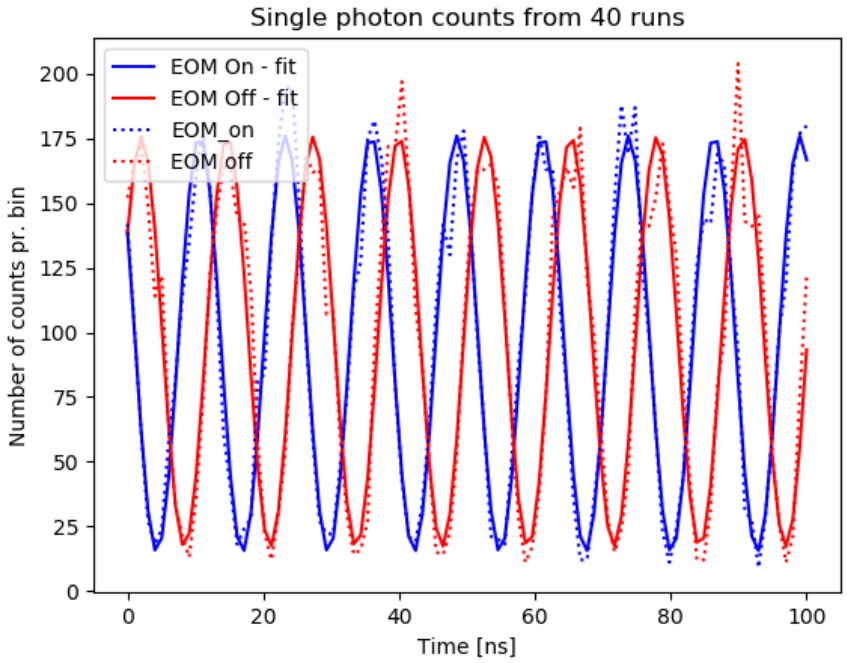

Figure 3.13: *A total of 40 cycles each with 1000 scans with a binwidth of* 1*ns. The red curve is with the EOM off and the blue with it on. The contrast is 85% based on the fit to the signals*

At this low number of cycles the probability of outliers like that at 90 ns is high and this yields a wrong result on the overall contrast when looking at the full eight periods. The voltage applied to the EOM was constant at 250 V leading to an expected phase change of roughly 0.7π according to figure 3.9. For the above data we also achieve a 0.7π phase change. This shows the system is able to detect the phase of single photons.

EOM Phase Change

The phase change induced by the EOM was determined classically as shown in figure 3.9. Presented below is a similar measurement performed at the single photon level. The measurement in the single photon regime was repeated several times using different light intensities. The intensity is measured as the average number of counts received on the Time Tagger. The count rate is adjusted via the number of ND-filters in front of the fiber to the SPCM. Each data point in the figures showing the phase change induced by the EOM as a function of the applied voltage consists of several cycles added together.

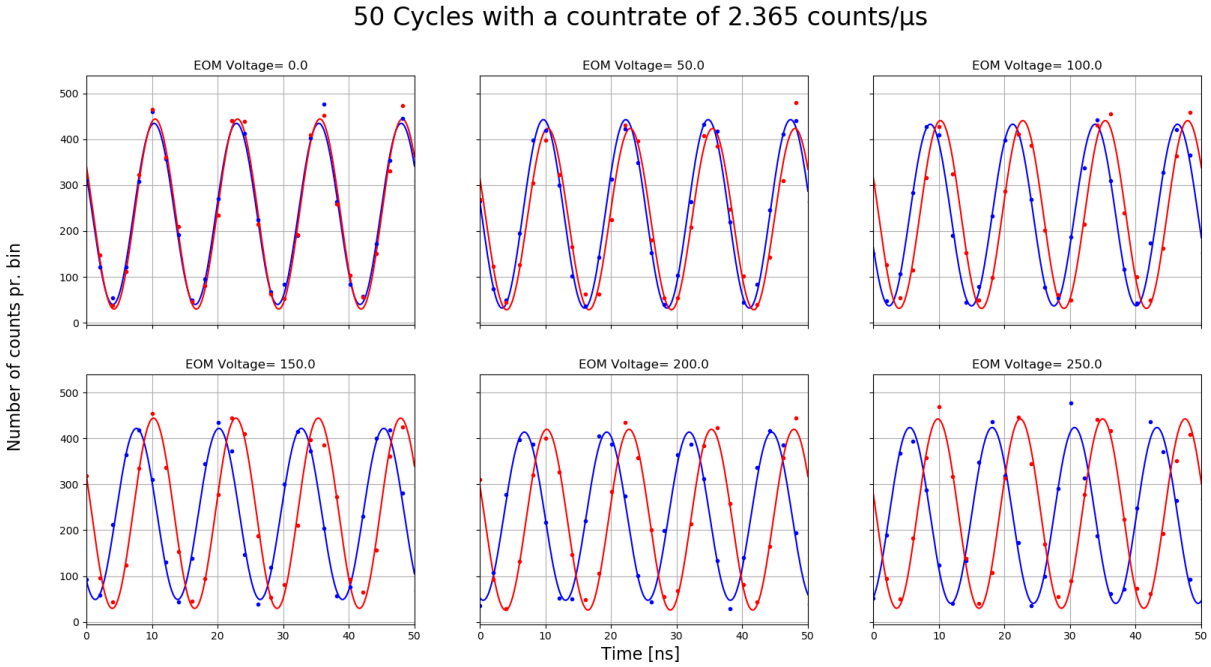

Figure 3.14: *Beat note signals detected for six different EOM voltages with 50 cycles added, running at a count rate of 2.365 photons per µs. Data is taken for 400ns and fitted on the full dataset. Only the first 50ns is plotted for clarity.*

Figures 3.14 and 3.15 show the results of 50 cycles for different voltages applied to the EOM and the corresponding induced phase change as a function of voltage. The count rate for this dataset is 2.365 counts/μs which results in plenty of photons after 50 cycles. The maximum count is roughly 450 photons in a single bin. This gives a good contrast of 90% and low error on the phase change of $\pm 0.02\pi$ extracted from the fit parameters.

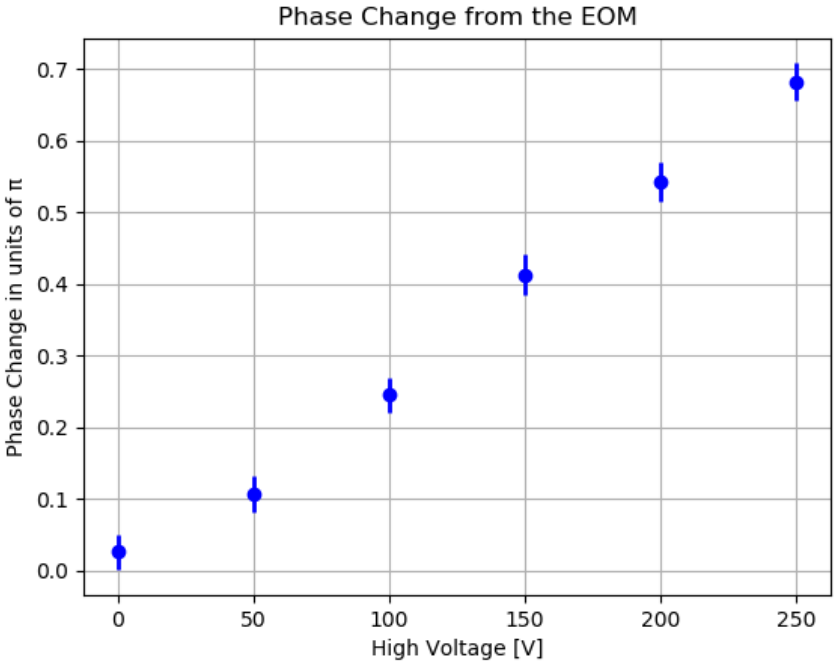

Figure 3.15: *Phase changed induced by the EOM as a function of the applied voltage with error bars being propagated standard deviation extracted from the covariance matrix. A total of 50 cycles are added with a count rate of* 2.365 photons/μs*. A total phase change of* 0.7π *was obtained in agreement with the classical graph in figure 3.9.*

Next, we investigate the effect of reduced intensity. Figures 3.16 and 3.17 are obtained when adding up 50 repetitions at a count rate of 0.129 counts/μs. The maximum number of counts in a bin is close to 20 which is too low and results in a larger uncertainty on the fit results. The sine-fit has a very clear deviation from the top of some of the bins because they end up acting as outliers. This large error on the fit leads to very large error bars on the corresponding phase change. An uncertainty on the phase parameter of $\pm 0.1\pi$ is found which is large compared to that of figure 3.15.

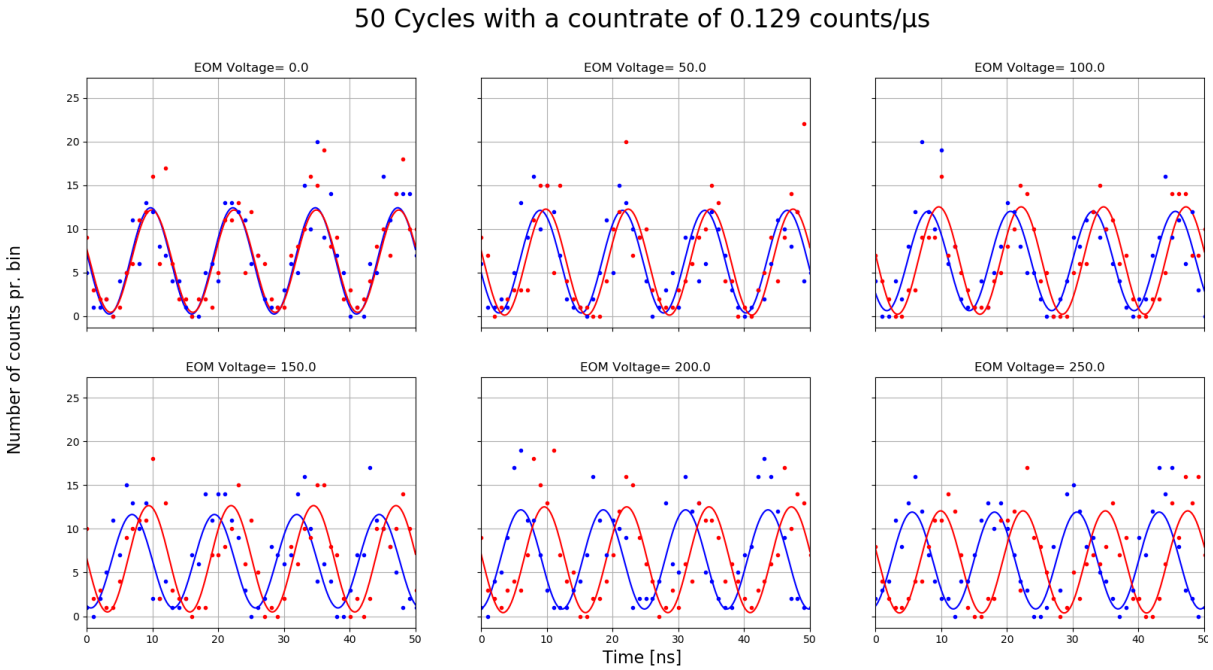

Figure 3.16: *Beat note signals detected for six different EOM voltages with 50 cycles added running at a count rate of 0.129 photons per µs. Data is taken for 400ns and fitted on the full set. Only the first 50ns is plotted for clarity.*

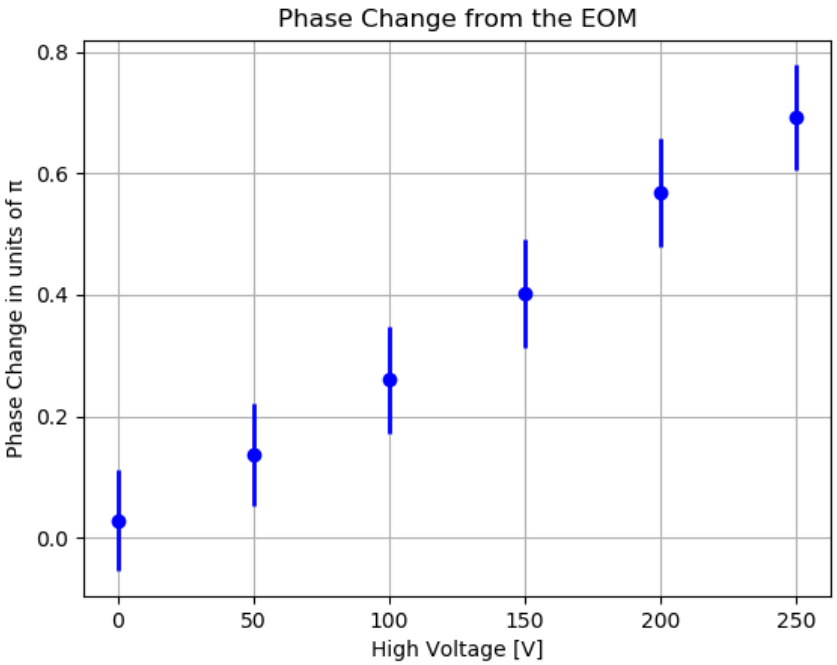

Figure 3.17: *Phase changed induced by the EOM as a function of the applied voltage with error bars being propagated standard deviation extracted from the covariance matrix. A total of 50 cycles are added with a count rate of* 0.129 photons/µs. *The standard deviation is on the order of* 0.1π.

By adding up more cycles with a photon rate of 0.129 counts/μs a better fit can be obtained. This is shown in figures 3.18 and 3.19. The uncertainty becomes approximately half when running the experiment three times longer.

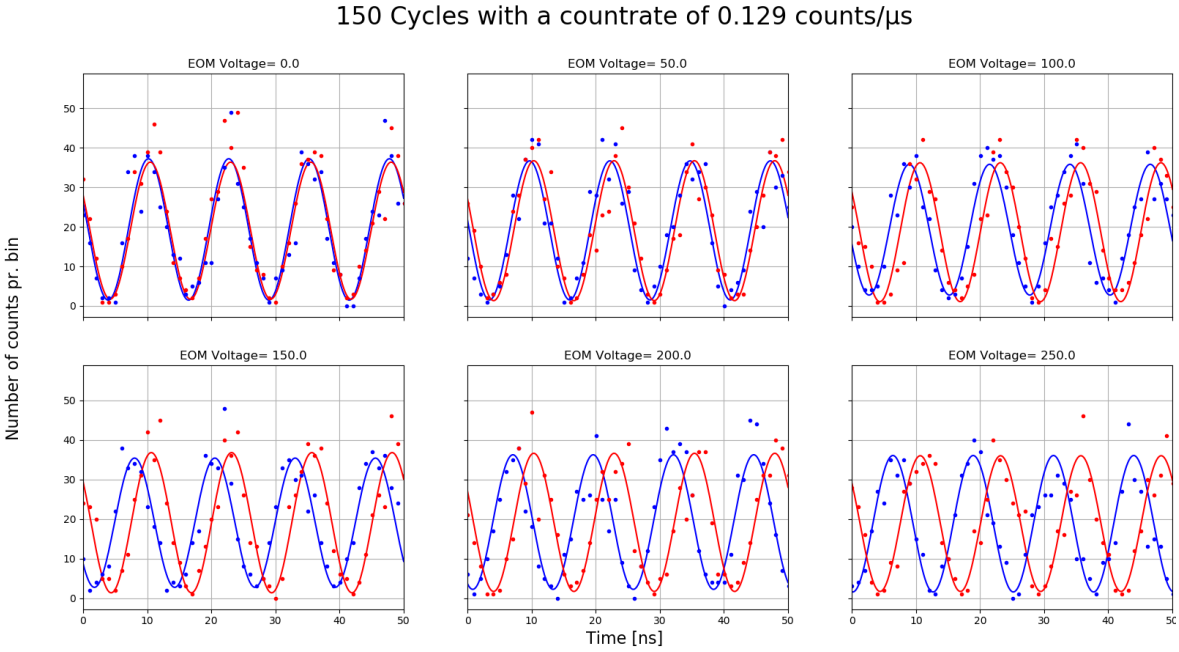

Figure 3.18: *Beat note signals detected for six different EOM voltages with 150 cycles added running at a count rate of 0.129 photons per µs. Data is taken for 400ns and fitted on the full set. Only the first 50ns is plotted for clarity.*

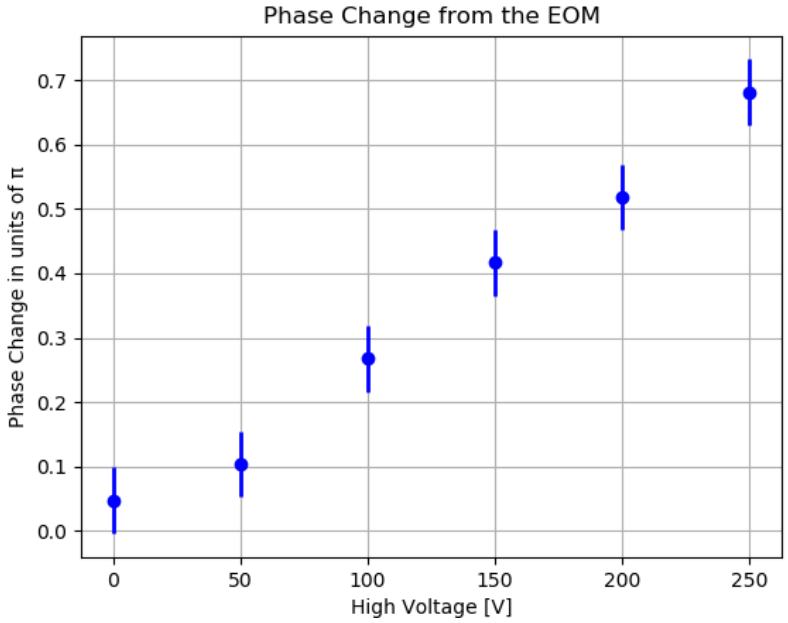

Figure 3.19: *Phase changed induced by the EOM as a function of the applied voltage with error bars being propagated standard deviation extracted from the covariance matrix. A total of 150 cycles are added with a count rate of* 0.129 photons/μs. *The standard deviation is roughly* 0.05π

The single-photon picture becomes increasingly accurate as the photon rate is reduced. However, there is always a trade-off to be made as the drift of the entire setup has increasing importance over long experiments. This is significantly more relevant for the test setup as the drift was determined to be 14° compared to the 1° measured for the simple setup. Increasing the stability of the interferometer allows for lower photon rates.

A dataset of 1000 cycles taken over 45 min is plotted in figure 3.20. The first 500 cycles are plotted in red and blue and the last 500 in green and yellow. A clear drift is seen which would wash out the contrast. It is, however, also clear that the phase shift induced by the EOM is not affected.

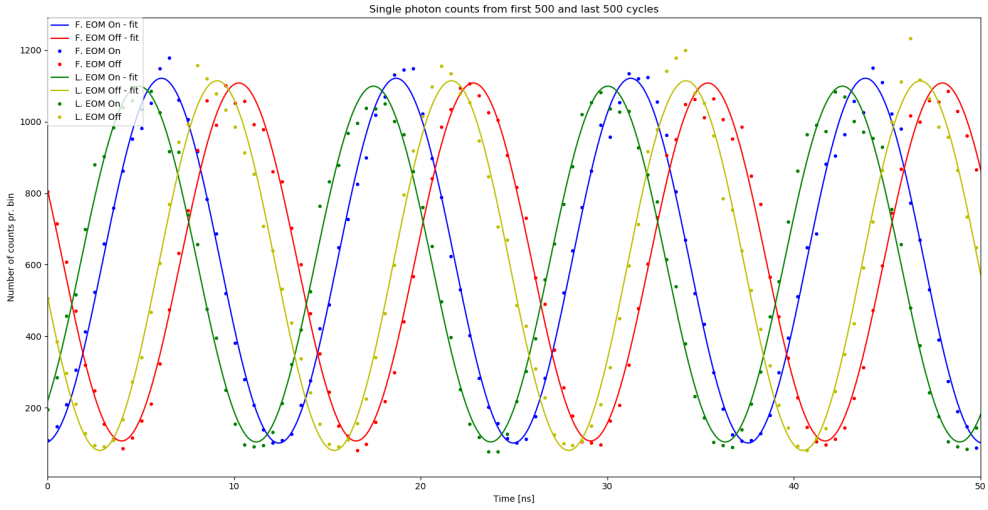

Figure 3.20: *Long-term stability measurement using single photons. The red and blue is the first 500 cycles and the green and yellow the last 500 cycles. A clear drift is seen during the 45min of measuring.*

Binwidth Analysis

To implement the interferometer into the experiment it is important to know what time resolution can be used for the data taking. The time resolution set by the Time Tagger is directly related to the binwidth. The binwidth is related to the file size with fewer bins resulting in small files. Therefore, it is of interest to find a binwidth for which the file size is small enough while still measuring the beat note at a sufficient level of details for our purpose.

The beat note has a period of 12.5 ns which leads to a theoretical minimum sampling rate of 6.25 ns. This is called the Nyquist limit and results from Shannon's sampling theorem [54, 55]. This theorem states that to be able to exactly replicate a periodic function, one must sample at least twice as fast as the period of the function. We tend to run our Rydberg quantum optics experiment using binwidths longer than 12.5 ns which is not sensible for this type of measurements. To reduce the amount of data and time resolution required, we investigate the uncertainty of the fit parameters coming from the covariance matrix of the fits. This is interesting as the Nyquist limit is not a strict limit in the sense that sampling slower leads to nothing but rather states when the signal will start to smear out.

All the data presented in this section is taken using the triggering procedure discussed earlier as well as the electronics in figure 3.4 and 3.8 with the EOM running at 250 V. The data are collected over 400 ns corresponding to 32 periods of the beat note signal. The fitting and analysis is performed using the full set of data, however, only the first 100 ns is shown for clarity.

In figure 3.21, a series of datasets taken with different binwidths are shown. A total of 13 data sets, using all integer values between 1 and 12, as well as 0.5 ns, was made and enters into the analysis. When fitting a sine-wave using Scipy.optimize curvefit in Python a covariance matrix is returned along with the value of the various fit parameters. This matrix can be used to obtain the standard deviation for each of the parameters [56]. The shaded area, primarily visible in figure 3.21d, is the result of the shaded area between the two functions 'fit $\pm 1\sigma$ confidence interval' for each parameter individually. A larger shaded area indicates a larger uncertainty. The 12 ns binwidth is clearly too large as there is essentially only one bin per period of the beat note.

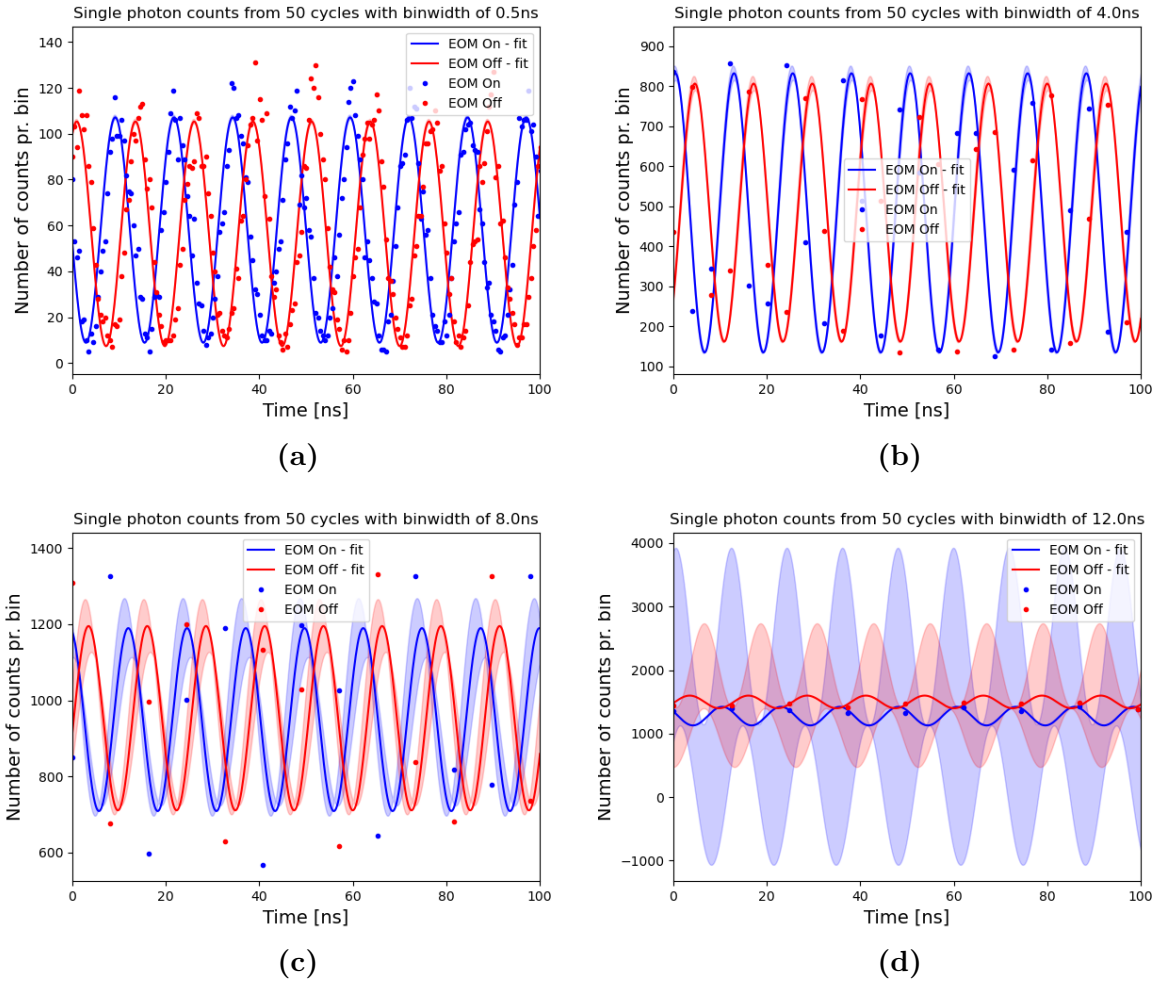

Figure 3.21: *A collection of phease measurements with different time bin widths of* ***a)*** 0.5 ns, ***b)*** 4 ns, ***c)*** 8 ns, ***d)*** 12 ns. *The shaded area is the area between the two functions, 'fit* $\pm 1\sigma$ *confidence interval'.*

As can be seen from the different panels in figure 3.21, the contrast washes out with increasing binwidth. The contrast is extracted from the fits and plotted in figure 3.22a. Ideally the system was so stable that if measured with high enough resolution, there would be zero clicks at the bottom of each period. This is not the case due to noise and drift. By increasing the width of a time-bin a single bin covers a larger part of the beat note signal curve. This part will have a slope, i.e. more clicks will happen in one "end" of the bin compared to the other. This information is lost when increasing binsize. By increasing the binsize beyond the Nyquist limit the function can not be reconstructed exactly and the fit more or less becomes a flat line with zero contrast at 12 ns. At 12.5 ns any contrast left would be noise, photon shotnoise or electronic noise, since a single period would fit exactly into a single time bin.

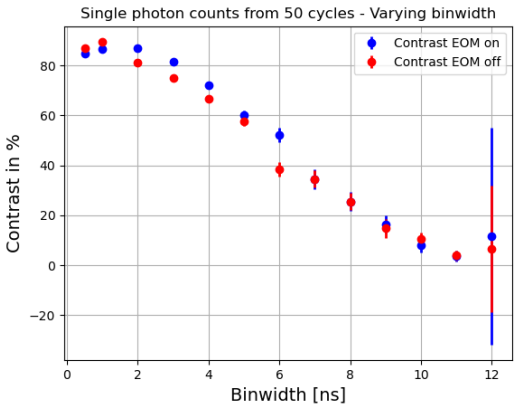

(a) *Contrast from fit to the varying binwidth data from figure 3.21. A clear linear drop is seen as well as what looks like a maximum around* 1 ns*. The error bars are one standard deviation on the fit parameter obtained from the covariance matrix.*

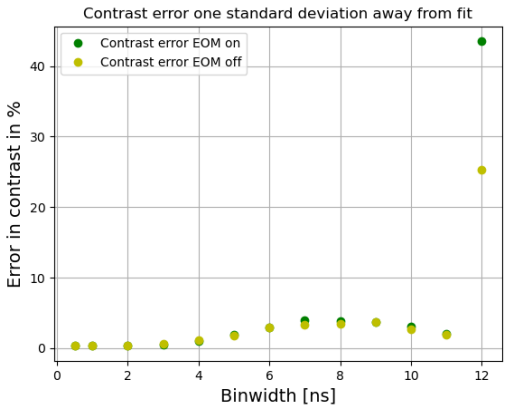

(b) *Standard error of the points on the graph to the left.*

Figure 3.22: *Contrast from varying binwidth and the standard error from the fits.*

There is also a lower bound to the binwidth beyond which, it makes little to no sense to decrease it any further. As seen from figure 3.22a there is no improvement in the contrast when going from 1 ns binwidth to 0.5 ns. This is presumably limited by the overall system stability and alignment. It could also be that a slight increase in contrast could be obtained by simply allowing the data collection to run for longer, but still on a timescale shorter than the overall drift. The count rate, i.e. number of counts per second, is a constant value leading to a total amount of incoming photons. By reducing the binwidth the number of chunks this number is divided into is increased and since the nature of single photons is not a coherent stream there will be more quantum noise in the measurement similar to the noise seen when too few measurements are taken. It was not examined further whether or not this could be the case as the desired conclusion could be drawn from the data presented here. Further work would, however, include experiments with more cycles and multiple datasets with binwidths around 0.5 ns. What can be concluded from this data is that a contrast of more than 60 % can be achieved for any binwidth obeying the Nyquist theorem as the sine-function can be fitted with very low error in this situation. The best contrast is achieved at 1 ns binwidth.

We are interested in measuring the phase shift and we now investigate how the binwidth influences the results. A similar analysis to the above has been made resulting in the two plots in figure 3.23a and 3.23b.

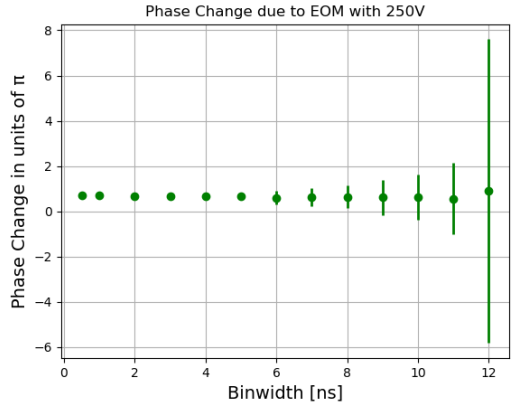

(a) *Phase change from fit of varying binwidth data from figure 3.21. The error bars are propagated standard deviations.*

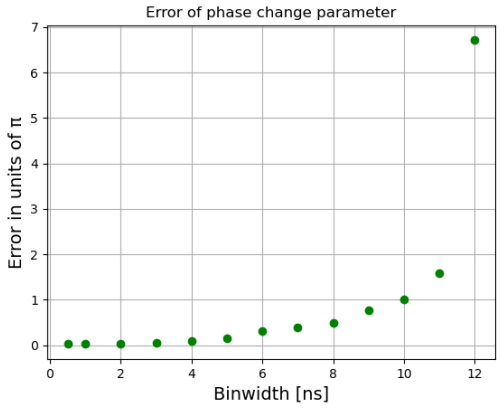

(b) *Standard error of the points on the graph to the left.*

The most important observation from this analysis is the very low standard deviation on the binwidths of size 3 ns and 4 ns. These, especially the 3 ns, have an error almost equal to that of the lower binwidths and could therefore provide phase change measurements of similar precision to the lower binwidths, if the reduced contrast can be accepted. This would be good when very long experiment cycles are performed and taking data every 0.5 ns or 1 ns will result in a huge overload of data. Overall the best result with the most precise measurements are obtained from the two lowest tested binwidths.

One could imagine a setup in which undersampling had to be performed for some reason. This will, as expected, greatly reduce the accuracy of the measured phase. Running at a binwidth of 8 ns could in theory work with a very large uncertainty of 0.5π on the phase, but above this value, the uncertainty is so large, with 10 ns corresponding to $\pm\pi$, that the phase is just an arbitrary number as a full turn on the unit circle is made.

In conclusion, a binwidth of 1 ns or less would be ideal when implemented into the experiment. For other measurements the Rydberg quantum optics experiment is typically recording data with time bins of 20 ns which is obviously too high. Taking 20 times as many bins will greatly increase the amount of data resulting in analysis scripts running extremely slowly. Therefore great care needs to be made when implementing the required code into the experiment as clever triggering will prove essential to only collect meaningful and essential data. How this was done is explained in the next section.

3.3 Interferometer Implementation

In this section, the phase interferometer is integrated into the running Rydberg quantum optics experiment. This first subsection discusses the important theory and the possible experimental regimes in which we can measure the phase of the light transmitted through an ensemble of ultracold atoms coupled to a Rydberg state. The next subsection describes key elements of the implementation process. These include the experimental sequence and the absorption of the probe laser. This description is followed by a subsection presenting our results. The section ends with an outlook on further interesting work to be done using the phase interferometer.

3.3.1 Phase Change of Atom Light Interaction

Two regimes are of interest for our experiments. Figure 3.24 shows the two regimes schematically. There is the possibility of creating a trap spatially confined to a radius less than the blockade radius of a Rydberg excitation. This is termed the super atom regime as only a single Rydberg excitation is possible. In the superatom regime, any Rydberg-Rydberg interactions are avoided. Alternatively a longer cloud, appropriately termed "the long cloud regime", can be investigated. This is characterized by supporting multiple Rydberg excitations. Such a regime is expected to be dominated by Rydberg-Rydberg interactions.

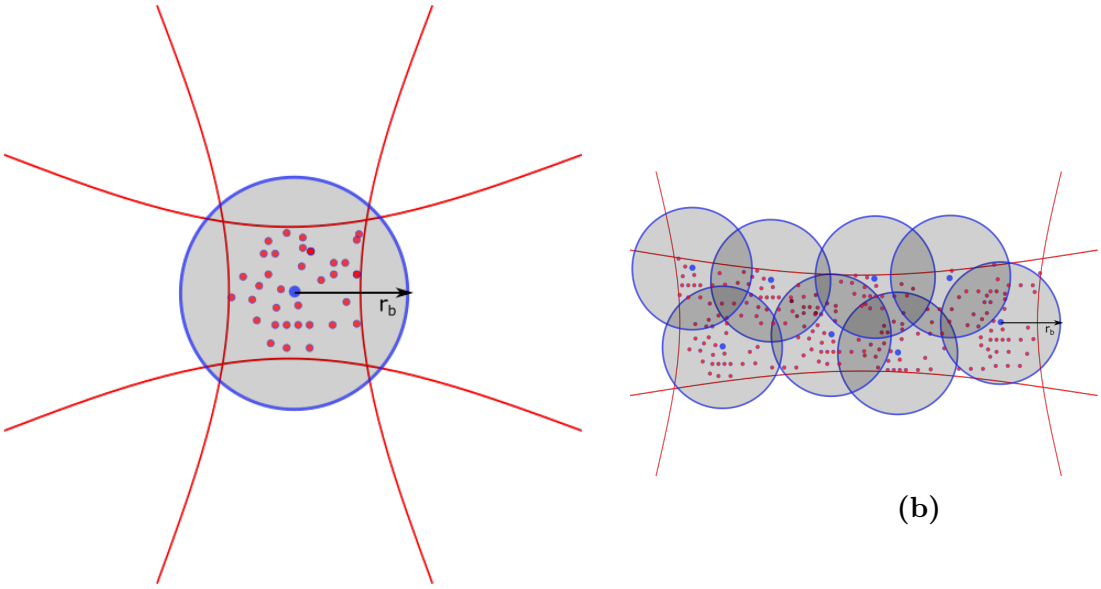

Figure 3.24: *The red lines represents the trap. Each of the small red dots represents an atom, while the bigger blue represents a Rydberg excitation with its important blockade radius r_b indicated by the blue circle.* ***a)*** *is the super atom regime. The trap is so tightly confined it only supports one Rydberg excitation.* ***b)*** *is the long cloud regime in which multiple Rydberg excitations can occur.*

The long cloud regime has been examined by other groups prior to our experiments. Our primary source of inspiration has been the work of the group of Vladan Vuletić [17]. We are interested in performing similar experiments to test our phase-detection setup.

They have shown, that for a fixed control laser and a probe scanning across two photon resonance, an increase in phase shift is observed when approaching two photon resonance and a change in sign occurs when the resonance is crossed. Based on there results we would also expect to observe a dependency on photon number.

The regime of the super atom would be of interest due to the effective two-level behavior when detuned from the intermediate state. By forcing the system to support only a single Rydberg excitation the fundamental effect of the phase of a photon interacting with a single Rydberg excitation, can be examined.

In what follows only the long cloud regime is considered and all measurements presented is done in this regime.

3.3.2 Implementation of Phase Interferometer

In the following, we describe the integration of the phase-detection setup. The integrated setup is the simple phase interferometer as we deal with atoms again. When measuring on atoms it is very important to think about whether or not the AOM adds or subtract 80 MHz from the light frequency. We are working with a blue-detuned probe laser, i.e. a probe laser of frequency slightly higher than that of the transition. Therefore it is important to choose the AOM orders such that the light is shifted 80 MHz further into the blue detuned regime. Alternatively, the probe is suddenly red detuned by 80 MHz minus the initial blue detuning. By choosing the order correctly the regime of one of the two interferometer beams interacting with the atoms while the other passes through unnoticed is realized.

The experimental setup and level scheme for the Rydberg quantum optics experiment is shown in figure 3.25.

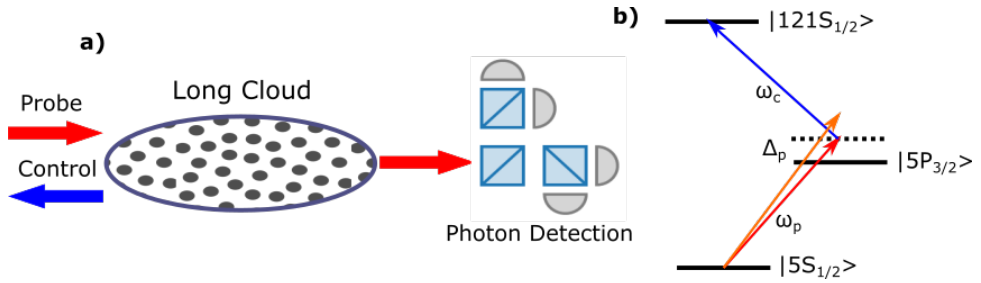

Figure 3.25: *Illustration of the Rydberg quantum optics experiment. The interferometer is integrated into the probe beam path before the cloud.* ***a)*** *Probe and control light is incident on a long atom cloud trapped in a dipole trap. Some probe light is transmitted and detected on SPCMs in a Hanbury-Brown-Twiss configuration.* ***b)*** *Level scheme of the experiment. The probe operates on the D2 transition at some detuning Δ_p with the frequency shifted part of the beat note even further detuned. The control light is adjusted for two-photon resonance to the $121S_{1/2}$ Rydberg state.*

The experiment operates on the D2 line and with the $121S_{1/2}$ Rydberg state. The probe is red detuned and the frequency shifted part of the beat note is shifted further off resonance. The probe and control are counter-propagating through an atomic ensemble trapped in a dipole trap. The transmitted probe light is detected on SPCMs in a Hanbury-Brown-Twiss configuration. The sequence for a scan is shown in figure 3.26.

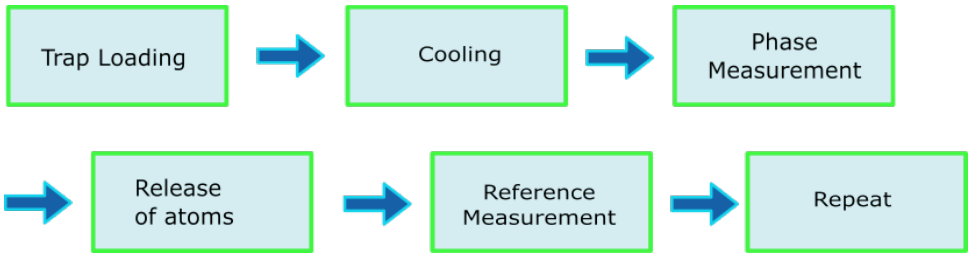

Figure 3.26: *Schematic representation of the experiment sequence. Atoms are initially loaded in a dipole trap. The loading is followed by a cooling time in which Raman Sideband Cooling is applied. The phase measurement consists of a sequence in which the dipole trap is turned off to measure the phase, then back on to trap the atoms. This is repeated 1000 times. Following this, the atoms are released by turning off the lasers. 1000 reference pulses are performed as the last step.*

Every scan starts with trapping atoms in a dipole trap. This is done using a MOT and strong magnetic field gradients and a strong dipole laser. The atoms are further cooled by a combination of evaporative and Raman Sideband Cooling. Once the atoms are trapped and cooled the actual experiment is repeated 1000 times. Measurements are done using a pulsating pattern in which the dipole laser is on, rapidly switched off, at which point the measurement is done, and then the laser is switched on again. Each of the 1000 pulses has a duration of $10\,\mu$s. The measurement is done with the dipole trap off to avoid any AC-stark shift of the atomic transitions. This sequence is followed by a release of the atoms by turning off the dipole trap light. The final step in the scan sequence is taking 1000 reference pulses using the same pulse pattern as with the atoms present. The pulsating dipole trap laser is also used here even though there are no atoms to trap to have similar background-noise conditions for all measurements.

All measurements presented in the next section are performed in what we term "a long cloud". As discussed in section 1.4.3 Rydberg atoms exhibit a blockade type of effect by shifting the energy levels of atoms in the near vicinity preventing additional excitations. A long cloud thus requires a lot of atoms which results in an optical depths of $OD = 38$ for our experiment. The OD is a single parameter from a fit. An OD-curve is a scan of the probe laser across the atomic resonance. Such a scan is shown in figure 3.27.

This scan is taken for the "pure" probe laser beam. If the interferometer is turned on and the first AOM adjusted to obtain 50% of the probe light in the reference detuned by 80 MHz, the scan reveals two absorption features. Such a scan with the AOM on is shown in figure 3.28. In that case, there are two resonances at which either beam is resonant with the atomic transition. In such a scan the valleys settle at 50% transmission corresponding to one of the beams passing unnoticed through the atoms.

In this figure, the measured transmission is sub 50% in both arms. This is due to the slight overlap of the absorption valley of the two beams.

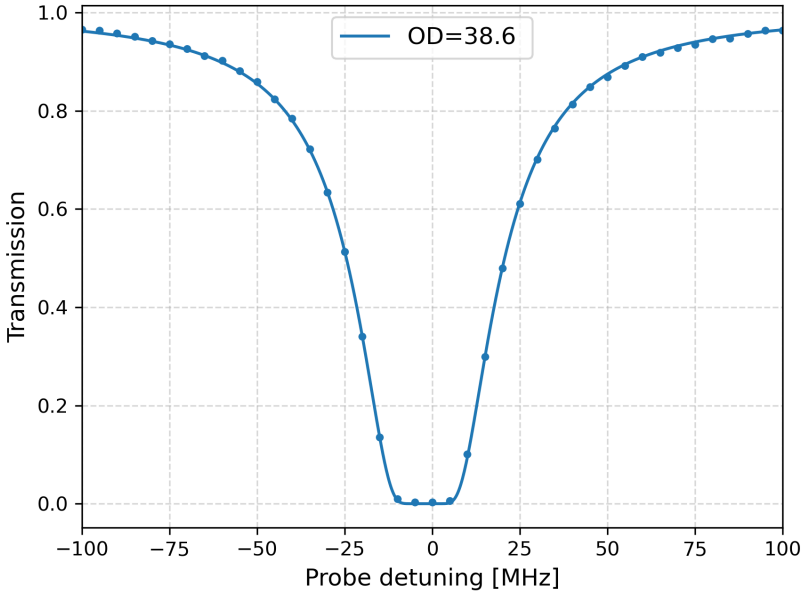

Figure 3.27: *Scan across resonance of the pure probe laser. The data is shown as transmission vs detuning from probe resonance. A transmission curve with the OD as fitting parameter is fitted to the data and a total of* $OD = 38.6$ *is obtained*

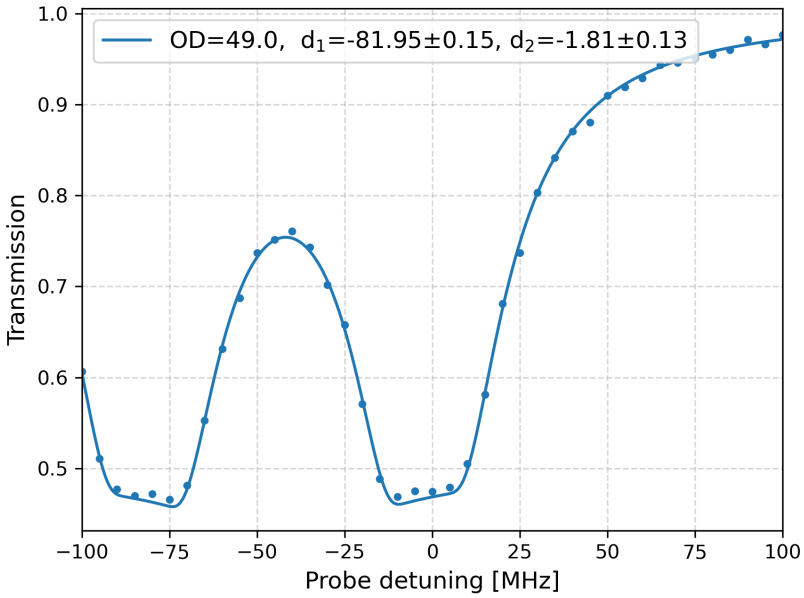

Figure 3.28: *Scan across resonance of the probe laser with the interferometer on to create a beat note pattern. The two valleys are located at the zero detuning due to the probe and the* 80 MHz *shifted frequency corresponding to the absorption of the other part of the beat note. The transmission goes below 50% in both of them as some light of the shifted beam is absorbed.*

The measurements presented in the next section are performed at some probe detuning and some control detuning matched such that we are always on two-photon resonance. The probe detunings chosen were 20, 40 ,70, and 100 MHz respectively. No measurements are done at EIT resonance, i.e. probe and control on resonance, as there is simply not enough light going through the cloud to measure on.

3.3.3 Phase Measurements

In this section, the results of phase measurements in the long cloud regime are presented. Measurements were performed at 20, 40 ,70, and 100 MHz detuning of the probe laser. The control laser is adjusted such that two-photon resonance is obtained to induce a coupling to the Rydberg state. We measure the phase of the transmitted light as a function of photon number. This is done to examine the behavior of the phase change as a function of the photon rate. The number of repetitions is different for different photon numbers and detuning. To obtain sufficiently good data more scans are needed with fewer photons and lower transmission.

The actual data collected is similar in structure to the test setup. The combined repetition show the oscillating behavior of the beat note signal. A plot showing a small part of a dataset is shown in figure 3.29.

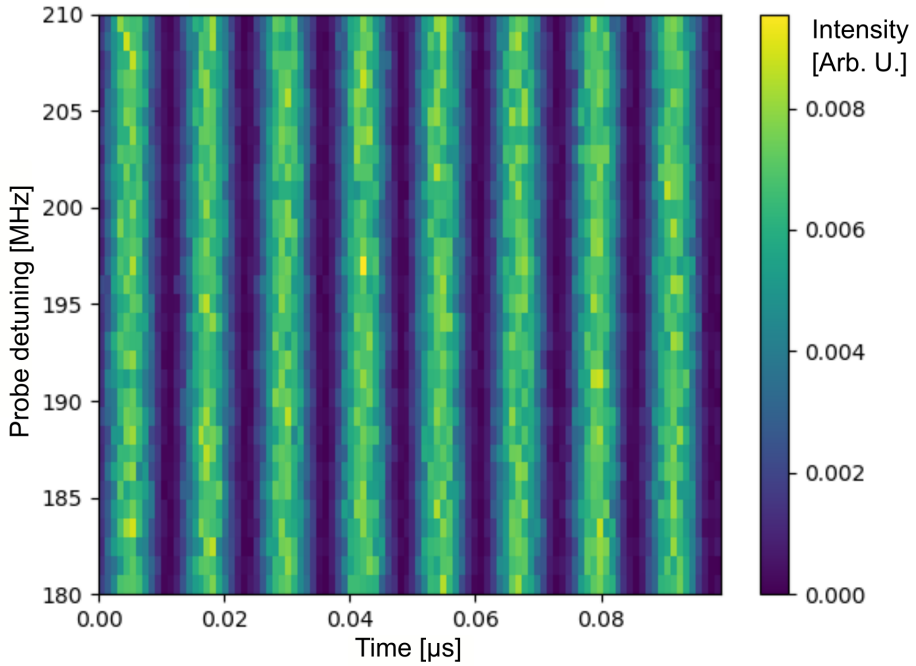

Figure 3.29: *Time trace vs the detuning of the probe. The color scale shows the number of photons. The color shows a clear periodic signal to which a sinus-curve is fitted to each line.*

In this figure, the time is plotted against the probe detuning. The color scale is the number of photons and is what shows a clear period pattern. For each probe detuning, a sine-curve is fitted to the beat note and from this fit, the phase is extracted. The phase shift is determined when similar fits are made to the data without atoms.

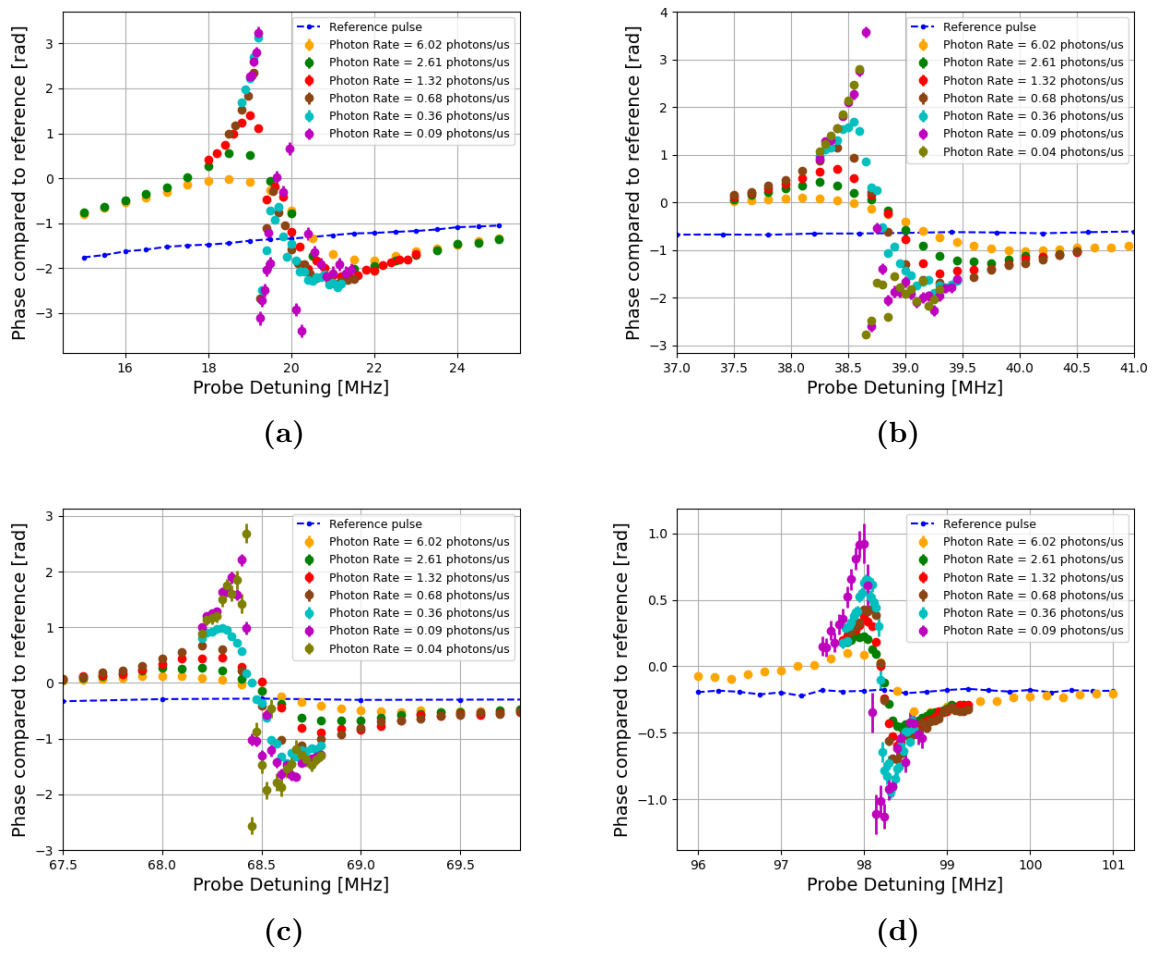

Figure 3.30: *Phase plots.* ***a),b), c), d)*** *shows the phase shift induced on the probe for detuning of* 20 MHz, 40 MHz, 70 MHz, 100 MHz *respectively. An increase in the sharpness of the phase change feature can be seen for decreasing photon rates in each plot. The total phase shift is increasing with lower probe detuning. At the lowest photon rates for each detuning there is so little light going through that fitting a sinus becomes difficult hence the outliers around resonance.*

In each of the four panels of figure 3.30 the data for the four chosen probe detunings are presented. It is very clear that the feature sharpens for lower photon rates. It is also clear that the total phase change increases with decreasing photon rate as well as decreasing probe detuning. This shows good agreement with our expectations and the data. It is worth noticing that very little light is transmitted through the cloud at the lowest photon rates. This eventually leads to so little contrast between the constructive and destructive interference windows in figure 3.29 that fitting a sinus becomes impossible. This is the reason for outliers at these low photon rates.

3.3.4 Conclusion and Further Work

In this section, the implementation of the phase interferometer tested in the previous sections of this chapter was implemented. By inserting the optics into the probe of the running Rydberg quantum optics experiment and implementing the data acquisition with the triggering discussed in section 3.1.2 it was possible to measure the phase change of Rydberg atoms in the regime of the long cloud. In this regime, the interactions were dominated by Rydberg-Rydberg interactions. We have demonstrated a similar behavior of the phase change as shown in other works [17]. This consists of a phase change increasing as two-photon EIT resonance is approached and a change in sign when passing through resonance. This effect was shown to give an increasing phase shift with decreasing probe photon rate. It was also shown to increase when probe resonance was approached.

For further work, it would be of interest to measure the phase shift at more probe detunings for a fixed photon rate. Currently, only four detunings were examined, and extending this to eight or ten would make it possible to create a plot of phase change vs detuning for a given photon rate. Furthermore, this would be an interesting plot for multiple photon rates.

It is also of interest to go to the super atom regime. In this regime, the trap is spatially limited to only support a single Rydberg excitation. This allows for investigation of the phase change imprinted by interaction with a single excitation and completely neglects Rydberg-Rydberg interactions.

Chapter 4

Vapor Cell EIT

In this chapter, an experiment with EIT in a vapor cell is presented. The theoretical foundation leading to this experiment was proposed by Lida Zhang and Thomas Pohl from the University of Aarhus in early march 2021 and shows a possibility of realizing non-reciprocal optics with experimentally feasible parameters. In section 4.1 an overview of the theory is given. The theory shows that the observation of electromagnetically induced transparency in a ladder scheme is widely different depending on the relative propagation direction of the two EIT fields, hence the reciprocity of the scheme. If the two EIT fields are co-propagating, no EIT feature is expected. If the two beams are propagating in opposite directions, a transparency window is expected. Further, the shape of the EIT peak may be broadened compared to what we normally observe in ultracold atoms in the case of high Rabi frequency on the upper transition. These effects are caused by atomic motions.

In section 4.2 it is discussed how the theoretical predictions are investigated experimentally and the results are shown in section 4.4. The experimental setup utilizes the second harmonic generated 480 nm laser output from the 960 nm laser that was locked to the cavity as the control laser and the 780 nm laser used throughout all work of this thesis as the probe laser.

Non-reciprocal effects have been realized in other areas of physics over the past years. In solid-state physics, Faraday isolators have long been known to exhibit non-reciprocal behavior but they prove too bulky in fabricate for ultralow light levels. For non-bulky systems like waveguide and microcavities, such non-reciprocal effects have been shown for large intensities and are not compatible with ultralow light levels [19, 20]. Alternatively, using time modulation of wave-guide properties has shown promising results for non-reciprocal transmissions at ultralow light levels [21]. Nanophotonic optical isolators fulfilling both requirements of exhibiting non-reciprocal transmission behavior while being possible to fabricate have been shown [57]. Common for all of these techniques is the costly fabrication of highly specialized components. In our scheme, we realize these effects by purely optical means. The only requirement is a vapor cell and two lasers making it a very simple way of realizing non-reciprocal optics.

4.1 Theoretical Proposal

The theoretical background for the non-reciprocal scheme implemented in the following sections was proposed by Lida Zhang and Thomas Pohl from the University of Aarhus [58]. The idea is to utilize the velocity distribution of the atoms in a hot atomic vapor. The level structure required is a ladder scheme with the k-vector for the upper transition higher than the lower. The level scheme and the definition of co- and counter-propagating are shown in figure 4.1.

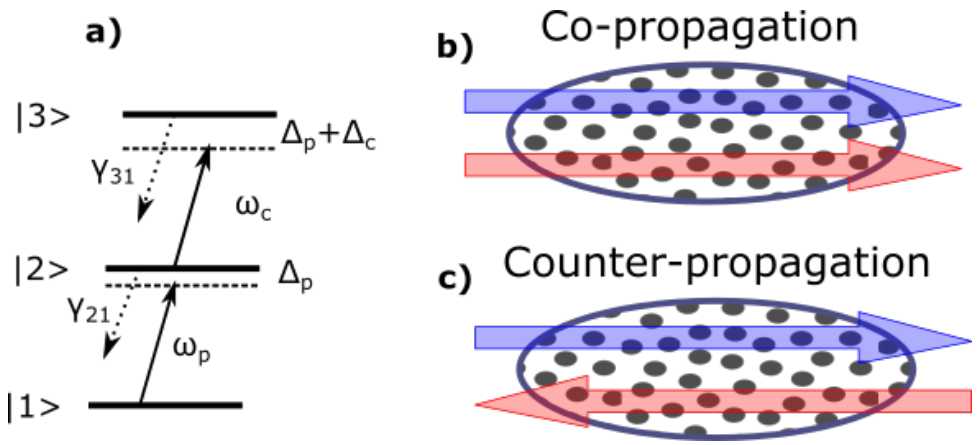

Figure 4.1: *In **a)** the ladder scheme is shown with the three states $|1\rangle$, $|2\rangle$, and $|3\rangle$. In **b)** and **c)** the definition of co- and counter-propagation is seen.*

The transition from the ground state to the intermediate state $|1\rangle \rightarrow |2\rangle$ is taken to be in the single photon regime while the transition from the intermediate state to the excited state $|2\rangle \rightarrow |3\rangle$ is done with a strong classical field with Rabi frequency Ω_c. The Rabi frequency must be large enough to result in the avoided crossing between the dressed states to see the broadened EIT feature we seek.

Owing to the strong classical field coupling $|2\rangle \rightarrow |3\rangle$ the excited state will split into two dressed states. In the situation of counter-propagating probe and control, the dressed states will have energies depending on the probe and control wavenumbers and detunings, as well as on the velocity of the atoms in the atomic vapor:

$$\lambda_+ = -\Delta_p + k_p v_z \tag{4.1}$$
$$\lambda_- = -\Delta_p - \Delta_c + (k_p - k_c)\, v_z \tag{4.2}$$

These equations hold for large atomic velocities [58]. The two photon transition will experience a Doppler shift given by

$$\nu_D = (k_p - k_c)\, v_z. \tag{4.3}$$

The Doppler shift will have a negative sign for $k_c > k_p$ which in wavelength reads $\lambda_p > \lambda_c$. The negative Doppler effect gives rise to an avoided crossing, as shown by the blue line in figure 4.2, between the two dressed states which results in a broadened EIT spectrum. This is different from the situation of co-propagation of the probe and control fields as the two-photon Doppler effect equals the single-photon effect in the case of a co-propagating setup. This leads to no avoided crossing between the dressed states and a constant

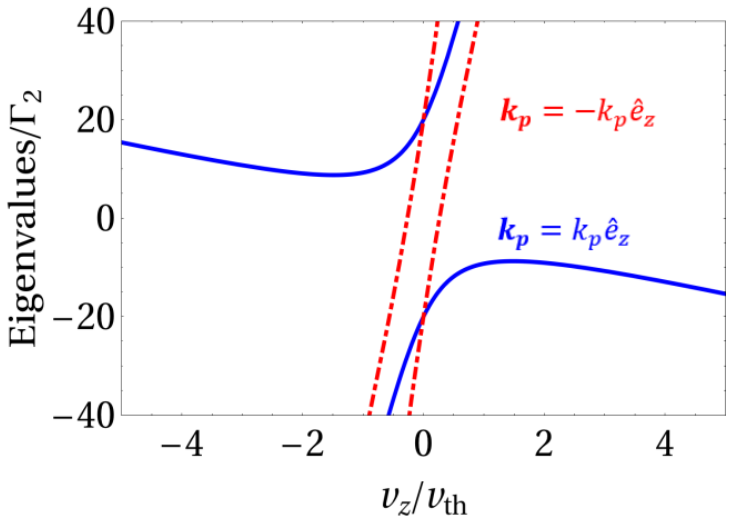

Figure 4.2: *Behavior of the two eigenvalues of the dressed states as a function of velocity. The blue shows the avoided crossing for the counter-propagating case. The red curve is for co-propagating probe and control. The figure is a courtesy of Lida Zhang.*

absorption will be experienced by the probe photon.

A single absorption valley can be described using the following two equations which are semi-classical susceptibilities with the velocity of the atomic vapor taken into account [23].

$$\chi_{co} = \int_{-\infty}^{\infty} \frac{iN(v)\mu_{21}^2/\left(\hbar\varepsilon_0\right)}{\gamma_{21} - i\left(\Delta_p - \frac{k_p+k_c}{2}v\right) + \frac{\Omega_c^2/4}{\gamma_{31}-i(\Delta-(k_p+k_c)v)}} dv \tag{4.4}$$

$$\chi_{counter} = \int_{-\infty}^{\infty} \frac{iN(v)\mu_{21}^2/\left(\hbar\varepsilon_0\right)}{\gamma_{21} - i\left(\Delta_p - \frac{k_p+k_c}{2}v\right) + \frac{\Omega_c^2/4}{\gamma_{31}-i(\Delta-(k_p-k_c)v)}} dv \tag{4.5}$$

Here $\Delta = \Delta_p + \Delta_c$ is the two-photon detuning. $N(v) = N_0 e^{-v^2/u^2}/\left(u\sqrt{\pi}\right)$ is the velocity distribution of the atoms with v being the velocity and u being the most probable velocity. N_0 is the density of atoms given by the vapor pressure which changes with temperature. k_p and k_c are the respective probe and control wavenumbers. μ_{21} is the dipole moment between the ground and excited state. Ω_c is the control rabi frequency which is given by the power of the laser and the state we address. γ_{21} and γ_{31} are the dephasing rates between the respective levels, ground (1), excited (2) and Rydberg (3). These two parameters contain all the imperfections, such as laser linewidth leading to broadening, etc. When fitting these equations γ_{31} is set to some fixed value and γ_{21} is fitted.

Since the EIT is observed in the probe field, it is important to work in a regime where absorption of this field is not saturated, i.e. well below the saturation intensity. The saturation intensity for the D2 line in rubidium is $I_{sat} = 2.50\,\mathrm{mW/cm^2}$ [30]. For a beam waist of $55\,\mu$m as in the experiment presented in this chapter, this corresponds to a saturation intensity at the focus of the probe of

$$P_{sat} = I_{sat} \cdot A_{beam} = 0.24\,\mu\mathrm{W}. \tag{4.6}$$

To be in the weak probe regime powers of a few nW is required.

4.2 Experimental Setup

The general proposal from Zhang and Pohl can in principle be realized in any atomic system where a ladder scheme with $k_c > k_p$ can be implemented. In our case, we had a rubidium vapor cell available, and lasers at 780 nm and 480 nm, which satisfies the requirement of $k_c > k_p$. We probe the rubidium atoms on the D2-line and excite them to the $20S$-state which is a Rydberg state. The final experiment design is shown in figure 4.4. In the following the design choices of this setup are discussed.

The setup consists of a 780 nm probe laser to probe the rubidium atoms via the D2 line. The probe comes out of a fiber and is split in two beams with polarization optics. One of the two beams propagates together with the control light, while the other propagates in the opposite direction of the control beam. The 480 nm control beam is overlapped with the probe using dichroic mirrors. Both beams are focused into the cell using a $f = 200$ mm and $f = 300$ mm lens respectively. The beams are overlapped using a camera and further optimized on the EIT signal once obtained.

The Excited State

While the first and second states in figure 4.1 are known, state $|3\rangle$ is yet to be chosen. We have a TA-SHG laser available for this excitation which forces us to excite to a Rydberg state. As figure 4.3 shows, the Rabi frequency decreases with the principal quantum number. Since the widening of the EIT window predicted by Zhang and Pohl is only reached for very high Rabi frequency, we aim for the lowest possible Rydberg state.

However, the TA-SHG laser is designed to work optimally at 480 nm and while it can be tuned in wavelength, the TA-chip will have a rapid drop-off in efficiency if tuned too far. As a trade-off, we choose the $20S$ state. We chose a Rydberg S-state as opposed to a D-state due to the simplicity in the level structure of the S-state This requires tuning of the 480 nm laser to 488.08 nm. At this wavelength, an output power of 0.9 W was measured.

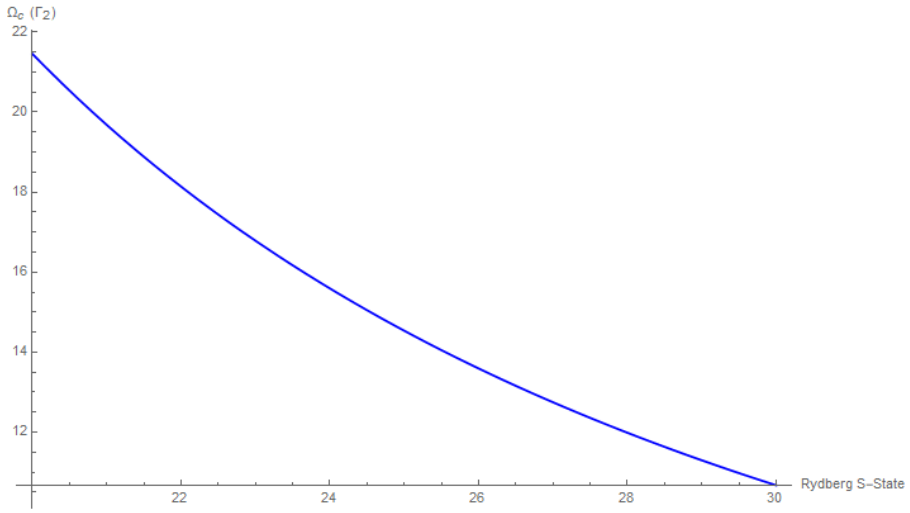

Figure 4.3: *Control rabi frequency in units of* Γ_2 *as a function of Rydberg S-state in the interval* $n = 20$ *to* $n = 30$ *for a beam waist of* 55 μm *and a power of* 1 W.

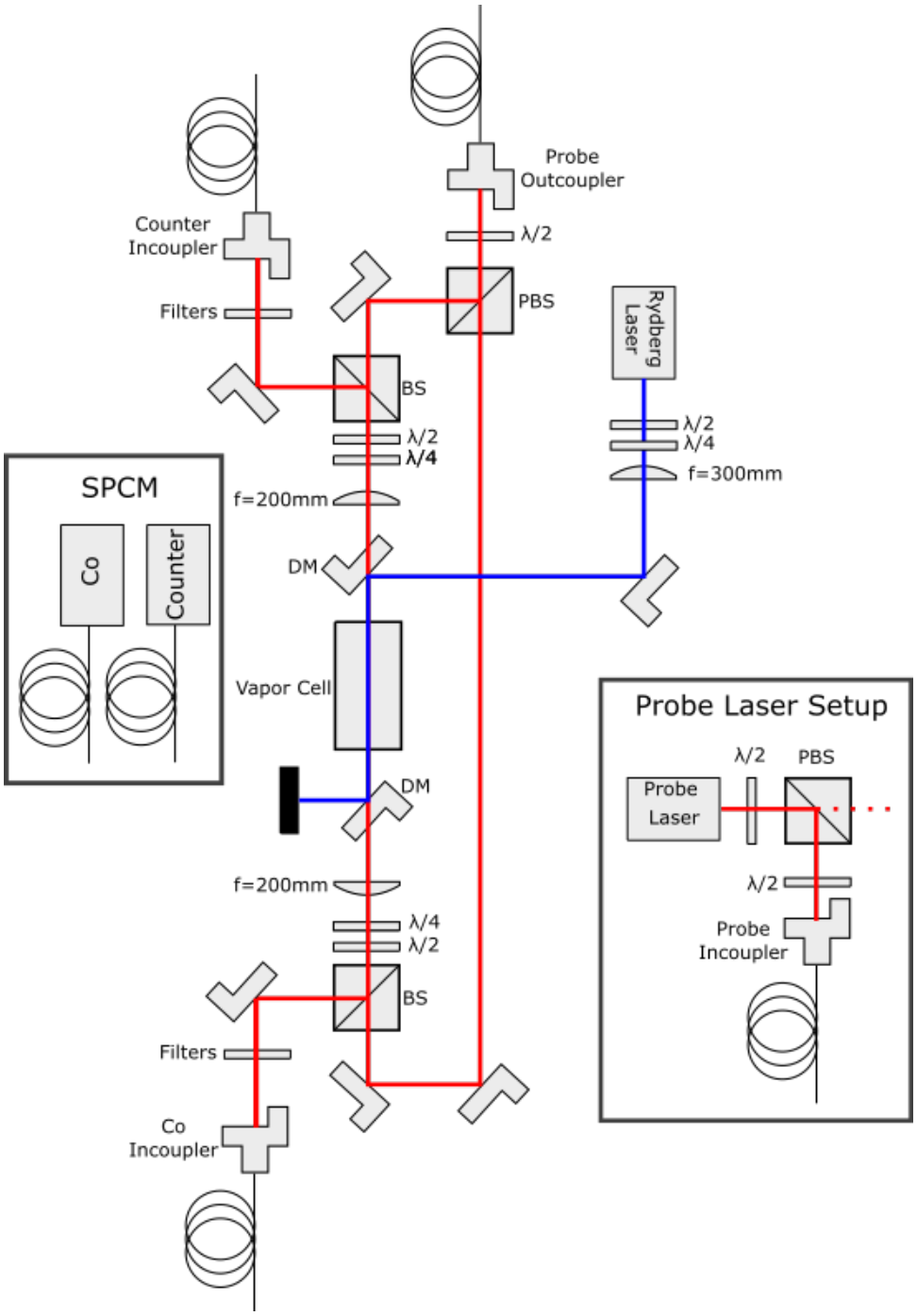

Figure 4.4: *Illustration of the final vapor cell setup. The probe laser setup box shows the setup before the fiber for intensity control. The probe is split and overlapped with itself. The control is overlapped and separated via dichroic mirrors. The HWP and QWP setup in each arm is to adjust the polarization going into the cell. After the cell, the probe is coupled to a fiber going to an SPCM after passing through some filters. For higher intensity probes the fibers are replaced with photodiodes.*

Vapor Cell

The key element of this setup is the vapor cell. We used a 50 mm vapor cell containing a natural abundance of rubidium. To control the vapor pressure in the cell and the atomic velocity, the cell was wound in a coil and mounted with a cell heater. To have proper control of the atoms in the vapor cell a coil of copper wire was winded around the cell as uniformly as possible. By sending a current through the coil it heats up and is used to heat the cell from the side. The current in the coil also results in a magnetic field which gives a preferable quantization axis. This is used to give the best coupling between the ground and the excited state as the polarization can be aligned with all the atoms' preferred direction. In addition to the coil, we used a home build cell heater to address the temperature of the vapor cell. The cell heater consists of two copper plates to which a power resistor was attached. The copper plates were adjusted to touch the ends of the cell. The cell was further isolated in alu-foil. The temperature was measured using a thermistor. However, the thermistor was placed on the outside of the glass cell, and it does, therefore, not necessarily give the exact temperature. Therefore, the temperature is also extracted from fits to the absorption curve.

Lenses

In the proposal from Pohl and Zhang, a distinct widening of the EIT feature is expected to occur for high Ω_c.

With approximately 1 W 480 nm light available, and to achieve the highest possible Rabi frequency, we focus both the probe- and control beam tightly in the cell. We focus both beams to a spot-size of 60 μm with the lenses shown in figure 4.4. The foci of the beams were characterized as shown in figure 4.5. The characterization is done using a camera moved through the focus. Focusing the beams to a 60 μm waist gives a high control Rabi frequency, but with a trade-off in form of non-uniformity. Therefore, the atoms in the cell will have a non-uniform response to the probe and control field. However, for a first demonstration of the predicted effect, we do not take this non-uniformity into account.

Polarization control and Intensity Adjustments

Initially, the intensity is attenuated before the fiber with filters and polarization optics. In the setup itself, polarization optics are used to split and balance the probe beam intensity in the two arms which are co- and counter-propagating with the control beam respectively.

The use of polarization optics to split and balance the intensity was chosen over a 50:50 BS setup to allow for Doppler spectroscopy. This type of spectroscopy requires highly imbalanced laser powers.

As the exact desired polarization is unknown, as well as the direction of the quantization axis, at the time of designing the setup it was created to have full flexibility. This includes a setup of a QWP and HWP in each of the three arms (co- and counter probe, and control). After the probe has passed through the cell a 50:50 BS setup was chosen. This was such that light would go to the detector no matter the polarization hence giving the highest flexibility of the setup.

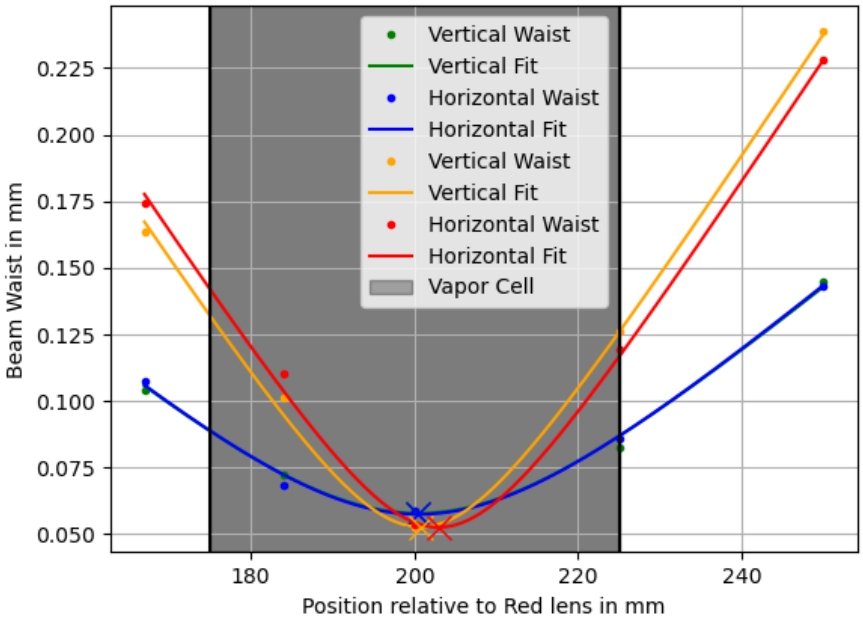

Figure 4.5: *Characterization of the focus of the probe and control beams. Each data point corresponds to a Gaussian fit in either horizontal or vertical direction to an image of the beam. The images were taken with a camera, which was moved through the focus. The blue and green are the control laser with the waist determined on the horizontal and vertical axis respectively. The orange and red are similar but for the probe. The black lines and shaded area indicate the placement of the vapor cell.*

Detection Method and Filtering of the blue

Initially, the probe beams were detected on photodiodes[1]. However, for the weak-probe regime, it was necessary to go to single-photon detection. To detect the very weak probe light used in this setup SPCMs from Laser Components were used.
The light coming from the vapor cell and reflected off the 50:50 beamsplitter was coupled into a fiber connected to the counter module.

In order to filter out the very strong control light, filters from Laser Line[2] were used before the fiber couplings in both probe directions. The filters has a transmittance of 93 % at 780 nm and $OD = 7$ at 480 nm.
In addition, the beam path, after the 50:50 beamsplitter, of the co-propagating probe beam was made very long. Thereby some spatial separation of the probe and control light was achieved.
However, a non-vanishing contribution from the blue light is visible in both probe directions. This contribution could be reduced further by adding a second fiber and laser line filter in the path from the experiment to the detector.

[1] Thorlabs - DET10A2
[2] Semrock - FF01-780/12-25

4.3 Spectroscopy

In this section, the content of the vapor cell is examined using spectroscopy. Both ordinary spectroscopy and Doppler-free spectroscopy has been performed.

Figure 4.6 shows a scan across all possible transitions $5S_{1/2} \rightarrow 5P_{3/2}$. There are two F levels of each of the isotopes. From atomic physics we expect an absorption feature for each of the F-levels, i.e. four features in total. These are $^{85}Rb\ F = 2 \rightarrow F'$, $^{85}Rb\ F = 3 \rightarrow F'$ and similarly for $^{87}Rb\ F = 1 \rightarrow F'$ and $^{87}Rb\ F = 2 \rightarrow F'$. From the energy spacing of the hyperfine levels of $5S_{1/2}$ states the order (from left to right) of the absorption features can be determined. From lowest to highest frequency: $^{87}Rb\ F = 2$, $^{85}Rb\ F = 3$, $^{85}Rb\ F = 2$, $^{87}Rb\ F = 1$.

For the case of Doppler-free spectroscopy the hyperfine structure of the excited $5P_{3/2}$, state is expected to be visible. The substructure of the absorption valleys is given by the selection rules, i.e. $\Delta F = 0, \pm 1$. The strength of the transition, which is visible in the height of the peak in the spectrum is given by the corresponding Clebsch-Gordan coefficient.

To find the transition from the ground to the excited state, the DFB laser was scanned over a long range of many GHz. The scanning was done using a function generator to apply a ramp-pulse. By adjusting the laser controller and pulse generator a signal was obtained on a photodiode.

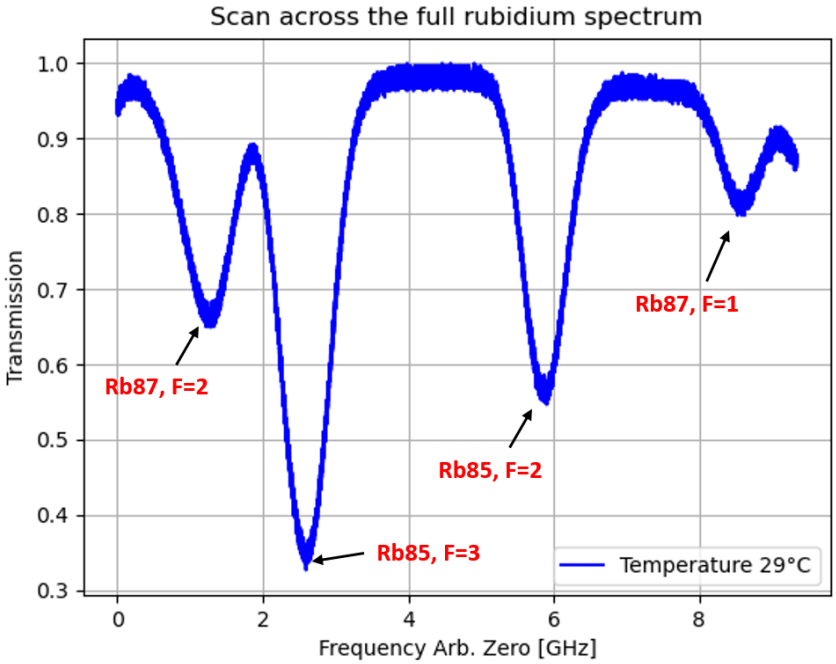

Figure 4.6: *Rubidium Spectrum of the $5S_{1/2} \rightarrow 5P_{3/2}$ transition. Four absorption valleys corresponding to the four transitions from the $5S_{1/2}$ ground state with two hyperfine states for each isotope. The substructure is hidden due to the Doppler broadening.*

In figure 4.6 the rubidium spectrum is seen. The spectrum is measured at roughly room temperature. The scan is adjusted such that the full spectrum is visible by adjusting the voltage on the function generator. The spectrum has four clear valleys corresponding to each of the four transitions as discussed above. It is important to note that the ^{87}Rb, $F = 2$ and ^{85}Rb, $F = 3$ transitions are close enough in frequency that their absorption valleys overlap. This is evident as the signal does not reach 1, which equals full transmission, between the absorption. This overlap will only increase with temperature and these transitions will essentially have to be treated as a sum of two individual contributions. The depth of the absorption valley does not reach zero, i.e. 100% absorption, in the above spectrum. This is due to the optical depth, which depends on the number of atoms in the vapor, being too low compared to the intensity of the light. The spectrum was made using a probe of some hundreds of μW which is far beyond the saturation intensity.
For the experimental realization of the effect, the scan was limited to the ^{87}Rb, $F = 2$ and $^{85}Rb, F = 3$ valleys. These two valleys have the highest absorption and the frequency between them is precisely known and can be used as a reference.
The full description of the spectrum across such a scan is the sum of two individual contributions as the light interacts separately with the two isotopes. Mathematically this would be $\chi_{co} = \chi_{co^{87}Rb} + \chi_{co^{85}Rb}$, with the two components of the spectrum have different dipole moments, detunings and dephasings.

Doppler-Free Spectroscopy

The Doppler-free spectroscopy is performed by having one strong beam saturating the medium and another beam of much lower intensity and opposite propagation direction on which the transmission peaks are measured [22]. A transmission peak will be visible when the frequency of the laser corresponds to a given hyperfine level, and when it is exactly between two resonances. The latter are called crossover resonances and stem from the interaction with atoms with a specific longitudinal velocity class. For each set of resonances, there is a crossover resonance. If there are three hyperfine levels a total of three crossover resonances should be visible, $1 \leftrightarrow 2, 1 \leftrightarrow 3, 2 \leftrightarrow 3$.

Assuming a velocity component v_z of the atoms in the direction of the probe the Doppler shift becomes

$$\nu_D = \nu_l \left(1 \pm \frac{v_z}{c} + \frac{v_z^2}{2c^2}\right). \tag{4.7}$$

Here ν_l is the laser frequency [24]. The last term is the relativistic Doppler effect which has not been considered in this work. The plus sign is for counter-propagating atoms with respect to the probe beam and the negative sign the same for the co-propagating atoms.

The Doppler-free spectrum shown in figure 4.7 was realized using a strong probe many orders of magnitude above the saturation intensity and a very weak probe from the other direction. While weak relative to the photodiodes detection range the probe was not attenuated to be in the weak probe regime as this was not possible with the used detectors.

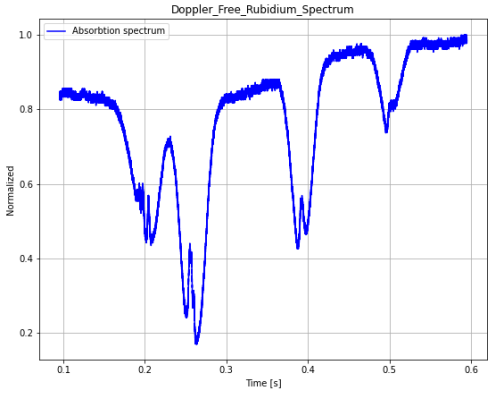

(a) *Doppler Free Spectrum. Each of the absorption valleys has the substructure expected from the atomic physics data.*

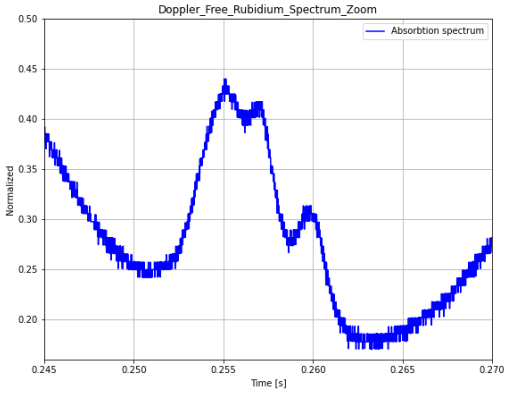

(b) *Zoom on the Doppler Free Valley of the* $^{85}Rb, F = 3$ *valley.*

Figure 4.7: *Doppler-free spectrum with lines clearly resolved.*

Blue two photon resonance

To find the correct frequency for the control laser, the laser was scanned close to the expected transition frequency, $\omega_c = 614.23\,\text{THz}$ for the $20S$ state, while the counter-propagating probe signal was observed. When a small EIT peak was seen, the scan range and offset of the control laser were adjusted so a signal was seen without scanning the control laser. This signal was used to optimize the alignment of the control beam and the polarization of the beams.
The laser frequency was chosen such that the highest EIT peak was seen. This is not necessarily coinciding with the control laser being on resonance with the $|2\rangle \rightarrow |3\rangle$ transition. This will be further discussed towards the end of the next section.

4.4 Realization of the non-reciprocal scheme

In this section, the results of the experiment are presented and discussed. First, the initial results are shown. These are followed by a discussion of possible improvements. Following this, experimental results of the improved setup are presented. Finally, a discussion of how to further improve the experiment is presented.

It is important to notice, that measurements on the co- and counter-propagating probe beams are not performed simultaneously. This is due to undesired interference effects which could not be eliminated by adjusting the polarization of the probe beams. Therefore, data for each direction is taken just after one another and not simultaneously. There is but a minute between the data collection for either side as only a single beam block had to be moved.

First Realization of the effect

The first non-reciprocal EIT signal observed is shown in figure 4.8. For this first observation, the temperature of the cell was approximately 27 °C, the Rydberg state was $30S_{1/2}$ and the control power was 1 W.
The DFB-laser was used as the probe laser and it was scanned over the $^{85}Rb\, F = 3 \rightarrow F'$ absorption line.

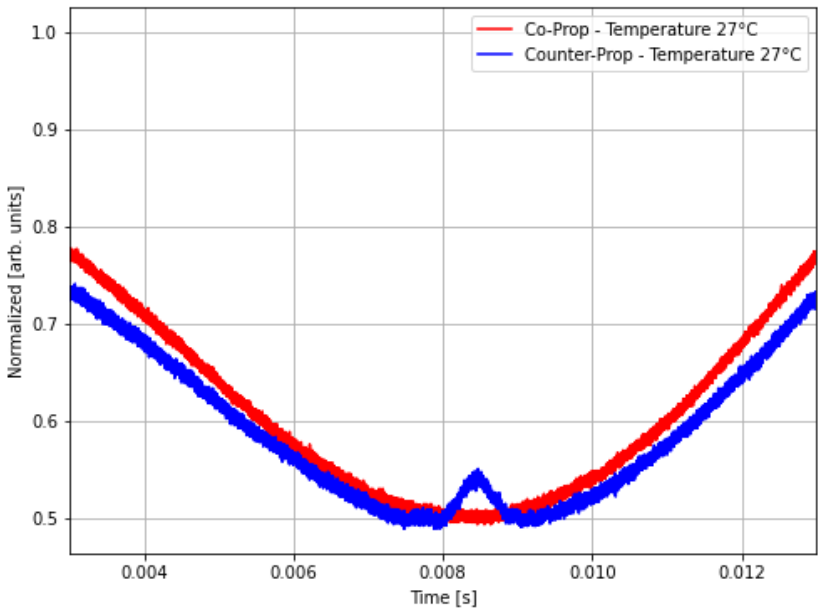

Figure 4.8: *First realization of the non-reciprocal EIT scheme. The blue curve is the counter-propagating absorption and small transmission window. The red curve shows no transmission window opening up.*

The detection was performed using photodiodes[3] connected to an oscilloscope. The parameters and experimental procedure were far from optimal. The scan range, for instance, was chosen to cover only a single resonance, leaving us without a true frequency reference. Therefore, the absorption shown in figure 4.8 is shown as a function of time. Also, the overall absorption was just around 50%. This is due to a combination of too few atoms and too many photons. The height of the EIT peak relative to the absorption shows only a 5% increase in transmission. This is much lower than expected at our control Rabi frequency. The peak is also relatively wide at the base indicating a high dephasing rate. The low EIT peak is caused by multiple effects, including sub-optimal polarizations and non-perfect alignment.

To improve the signal, the changes discussed in the following were done.

[3] PDA10A2 from Thorlabs

Optimizing the setup

First and foremost the Rydberg state was changed from $30S_{1/2}$ to $20S_{1/2}$. As shown in figure 4.3 this results in twice the Rabi frequency and we figured tuning the laser to this frequency was possible without losing output power.

Secondly, the probe intensity was reduced to the weak probe regime. This meant exchanging the photodiodes for SPCMs connected to a Time Tagger. The probe intensity was adjusted such that count rates of roughly 8×10^5 counts/s were measured in both arms. This corresponds to powers on the order of 30 fW and puts us in a regime of a weak probe but high enough count rates to detect for a sufficiently short time to neglect the inevitable long-term frequency drift of an unlocked laser.

The final large change to the setup was to use a DLPro laser from the running Rydberg quantum optics experiment as opposed to the DFB laser used for the first realization of the effect. As discussed in chapter 2 the DFB laser is known to have a much larger linewidth when free-running than cavity diode lasers such as the Toptica DLPro. Using a more sophisticated laser also allowed for better monitoring of the scan to ensure a linear scan in frequency over the range of interest. Changing the laser turned out to have a remarkable influence on the resulting EIT spectrum. So far only the single peak as shown in figure 4.8 was seen. However, this changed dramatically with the reduced linewidth giving rise to EIT resonances from each of the hyperfine states of the excited state.

Final Experimental Results

The data collected with the $20S_{1/2}$ Rydberg state, SPCMs, and DLPro laser is shown in figure 4.9 and 4.10. Three sets of data were taken each with different polarization. Figure 4.9 shows a data set where the polarization was optimized on highest possible EIT. Figure 4.10 shows the same for circularly and linearly polarized light respectively. A PBS was used to adjust the waveplates to have a know polarization.
In the following data the probe laser is scanned across the $^{87}Rb,\ F = 2$ and $^{85}Rb,\ F = 3$ absorption valleys.

The data with the unknown polarization is shown in figure 4.9. In this figure, the signal is plotted with the control laser turned on (blue graph) and with the control laser turned off (red graph). This shows very good overlap and hence no power broadening due to the blue laser is observed.

If this spectrum was corrected for ^{87}Rb or ^{85}Rb respectively there would be several peaks reaching unit transmission. Such a correction would include fitting the sum of equation (4.5) for each isotope. Even though the transmission is still 40% at the lowest point and the transmission window is not from full absorption to full transmission it is still a very clear improvement from the initial realization in figure 4.8. By increasing the temperature, hence the number of atoms, the absorption would go down but this would also reduce the height of the transmission peak. Because this relation was already shown in reference [23] it was not examined further in this work.

In figure 4.10 the data taken with circularly and linearly polarized light respectively, are shown.

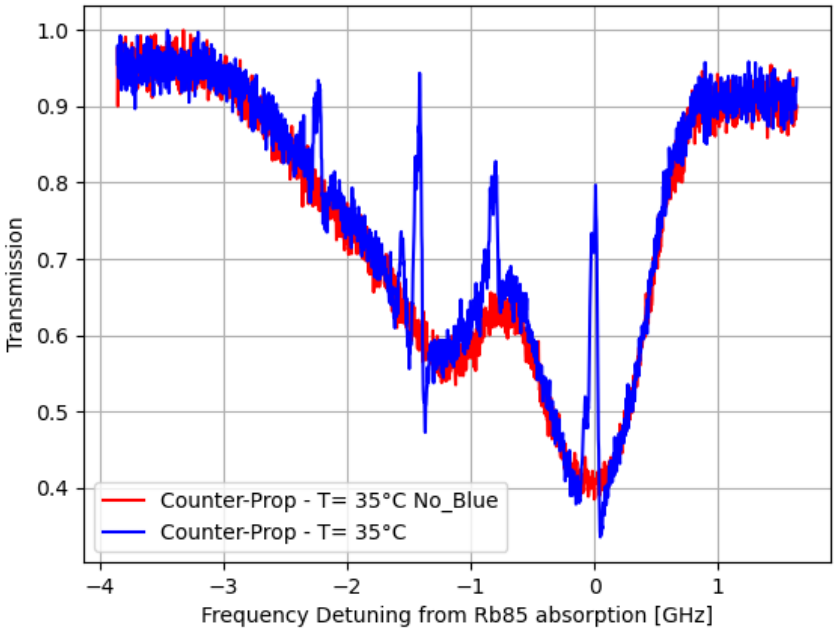

Figure 4.9: *Non-reciprocal scheme with unknown polarization optimized solely on the height of the rightmost EIT peak. The blue is the signal with a control field and the red is without a control field. No power broadening is observed. Almost unit transmission is achieved for several transmission peaks if corrected for absorption due to the other isotope.*

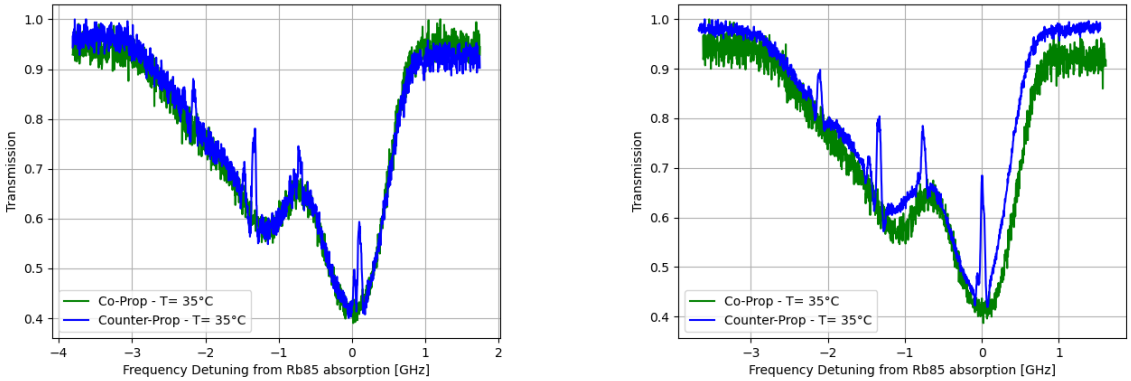

(a) *Circularly polarization* **(b)** *Linearly polarization*

Figure 4.10: *The blue is the counter-propagating light and the green is the co-propagating. Different heights of the transmission peaks are observed for the different polarization.*

It is clear from the figure that the coupling strength from the excited state to the Rydberg state is lower for the circular polarized light than for the linear polarized. This is seen from the height of the transmission peaks. What is interesting is that the unknown polarization seems to couple stronger to the Rydberg state than the two known polarizations. This may indicate that the linear polarization, which was adjusted to be perpendicular to the table, does not match the quantization axis, due to the magnetic field, as well as the unknown polarized light did.

It is worth noticing that on each of the above three graphs there is a frequency axis that represents the detuning from the $^{85}RbF = 3$ valley. This is derived from atomic data. The center of the ^{87}Rb and ^{85}Rb valleys are identified and the observed time difference between them is converted to frequency using atomic data [29,30]. This approach requires the laser scan to be linear and have only minimal hysteresis, as discussed in section 2.4. To ensure this, the laser was optimized to scan linearly over a range larger than the frequency range of the spectrum. This was done by adjusting the scan parameters on the scan module of the DLPro laser. Using this approach there is also uncertainty related to the fact that what is seen as two absorption valleys has a substructure as examined when doing Doppler-free spectroscopy in section 4.3. The fact that not all of the substructure contribute evenly, as each transition has a different Clebsch-Cordon coefficient, it has the potential of displacing the minima of the absorption valley by some frequency. To compensate for this effect each substate has to be taken into account. This is a rather complicated calculation even though all the atomic data is available and was not performed due to lack of time.

As a sanity check, a beat note between the probe laser and a different 780 nm laser locked to a high finesse cavity, the 'Master Laser', was created. In figure 4.11 the beat note frequency of the probe laser relative to the Master Laser is seen as a function of time during a scan of the probe laser.

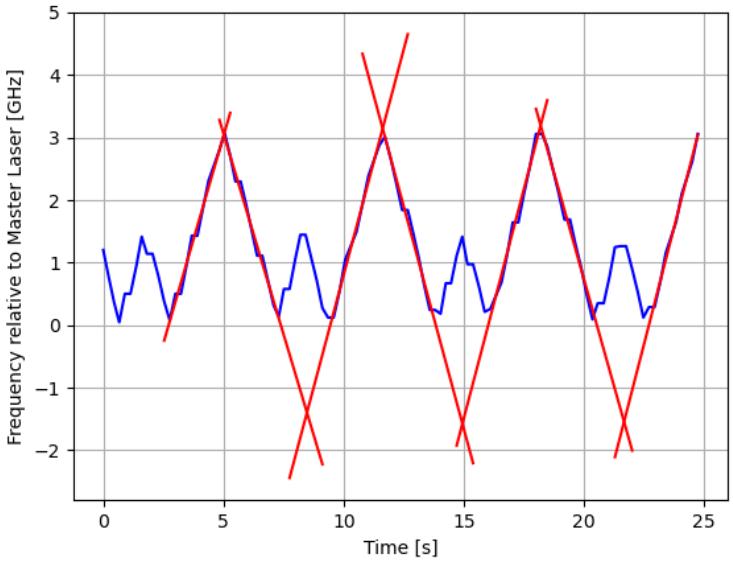

Figure 4.11: *Scan relative to the master laser. The blue is the data from the spectrum analyzer. The small "triangular peaks" are when the scan frequency is less than the frequency of the master laser but the beat note frequency never goes negative. The red lines are linear fits.*

The small triangular peaks are when $\omega_p < \omega_{master}$, but as the beat note frequency cannot be negative, see section 1.1, it appears to scan like this, rather than nice triangles. The red lines are linear fits to the scan. The sampling frequency is too low to meaningfully say anything about the hysteresis behavior of the scan. From this data, it is linear in frequency and the two-point translation to frequency is assumed reasonable. Another important feature in this plot is that no visible drift of the scan happens on a 15 s timescale on which the experiment is performed. This proves that it is acceptable to overlap frequency scans taken at 15 Hz over 15 s without any corrections for drift.

In figures 4.9 and 4.10 one finds at least four EIT peaks which appear in the same location independent of polarization. It is logical to try to identify the transitions responsible for these peaks.
When one considers the possible excitations from $|1\rangle \rightarrow |3\rangle$, which are determined by selection rules, it turns out that a total of six possible excitation routes can occur. These are shown in figure 4.12.

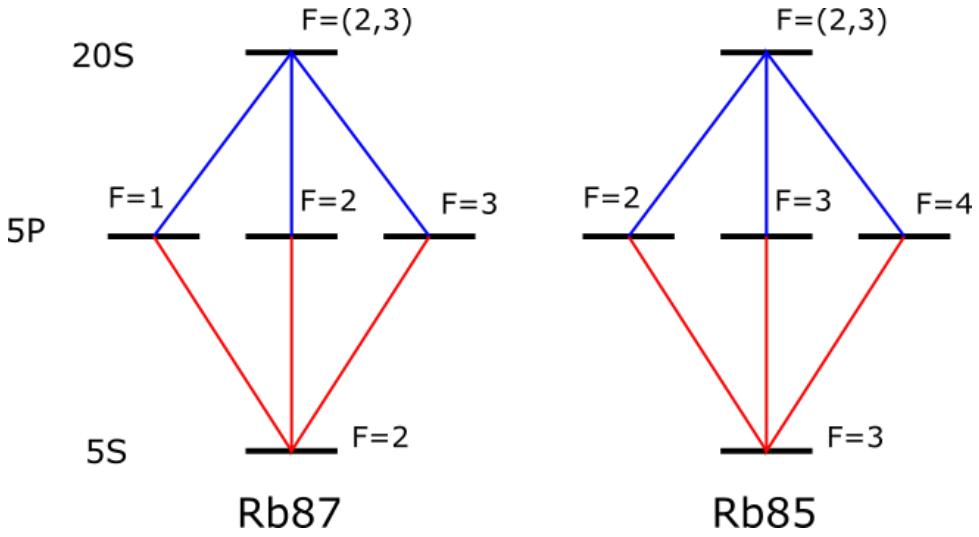

Figure 4.12: *All possible excitation routes from the ground state to the Rydberg state for the two absorption valleys. A total of six peaks should be visible according to theory. Each of the six has slightly different probe resonances due to the hyperfine splitting.*

The hyperfine splitting of the $20S_{1/2}$ state is 7 MHz and is thus neglected [59]. Each of the six routes appears at different probe frequencies due to the hyperfine levels shown in section 1.4.

To calculate the position of each peak in the spectrum the detuning from two photon resonance is of interest. The two photon resonance is $\omega_{p0} + \omega_{c0}$ with each term given as the frequency plus some contribution from the velocity

$$\begin{aligned} \omega_{c0} &= \omega_c - k_c v \\ \omega_{p0} &= \omega_p + k_p v. \end{aligned} \tag{4.8}$$

By combining these equations the probe frequency, i.e. the position in the rubidium spectrum, can be calculated via the relation

$$\omega_p = \omega_{p0} + \frac{k_p}{k_c}\left(\omega_{c0} - \omega_c\right). \tag{4.9}$$

Here $(\omega_{c0} - \omega_c)$ is the control detuning which is the unknown factor in this equation that will have to be fitted to the data. k_p and k_c are the respective wavevectors and ω_{p0} is the single photon resonance for the $|1\rangle \rightarrow |2\rangle$ transition. This is always resonant as the probe laser is scanned. Work on this is still being done and is thus not presented here.

Improvements and Further Work

This project was stopped as the whole laboratory was moving from Odense to Bonn. While the effect has been shown with great success there are still a few minor things that can be improved.

It will be possible to obtain a higher control power than used for the final data shown in this thesis. The light emitted from the TA-SHG laser was incident on a HWP followed by a PBS[4] with the reflected arm going to the experiment. However, the cube was degrading over time and thus the power to the experiment dropped from 1 W at the start to roughly 650 mW when the experiment was packed up. Exchanging the cube for a different optics component could yield more power in the control beam.

The process of filtering the blue from the red can also be improved by using an additional set of laser-line filters followed by a single-mode fiber. In the current setup, the count rate of the background is 0.02% of the total counts but this can be reduced further if required. Reducing it would allow for fewer photons in the probe without drowning in background noise.

The next logical step would be to lock the lasers. By locking the control laser to a stable laser cavity the linewidth could be greatly reduced, leading to lower dephasing rates. While locking the control laser is relatively straightforward as it just has to be locked to a single frequency, locking the probe will pose a far more difficult challenge. This involves building electronics allowing for a scan over a handful of GHz while keeping the laser in lock to have the benefit of the narrow linewidth.

While this experimental work was in progress, similar work was published by Ming-Xin Dong, Ke-Yu Xia, Wei-Hang Zhang, Yi-Chen Yu, Ying-Hao Ye, En-Ze Li, Lei Zeng, Dong-Sheng Ding, Bao-Sen Shi, Guang-Can Guo, and Franco Nori. The publication investigates exactly the theory proposed by Zhang and Pohl, and the expected difference between co- and counter-propagating EIT is beautifully demonstrated. The main difference between the work by Ming-Xin et. al. and the work discussed in this thesis is the choice of the excited state. Ming-Xin et. al. excites the atoms of an isotope pure cell via the D2 line and further to the $5D_{5/2},\ F = 4$ state while this work observes the same effect using a Rydberg state as the highest lying state.
By utilizing the 776 nm transition to the $5D_{5/2},\ F = 4$, it is possible for Ming-Xin et. al. to achieve enormous Ω_c on the order of 320 Mhz since the dipole matrix element of this transition is much larger as opposed to that of the $20S_{1/2}$ Rydberg state.
To the best of our knowledge, this work is, however, the first demonstration of this effect with a Rydberg state as the highest lying state.

[4] PBS121 from Thorlabs

Chapter 5

Conclusion and Outlook

This thesis deal with three different topics, namely the design and construction of a setup for lock three lasers with different wavelengths to an ultra stable cavity, the design and construction of a phase interferometer for measuring the phase change imprinted on a photon through interaction with an atom, and an experiment to investigate electromagnetically induced transparency in a hot atomic vapor.
The two first topics are directly aimed at application in an existing experimental setup for investigating nonlinear quantum optics with Rydberg states of ultracold rubidium. The last topic is not a direct extension of this experiment but rather explores a new approach to the realization of non-reciprocal optics.

To lock the three different lasers, the lasers were coupled into an ultra-low expansion optical resonator, which can be used to generate a PDH error signal, to which the lasers can be locked. The three lasers were a 780 nm used to probe rubidium atoms to an excited state, a 960 nm TA-SHG laser used as the control laser for performing Rydberg excitations, and a 1012 nm laser to be used for a magic wavelength trap. A laser lock was achieved for the control laser but the cavity was not under vacuum and drifts of the entire cavity systems on the order of a few MHz were discovered. The drift was determined by looking at the beat note signal with respect to a similar laser locked to a different cavity that was under vacuum.
Further work on the cavity setup would include a thorough examination of the leakage, preventing vacuum. Following this, the two remaining lasers should be locked and the finesse of the cavity determined for these two wavelengths. This is expected to happen in the immediate future, as the setup designed in the scope of this thesis is currently being rebuild for the next iteration of the nonlinear quantum optics experiment.

The phase interferometer demonstrated in this thesis, utilizing the relative phase shift of a beat note signal to measure the phase of photons interacting with Rydberg atoms, was designed and built. The interferometer was first constructed and tested on the side in an experiment-compatible format in which a drift correlated to temperature fluctuations in the lab of 1° was determined. Further, the electronics required to trigger the data collection on a classical reference signal were tested. This testing was done using an EOM to induce a phase shift in one of the beat note paths. The measurements show the same observed phase shift when measuring in the classical and quantum regimes. This shows that the setup is capable of detecting single-photon phase shifts.
Finally, the setup was implemented in the running Rydberg quantum optics experiment and the triggering procedure implemented in the experiment control. Measurements were performed at 20 MHz, 40 MHz, 70 MHz, and 100 MHz probe detuning, but two-photon

EIT resonance, in a long cloud of ultracold rubidium atoms. The data show that the phase change increases when approaching EIT resonance and changes sign when crossing resonance. The magnitude of the phase change increases with decreasing probe photon rate. It also increases with lower probe detuning.
The interferometer discussed in this thesis was implemented in the nonlinear quantum optics experiment in Odense and will be rebuilt in the new iteration in Bonn. Once rebuilt, further work using this setup would include measurements at more probe detunings with a fixed photon rate, to make a plot of phase change vs. probe detuning. It would also include going to a very small cloud supporting only one Rydberg excitation due to the Rydberg blockade. This is called the superatom regime and would allow us to study the fundamental phase behavior the interaction with a single excitation.

The final topic of this thesis is on a novel scheme for realizing an all-optical non-reciprocal effect using the velocity of the atoms in an atomic vapor was also realized in this work. By utilizing the avoided crossing in a ladder EIT scheme induced by the negative Doppler effect for a two-photon transition with $k_c > k_p$ and a very large probe rabi frequency Ω_c, it is shown that a broadened EIT window is opened when probe and control are counter-propagating while no EIT window is seen for co-propagating beams. The probe laser was scanned across the ^{87}Rb, $F = 2$ and ^{85}Rb, $F = 3$ $5S_{1/2} \rightarrow 5P_{3/2}$ transition. Applying a strong control field exciting from $5P_{3/2} \rightarrow 20S_{1/2}$ a spectrum exhibiting EIT behavior for each hyperfine level of the intermediate state was found. The EIT peaks go almost to unity transmission for polarization optimized on the EIT signal. While this thesis shows the first demonstration of this velocity-dependent non-reciprocal effect with Rydberg atoms some optimization can be considered for future iterations of the experiment. These would include implementing a better magnetic field control and frequency stabilizing the lasers.
For the work presented in this thesis control laser was free running and the frequency was chosen based on having a strong EIT signal hence the control detuning is completely unknown.
Within the time frame of this thesis, it was not possible to identify the individual transitions in the recorded spectrum. This remains a work in progress, along with further considerations of how this effect can be utilized in future technical applications.

Bibliography

[1] Peter A. Franken. Lasers. generation of light by stimulated emission. *Science*, 140(3567):647–648, 1963.

[2] R. W. P. Drever, J. L. Hall, F. V. Kowalski, J. Hough, G. M. Ford, A. J. Munley, and H. Ward. Laser phase and frequency stabilization using an optical resonator. *Applied Physics B*, 31, June 1983.

[3] T. Kessler, C. Hagemann, C. Grebing, T. Legero, U. Sterr, F. Riehle, M. J. Martin, L. Chen, and J. Ye. A sub-40-mhz-linewidth laser based on a silicon single-crystal optical cavity. *Nature Photonics*, 6(10):687–692, 10 2012. Copyright - Copyright Nature Publishing Group Oct 2012; Last updated - 2012-10-17.

[4] J. Alnis, A. Matveev, N. Kolachevsky, Th. Udem, and T. W. Hänsch. Subhertz linewidth diode lasers by stabilization to vibrationally and thermally compensated ultralow-expansion glass fabry-pérot cavities. *Phys. Rev. A*, 77:053809, May 2008.

[5] M. Schioppo, R. C. Brown, W. F. Mcgrew, N. Hinkley, R. J. Fasano, K. Beloy, T. H. Yoon, G. Milani, D. Nicolodi, J. A. Sherman, N. B. Phillips, C. W. Oates, and A. D. Ludlow. Ultrastable optical clock with two cold-atom ensembles. *Nature Photonics*, 11(1):48–52, 01 2017. Copyright - Copyright Nature Publishing Group Jan 2017; Last updated - 2017-01-03.

[6] Colin J. Kennedy, Eric Oelker, John M. Robinson, Tobias Bothwell, Dhruv Kedar, William R. Milner, G. Edward Marti, Andrei Derevianko, and Jun Ye. Precision metrology meets cosmology: Improved constraints on ultralight dark matter from atom-cavity frequency comparisons. *Phys. Rev. Lett.*, 125:201302, Nov 2020.

[7] O Firstenberg, C S Adams, and S Hofferberth. Nonlinear quantum optics mediated by rydberg interactions. *Journal of Physics B: Atomic, Molecular and Optical Physics*, 49(15):152003, jun 2016.

[8] Thomas F. Gallagher. *Rydberg Atoms*. Cambridge Monographs on Atomic, Molecular and Chemical Physics. Cambridge University Press, 1994.

[9] M. Saffman, T. G. Walker, and K. Mølmer. Quantum information with rydberg atoms. *Rev. Mod. Phys.*, 82:2313–2363, Aug 2010.

[10] Sebastian Weber, Christoph Tresp, Henri Menke, Alban Urvoy, Ofer Firstenberg, Hans Peter Büchler, and Sebastian Hofferberth. Calculation of rydberg interaction potentials. *Journal of Physics B: Atomic, Molecular and Optical Physics*, 50(13):133001, jun 2017.

[11] M. D. Lukin, M. Fleischhauer, R. Cote, L. M. Duan, D. Jaksch, J. I. Cirac, and P. Zoller. Dipole blockade and quantum information processing in mesoscopic atomic ensembles. *Phys. Rev. Lett.*, 87:037901, Jun 2001.

[12] E. Urban, T. A. Johnson, T. Henage, L. Isenhower, D. D. Yavuz, T. G. Walker, and M. Saffman. Observation of rydberg blockade between two atoms. *Nature Physics*, 5:110–114, 2009.

[13] Y. O. Dudin and A. Kuzmich. Strongly interacting rydberg excitations of a cold atomic gas. *Science*, 336(6083):887–889, 2012.

[14] Asaf Paris-Mandoki, Christoph Braun, Jan Kumlin, Christoph Tresp, Ivan Mirgorodskiy, Florian Christaller, Hans Peter Büchler, and Sebastian Hofferberth. Free-space quantum electrodynamics with a single rydberg superatom. *Phys. Rev. X*, 7:041010, Oct 2017.

[15] Michael Fleischhauer, Atac Imamoglu, and Jonathan P. Marangos. Electromagnetically induced transparency: Optics in coherent media. *Rev. Mod. Phys.*, 77:633–673, Jul 2005.

[16] Han Seb Moon, Kyoungdae Kim, and Jung Kim. Laser frequency stabilizations using electromagnetically induced transparency. *Applied Physics Letters*, 84, 04 2004.

[17] Ofer Firstenberg, Thibault Peyronel, Qi-Yu Liang, Alexey V. Gorshkov, Mikhail D. Lukin, and Vladan Vuletić. Attractive photons in a quantum nonlinear medium. *Nature*, 502:71–75, Oct 2013.

[18] Daniel Tiarks, Steffen Schmidt, Gerhard Rempe, and Stephan Dürr. Optical pi phase shift created with a single-photon pulse. *Science Advances*, 2(4):e1600036, Apr 2016.

[19] Tauhid R. Zaman, Xiaoyun Guo, and Rajeev J. Ram. Semiconductor waveguide isolators. *Journal of Lightwave Technology*, 26(2):291–301, 2008.

[20] Li Fan, Jian Wang, Leo T. Varghese, Hao Shen, Ben Niu, Yi Xuan, Andrew M. Weiner, and Minghao Qi. An all-silicon passive optical diode. *Science*, 335(6067):447–450, 2012.

[21] Nicholas A. Estep, Dimitrios L. Sounas, Jason Soric, and Andrea Alù. Magnetic-free non-reciprocity and isolation based on parametrically modulated coupled-resonator loops. *Nature Physics*, 10:923–927, 2014.

[22] et. al. Zhan, Ming-sheng. Doppler-free spectroscopy of rubidium atoms driven by a control laser. *Frontiers of Physics*, 7, June 2012.

[23] Ming-Xin Dong, Ke-Yu Xia, Wei-Hang Zhang, Yi-Chen Yu, Ying-Hao Ye, En-Ze Li, Lei Zeng, Dong-Sheng Ding, Bao-Sen Shi, Guang-Can Guo, and Franco Nori. All-optical reversible single-photon isolation at room temperature. *Science Advances*, 7(12), 2021.

[24] F. Träger. *Springer Handbook of Lasers and Optics*. Springer Handbooks. Springer Berlin Heidelberg, 2012.

[25] Rodney Loudon. *The Quantum Theory of Light*. Oxford Science Publications, 2010.

[26] S. J. M. Kuppens, K. L. Corwin, K. W. Miller, T. E. Chupp, and C. E. Wieman. Loading an optical dipole trap. *Phys. Rev. A*, 62:013406, Jun 2000.

[27] Markus Aspelmeyer, Tobias J. Kippenberg, and Florian Marquardt. Cavity optomechanics. *Rev. Mod. Phys.*, 86:1391–1452, Dec 2014.

[28] M.D. Lukin. Modern atomic and optical physics ii. `https://lukin.physics.harvard.edu/teaching`, 2016. [Online; accessed 30-March-2020].

[29] Daniel A. Steck. Rubidium 85 d line data. `http://steck.us/alkalidata`, 2008. [revision 2.2.2 29 April 2021. Online; accessed 11-May-2021].

[30] Daniel A. Steck. Rubidium 87 d line data. `http://steck.us/alkalidata`, 2001. [revision 2.2.1 21 November 2019. Online; accessed 11-May-2021].

[31] D.A. Steck. *Quantum and Atom Optics*. 2007.

[32] Christoph Tresp. A Setup for Highly Precise Excitation and Detection of Rydberg Atoms, 26. October 2012.

[33] I. I. Beterov, I. I. Ryabtsev, D. B. Tretyakov, and V. M. Entin. Quasiclassical calculations of blackbody-radiation-induced depopulation rates and effective lifetimes of rydberg ns, np, and nd alkali-metal atoms with $n \leq 80$. *Phys. Rev. A*, 79:052504, May 2009.

[34] I. I. Ryabtsev, I. I. Beterov, D. B. Tretyakov, V. M. Entin, and E. A. Yakshina. Doppler- and recoil-free laser excitation of rydberg states via three-photon transitions. *Phys. Rev. A*, 84:053409, Nov 2011.

[35] M. D. Lukin, M. Fleischhauer, R. Cote, L. M. Duan, D. Jaksch, J. I. Cirac, and P. Zoller. Dipole blockade and quantum information processing in mesoscopic atomic ensembles. *Phys. Rev. Lett.*, 87:037901, Jun 2001.

[36] Nina Stiesdal, Hannes Busche, Kevin Kleinbeck, Jan Kumlin, Mikkel G. Hansen, Hans Peter Büchler, and Sebastian Hofferberth. Controlled multi-photon subtraction with cascaded rydberg superatoms as single-photon absorbers, 2021.

[37] C P Pearman, C S Adams, S G Cox, P F Griffin, D A Smith, and I G Hughes. Polarization spectroscopy of a closed atomic transition: applications to laser frequency locking. *Journal of Physics B: Atomic, Molecular and Optical Physics*, 35(24):5141–5151, dec 2002.

[38] H. Kogelnik and C. V. Shank. Coupled-wave theory of distributed feedback lasers. *Journal of applied physics*, 43(5):2327–2335, 1972.

[39] M. S. Safronova, Carl J. Williams, and Charles W. Clark. Optimizing the fast rydberg quantum gate. *Phys. Rev. A*, 67:040303, Apr 2003.

[40] H. Nguyen, J. Lampen, P. R. Berman, and A. Kuzmich. Differential nuclear-spin-dependent light shifts and state mixing of rydberg atoms. *Phys. Rev. A*, 100:033412, Sep 2019.

[41] J. Lampen, H. Nguyen, L. Li, P. R. Berman, and A. Kuzmich. Long-lived coherence between ground and rydberg levels in a magic-wavelength lattice. *Phys. Rev. A*, 98:033411, Sep 2018.

[42] M. Teich and B. Saleh. *Fundamentals of Photonics*. Wiley Interscience Publication, 1991.

[43] Philipp Lunt. Design and Construction of a New Ultracold Ytterbium Experiment For Rydberg Physics, 1. January 2019.

[44] Eric D. Black. An introduction to pound-drever-hall laser frequency stabilization. *American Journal of Physics*, 69(1), 2000.

[45] RP Photonics Encyclopedia. Gouy phase shift. `https://www.rp-photonics.com/gouy_phase_shift.html`, 2020. [Online; accessed 04-May-2020].

[46] Wei Shibiao, Stuart K. Earl, Lin Jiao, Shan S. Kou, and Yuan Xiao-Cong. Active sorting of orbital angular momentum states of light with a cascaded tunable resonator. *Light: Science and Applications*, 9(1), 2020. Copyright - This work is published under http://creativecommons.org/licenses/by/4.0/ (the "License"). Notwithstanding the ProQuest Terms and Conditions, you may use this content in accordance with the terms of the License; Last updated - 2020-04-14.

[47] Yu V Troitskiĭ. Optimization and comparison of the characteristics of optical interference discriminators. *Soviet Journal of Quantum Electronics*, 8(5):628–631, may 1978.

[48] Frank L. Pedrotti, Leno M. Pedrotti, and Leno S. Pedrotti. *Introduction to Optics*. Cambridge University Press, 2018.

[49] SciPy.org. Scipy signal find peaks documentation. `https://docs.scipy.org/doc/scipy/reference/generated/scipy.signal.find_peaks.html`. [Online; accessed 19-Jan-2021].

[50] Qi-Yu Liang, Aditya V. Venkatramani, Sergio H. Cantu, Travis L. Nicholson, Michael J. Gullans, Alexey V. Gorshkov, Jeff D. Thompson, Cheng Chin, Mikhail D. Lukin, and Vladan Vuletić. Observation of three-photon bound states in a quantum nonlinear medium. *Science*, 359(6377):783–786, Feb 2018.

[51] Keysight Infiniivision. *3000 series prog guide*, Nov 2020.

[52] R. S. Weis and T. K. Gaylord. Lithium niobate: Summary of physical properties and crystal structure. *Applied Physics A*, 37:191–203, Aug 1985.

[53] Marian Rockenhauser. A Setup For Heterodyne Single Photon Phase Shift Detection, 26. August 2016.

[54] James H. McClellan, Ronald W. Schafer, and Mark A. Yoder. *DSP First*. Pearson, 2015.

[55] David J. C. MacKay. *Information Theory, Inference and Learning Algorithms*. Cambridge University Press, 2003.

[56] SciPy.org. Scipy optimize curve fit documentation. `https://docs.scipy.org/doc/scipy/reference/generated/scipy.optimize.curve_fit.html`. [Online; accessed 18-Jan-2021].

[57] Shicheng Zhang, Gongwei Lin, Yiqi Hu, Yihong Qi, Yueping Niu, and Shangqing Gong. Cavity-free circulator with low insertion loss using hot atoms. *Phys. Rev. Applied*, 14:024032, Aug 2020.

[58] Lida Zhang and Thomas Pohl. High-fidelity single-photon isolator in hot atoms, 2020.

[59] Atreju Tauschinsky, Richard Newell, H. B. van Linden van den Heuvell, and R. J. C. Spreeuw. Measurement of87rb rydberg-state hyperfine splitting in a room-temperature vapor cell. *Physical Review A*, 87(4), Apr 2013.

Acknowledgements

A lot of people have contributed to this work and I am thankful for the support. I'd like to mention a few people,

- I'd like to thank my supervisor Sebastian Hofferberth for giving me the opportunity of doing this project during these difficult times of lock down and the move to Bonn. I've had a great time and learned a lot of interesting physics and your continuous attempt to get me access to the lab has been greatly appreciated. I would also like to thank you for giving me the opportunity to perform a brand new experiment when the chance arose.

- I would also like to thank Thomas Pohl and Lida Zhang from the University of Aarhus. It has been a pleasure working together with you on your theory proposal. I can safely say that I have never learned so much new and interesting physics in such a short time before and I greatly appreciate the opportunity.

- I would like to thank the institute of Physics, Chemistry and Pharmacy at SDU for their effort in keeping the university running in these difficult times. Special mentions from the institute are Danny from the electronics workshop, who's been assisting with the home built electronics, Sanne for not stealing all the labsnacks from Thorlabs, and Lars for assisting with crucial drilling tasks beyond my capabilities!

- A thanks also goes out to my fellow physics students at SDU. The discussions we have had in Æter has been a huge part of my time studying here. And remember, goals from the midfield always count!

- A special thanks also go to my lab-partners Hannes Busche and Nina Stiesdal and the rest of the NQO team.

- Hannes, your knowledge and passion for physics has been an inspiration throughout my year in the lab. You were always there, ready to discuss Physics, Corona-rules, the American election or something else! I can safely say that without your post-doc magic this project would not have been what it has become.

- Nina Stiesdal, rarely have I been so lucky as to meet someone with your good mood! Your everyday assistance throughout this project and especially your help during the writing up of this thesis has been very much appreciated.

- A huge thank you also goes to my entire family for their support and willingness to hear about my work, thought I know the 10th story about "photons" can make a long evening!

- Finally, the biggest thank you of them all goes to my beloved girlfriend Charlotte. Your support throughout our years together has been a huge part of my success with this work!